Pontificia Universidad Católica del Perú

Escuela de Posgrado

Tesis de Maestría

Real-Time Quantitative Sonoelastography in an Ultrasound Research System

Para obtener el grado de:

Master of Science (M. Sc.)

en Ingeniería Mecatrónica

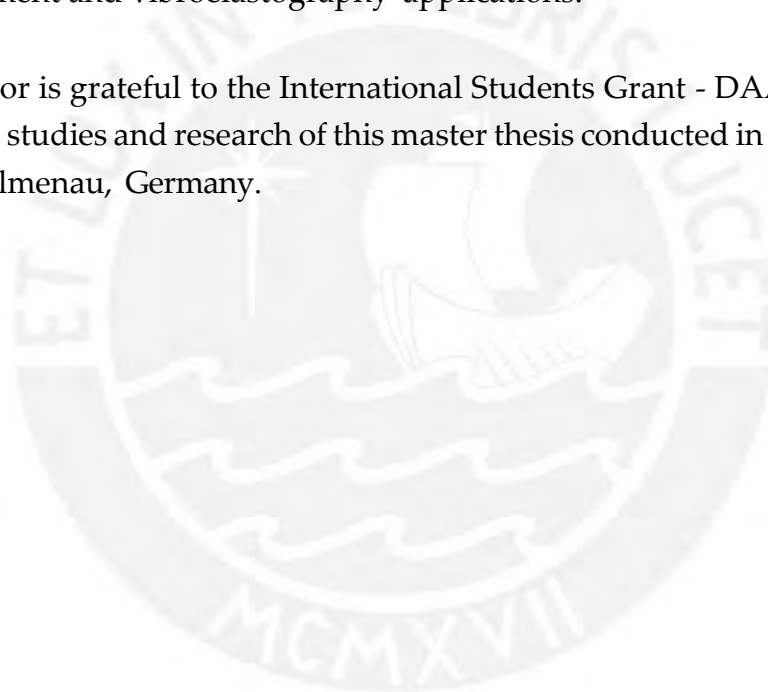|	
Presentado por:	Eduardo André González Bellido
Fecha y lugar de nacimiento:	07. 10. 1989, Lima, Perú
Tutor Responsable (TU Ilmenau):	Prof. Dr.-Ing. habil. Pu Li
Profesor Responsable (TU Ilmenau):	Prof. Dr.-Ing. habil. Pu Li
Profesor Responsable (PUCP):	Prof. Dr. -Ing. Benjamín Castañeda Aphán
Fecha y Lugar:	24. 07. 2017, Lima

Acknowledgements

Kurzfassung

Quantitative Sono-Elastographie ist eine neue Technologie für die Ultraschall Bildgebung, die Radiologen maligne Tumoren ohne Risiko der strahlungsinduzierten Krebs (d.h. Mammographie) zu erfassen können. Aufgrund gefunden Rechenkomplexität in der aktuellen Algorithmen, Implementierung von Echtzeit-Anwendungen, die Prüfungsverfahren profitieren wurde jedoch noch nicht berichtet. Zusätzlich, aktuelle Schätzer für die Darstellung eine Elastizität Bilder vorhanden Artefakte der hohen Schätzung Varianz, die die Techniker in die Gegenwart steifer Massen irreführen könnten und zwar, falsch-positive Diagnose zu erzeugen.

In dieser Arbeit wird eine GPU-basierte Elastographie-System entwickelt und an einem Forschungsultraschallgeräten implementiert. Quantitative Elastizität in Echtzeit bei 2 FPS mit einer Verbesserung Rechenzeitfaktor aus 26 wird gezeigt. Validierung der Systemgenauigkeit Anzeige wurde, auf Gelatinebasis Gewebe Phantome durchgeführt., waren niedrige Vorspannung der Elastizitätswerte berichtet wurde (4,7 %) bei geringe Anregungsfrequenzen nachahmt. Ausserdem wird eine neue Elastizität Schätzer auf quantitative Sono-Elastographie basiert eingeführt. Ein lineares Problem wurde entlang der seitlichen Abmessung modelliert und eine Regularisierung Methode wurde implementieren. Elastizität Bilder mit niedriger Vorspannung wurde darstellen (1,48 %) sowie seine Leistung in einer Brust kalibrierte Phantom mit verbesserter CNR (47,3 dB) im Vergleich mit anderen Schätzer ausgewertet sowie die Verringerung Seiten Artefakte bereits erwähnt in der Literatur (PD: 22,7 dB, 1DH 28,7 dB) gefunden. Diese zwei Beitrag profitieren, die Umsetzung und Entwicklung weiterer Elastographie Techniken, die eine verbesserte Qualität der Elastizität Bilder liefern könnten und somit eine verbesserte Genauigkeit der Diagnose.

Abstract

Quantitative sonoelastography is an alternative technology for ultrasound imaging that helps radiologist to diagnose malignant tumors with no risk of radiation-induced cancer (i.e. mammography). However, due to the high computational complexity found in the current algorithms, implementation of real-time systems that could benefit examination procedures has not been yet reported. Additionally, elasticity maps depicted from current estimators feature artifacts of high estimation variance that could mislead the technician into the presence of stiffer masses, generating false positive diagnosis.

In this thesis, a GPU-based elastography system was designed and implemented on a research ultrasound equipment, displaying quantitative elasticity in real-time at 2 FPS with an improvement computational time factor of 26. Validation of the system accuracy was conducted on gelatin-based tissue mimicking phantoms, where low bias of elasticity values were reported (4.7%) at low excitation frequencies. Additionally, a new elasticity estimator based on quantitative sonoelastography was developed. A linear problem was modeled from the acquired sonolastography data along the lateral dimension and a regularization method was implemented. The resulting elasticity images presented low bias (1.48%), enhanced CNR and reduced lateral artifacts when evaluating the algorithm's performance in a breast calibrated phantom and comparing it with other estimators found in the literature. These two contribution benefit the implementation and development of further elastography techniques that could provide enhanced quality of elasticity images and thus, improved accuracy of diagnosis.

Contents

1 Introduction

1.1 Motivation

In this chapter, a brief description of the current situation of breast cancer in Peru is exposed. Likewise, the technological evolution of the methods and state of art equipment used to detect and diagnose tumors worldwide are presented.

1.1.1 Cancer in Perú

Breast cancer is one of the most common malignancies in Peru. In recent decades, the incidence has increased considerably, reaching similar frequency than prostate cancer cases as well as surpassing stomach and lung cases. In 2014, the Ministry of Health conducted a study of cancer registration during 2004-2005 in the capital, Lima, where 33.8% of tumors in 16,319 women with cancer were located in the breast. Furthermore, the mortality rate found for breast cancer was 10.7 per 100,000 females, higher than the cervical cancer (7.9 per 100,000 females) as well as stomach cancer (10.1 per 100,000 females) [dEN14]. Globally, the incidence and mortality rate for 2010 was 39% and 12.5% respectively, while in Latin America was 39.7% and 12.4% [FSB+08].

In Peru, the late diagnosis of this disease is the leading cause of death in breast cancer patients. According to the Instituto Nacional de Enfermedades Neoplásicas, 90% of patients are hospitalized with a tumor above stage I, reaching a considerable size and demonstrating the need for early detection to treat it on time [Pro98]. Among the most used diagnostic tools, mammography is an imaging technique where the mammary structure is exposed to X-ray dose, obtaining a craniocaudal and mediolateral oblique image of it which aids the radiologist to localize abnormalities or tumors therein [Gue11]. This procedure has been widely used worldwide, presenting an 96% accuracy of detecting cancerous lesions. Hence, mammography examinations are usually included in the regular checkups for women of middle and advanced age [GH12].

Factors contributing to the cumulative risk of developing breast cancer (3.69% up to 74 years) typically involve obesity, late menopause, family history and early menarche

[dEN14]. However, radiation-induced mammography, despite being regulated at low exposure levels, increase the possibility of generating breast cancer [YM12]. Moreover, mammogram tests induce as well discomfort and pain to the patient due to the pressure exerted on the breast structure, being more severe in smaller busts. While these tests focus on the detection and diagnosis of microcalcifications that might develop into malignant lesions, breast density could severely affects the visualization of such structures. Therefore, an alternative method less susceptible to the change of breast density is required for such cases.
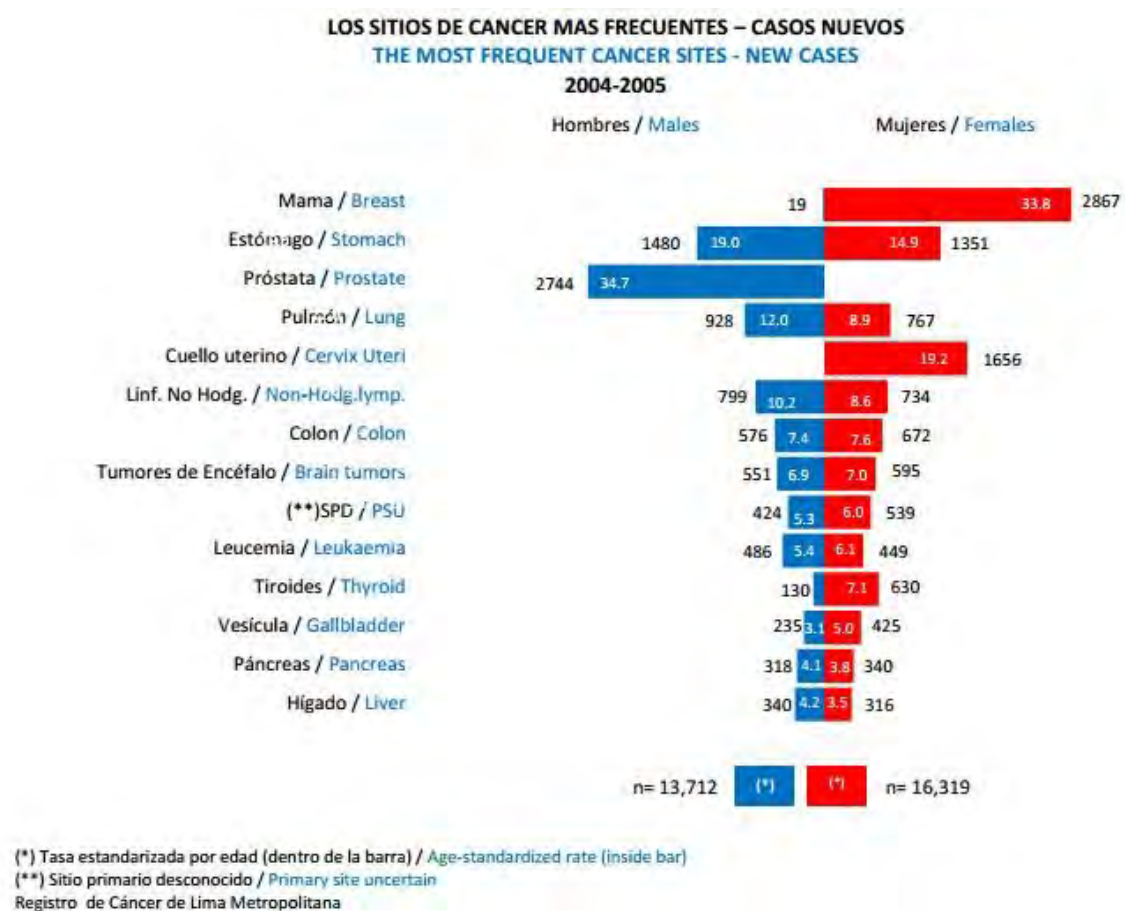

Figure 1.1: The most frequent cancer sites. Extracted from [dEN14]

1.1.2 Ultrasound and Elastography for tumor detection

In the field of medical imaging, mammography correspond to a modality of x-ray examination oriented to breast tissue. Over the past few decades, due to the emergence of new technologies of stimulate the tissue, the research of new methods to represent

physical properties of an examined mass has increased considerably [OAG+99]. Currently, computed tomography (CT) and magnetic resonance imaging (MRI) provide improved spatial resolution and tissue differentiation but require high implementation cost as well as long examination time (i.e. 20 min) in the case of MRI. On the other hand, Ultrasound Imaging (US) stand out for being a remarkably lower cost technology that induces the patient with non-ionizing radiation, contrary to mammography. However, statistics from recent years show that the effectiveness of US to detect small (less than 0.5 cm) lesions in the breast is still lower than those found on mammography or MRI exams [GH12] [GSD+04].

Likewise, a modality labeled as elastography has been developed for MRI, optical tomography and US systems in order to estimate the elasticity of a body when subjected to excitation. Since two decades, several quantitative and qualitative elasticity techniques have been formulated and developed [PTG05]. In the case of US, these techniques consist on exciting the tissue with a certain mechanical force and analyze the tissue response over a period of time with ultrasonic pulse-echo data in order to depict an elasticity map of the examined region [CORP13]. Among these techniques, quantitative approaches help the radiologist to establish an even more accurate diagnosis since they do not depend heavily on the interpretation of the results or specialist's expertise but only on the numerical values of the properties provided in the elasticity image [CAW+09].

Elasticity imaging methods based on US often require several acquisition of radio-frequency data to assess the behavior of the tissue due to mechanical vibrations. While current US systems features models of quantitative and qualitative elasticity, new elasticity algorithms are commonly structured with numerous filtering and reconstruction stages. Thus, the long computational time for generating a single elasticity image greatly affects the implementation of suchs techniques on commercial US equipment. To overcome this problem, ultrafast acquisition procedures such as synthetic aperture imaging [YTY11] as well computation enhancement with Graphics Processor Units (GPUs) have been proposed and implemented on US-based elastography methods [TF14].

Over the past five years, in the Laboratory of Medical Imaging of Pontificia Univerisdad Católica del Perú (PUCP), the Crawling-Wave Sonoelastography (CWS) technique has been used to depict quantitative elasticity images of an examined tissue. However, to date it has not been reported the implementation of parallel processing algorithm of this technique with the aid of GPUs, allowing real-time visualization of elasticity images. This is one of the aspects that serves as the motivation of the current master
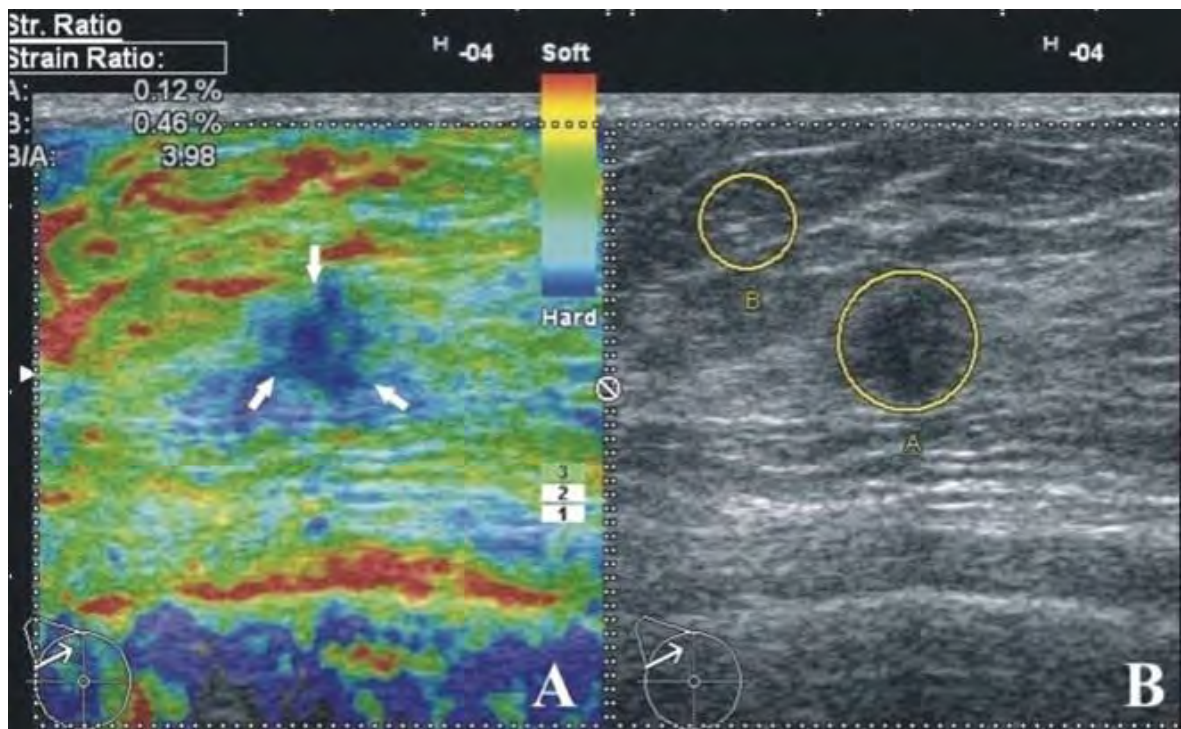
Figure 1.2: Example of elasticity image. (Left) Strain elasticity image of breast tissue. (Right) B-mode image of the same region. Extrated from [GSB11]

thesis.

On the other hand, in order to measure local shear wave speed (SWS) and reconstruct an elasticity image for CWS, a wide number of estimators have been reported in the literature. However, the presence of artifacts at the boundary regions as well as high estimation variance are still been observed in most of the reconstructed elasticity images. These artifacts might mislead the technician into the presence of stiffer masses, which compromise the accuracy of diagnosis. Therefore, a more robust algorithm for SWS estimation is constantly been researched, serving likewise as motivation of this study.

1.2 Objetives

Main

The main objective of the current thesis is the development and implementation of a quantitative imaging technique for generating elasticity images based on CWS in real time.

Specific

· Design a software featuring a Graphical User Interface (GUI) where elasticity estimates are displayed in real time.

· Use parallel processing capabilities of a GPU to improve performance of the algorithm and increase the number of frames per second.

· Implement the technique in an ultrasound research equipment and validate the results with gelatin-based elasticity phantoms.

· Develop a new SWS estimator and test its feasibility on simulated tissue phantoms and implement an optimization method for parameter determination of the new estimator

· Evaluate of both contributions (GUI and new SWS estimator) in gelatin-based phantoms generated in the lab.

· Evaluate of both contributions in calibrated elasticity phantom of homogeneous and inhomogeneous media.

2 Ultrasound Elastography

2.1 Introduction to Elastography

Elastography approaches are based on the elasticity equations derived from Hooke's law for a deformable body in order to measure the stiffness of a certain material. From the continuum mechanics theory, the conservation of momentum is presented on a certain volume of density ρ considering the surface forces T and body forces b as follows:

$$\frac{d}{dt}\iiint_{V} \rho u\, dV = \iint_{S} T^{(n)}\, dS + \iiint_{V} \rho b\, dV, \tag{2.1}$$

where u is the displacement vector and $T^{(n)} = \sigma \cdot n$ the traction vector expressed with the normal unit n and Cauchy stress tensor σ. Since body forces b slightly influence the estimation of stiffness, it can be removed from Eqn. 2.1. Then, the differential form of Eqn. 2.1 using the divergence theorem for the surface forces term is:

$$\rho \ddot{u} = \nabla \cdot \sigma \tag{2.2}$$

Following the constitutive equations of linear elasticity and considering an isotropic homogeneous media, the Cauchy stress tensor σ is defined as the inner product of the infinitesimal strain tensor ε and the fourth-order stiffness tensor C :

$$\sigma_{ij} = C_{ijkl}\varepsilon_{ij} \tag{2.3}$$

$$\varepsilon_{ij} = \frac{1}{2}(u_{i,j} + u_{j,i}) \tag{2.4}$$

$$C_{ijkl} = K\delta_{ij}\delta_{kl} + \mu(\delta_{ik}\delta_{jl} + \delta_{il}\delta_{jk} - \frac{2}{3}\delta_{ij}\delta_{kl}), \tag{2.5}$$

where δ_{ij} is the Kroneker delta and K and μ are the bulk and shear modulus, respectively. Then, combining the last three equation results in a simplified version (i.e. Hook's Law) presented as follows:

$$\sigma_{ij} = \lambda\varepsilon_{kk}\delta_{ij} + 2\mu\varepsilon_{ij}, \tag{2.6}$$

where λ is the first Lamé parameter. By replacing Eqn.2.6 in Eqn.2.1, a generalized equation for the dynamic response of a medium under any type of excitation force is derived:

$$\rho\ddot{u} = (\lambda + \mu)\nabla(\nabla \cdot u) + \mu\nabla^2 u. \tag{2.7}$$

Most of the elastography approaches focuses on the measurement of shear waves that propagate within a homogeneous material. In such cases, movement of shear waves are perpendicular to the displacement vector and thus, no deformation of volume is present, that is $\nabla \cdot u = 0$. Therefore, the dynamic response in terms of shear wave speed c_s^2 is:

$$\frac{1}{c_s^2}\ddot{u} = \nabla^2 u \tag{2.8}$$

$$c_s = \frac{\mu}{\rho}. \tag{2.9}$$

Finally, the shear wave modulus is related to the Young's modulus E and Poisson's ratio v, where this last parameter is typically found between 0.49 and 0.5 on biological tissues. Assuming $v = 0.5$, an approximation of the SWS is established for stiffness determination of a certain material:

$$\mu = \frac{E}{2(1 + v)} = \frac{E}{3} \tag{2.10}$$

$$c_s = \frac{E}{3\rho} \tag{2.11}$$

This Young modulus E, like the Poisson's ratio v and viscosity, is one of the biomechanical properties that is affected due to pathologies in an examinad tissue, which provides useful clinical information such as the mass density and stiffness [Duc90]. Among these changes of properties, increased stiffness are commonly related to abnormalities in soft tissue, leading to benign tumors or cancer. For those pathologies, conventional diagnosis procedures often appeal to palpation routines where technicians qualitatively evaluate the relative stiffness of a tissue region from its vicinity [GPAL95]. By applying a controlled pressure in the overlaying tissue, physicians have widely used this technique for centuries as a reliable tool for tumors and cancer detection. In

particular cases, however, this might be challenging task due to the lesions disperse morphology, small size and/or deep location, leading to assessment errors [GFI03]. In addition, the diagnosis accuracy is directly correlated with the physician's background expertise which could underestimate or overestimate malignant structures.

The goal of elastography is, therefore, to provide accurate Young's modulus information in an elasticity map, overcoming the limitations described above. Likewise, imaging new biomechanical properties combined with existing modalities in several medical imaging systems, such as MRI, CT and US, would be beneficial for diagnosis improvement and reliability.

2.2 Methods of Ultrasound Elastography

During the past two decades, several qualitative and quantitative methods of tissue elasticity techniques have been formulated and developed [PTG05]. For instance, qualitative approaches such as strain elastography produce a relative elasticity image where accuracy of the estimation is strongly dependent on an excitation force controlled by the radiologist [CORP13]. In contrast, as mentioned in Chapter 1, quantitative elasticity imaging techniques benefits diagnosis accuracy by overcoming estimation errors produced by manual excitation or mislead interpretation of elasticity estimates[CAW+09]. Table 2.1 present the current quantitative techniques developed for ultrasound elastography.

Most quantitative techniques estimate the Young's modulus in relation to the SWS (typically between 1 m/s to 10 m/s) which propagates transversely to the direction of the force that is applied to the tissue. For instance, Shear Wave Elasticity Imaging (SWEI) induces acoustic radiation forces generated by a focused beam in the ultrasonic transducer as the vibration source and thereby the velocity of shear waves is estimated [RPR+12]. Supersonic Shear Imaging (SSI) techniques increase the speed of the supersonic wave excitation level in order to increase the propagation of shear wave and thereby improve the spatial resolution along the axial axis [BTF04]. Other methods, such as Transient Elastography (TE) measure the tissue response after applying an impulsive force, avoiding bias errors which are typically found in phase velocity estimation in external vibrations approaches [CWF99]. Likewise, bias are diminished in Single Tracking Location Acoustic Radiation Force Imaging (STL-ARFI) due to shear wave tracking in a single location using normalized cross-correlation [EM13].

While the excitation sources mentioned above originate from the transducer, prolonged exposure of high energy could develop into heating and cavitation in the ex-

Table 2.1: Main quantitative ultrasound-based elastography techniques developed in recent decades

Technique	Number of sources	Excitation type	Evaluated parameter
Shear Wave Elastography (SWE)	1-internal	acoustic radiation force	SWS
Vibro-acoustography (VA)	1-external	acoustic radiation force	ALR[a]
Transient Elastography (TE)	1-external	transient mechanical	SWS
Crawling Wave Sono-elastography (CWS)	2-external	sinusoidal vibration	SWS
Supersonic Shear Imaging (SSI)	1-internal	radiation force	SWS
Vibro-elastography (VE)	1-external	multi-freq vibration	LF[b]
STL-ARFI[c]	1-internal	acoustic radiation force	SWS

[a] Acoustic Local Response
[b] Local Frequency
[c] Single Tracking Location Acoustic Radiation Force Imaging

amined area. In contrast, Vibro-acoustography [FG99], Vibro-elastography [TSR06] and Crawling Wave sono-elastography (CWS) [WTRP04] techniques use external vibration sources of relatively low amplitude (5um - 1 mm) and frequency (20 Hz - 500 Hz). As stated in Chapter 1, research on CWS has been conducted in the Laboratory of Medical Imaging of the Pontifical Catholic University of Peru for the past five years. Following this framework, the CWS method is selected for quantitative elastography estimation as further contribution to the research group in the current thesis work.

2.3 Crawling Wave Sono-elastography

This technique, proposed by Wu *et al.*, estimates the shear wave speed of a material by the analysis of a moving interference pattern generated from the opposition of two mechanical vibration sources. The main advantage of CWS is that the SWS can be scaled and controlled by the offset frequency between the sources, allowing its visualization on commercial US systems in the Color Doppler modality [WTRP04].

Studies of CWS feasibility and performance has been validated in several ex vivo experiments. For instance, Castaneda *et al.* [CAW+09] reported stiffness differentia-

tion between cancerous and normal tissue in prostate with 80% accuracy. Likewise, Hoyt *et al.* [HCP08] generated 3D reconstruction of porcine liver with consistent lesion boundaries. Additionally, CWS has proven appreciable differentiation of shear modulus in relaxed and contracted human skeletal muscle, making it feasible for in vivo characterization [HCP07]

2.3.1 Theory

The conventional CWS setup applied in a tissue-mimicking phantom is showed in Fig. 2.1. Two mechanical sources are placed on opposite lateral sides of an examined tissue. Sinusoidal vibrations with relative low amplitude (1um - 5 um) and frequency (150 Hz - 500 Hz) are induced through medium, parallel to the transducer beam direction, with an offset frequency Δf between the sources.
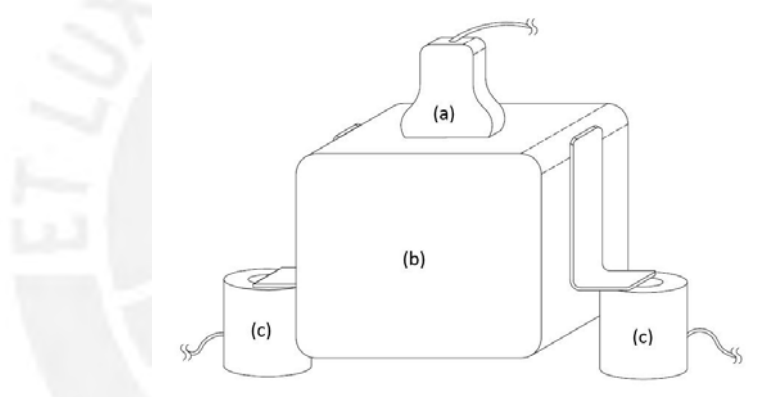

Figure 2.1: Conventional CWS setup. (a) Ultrasonic transducer, (b) Tissue mimicking phantom and (c) Vibration sources.

Considering a large distance between the sources and the Region of Interest (ROI), plane wave condition is achieved and the shear wave behavior for each source along the lateral axis x is described as follows:

$$S_r(x, t) = e^{-a_c(\frac{D}{2}+x)} e^{-i(k(x+\frac{D}{2})-\omega t)} \tag{2.12}$$

$$S_l(x, t) = e^{-a_c(\frac{D}{2}-x)} e^{-i((k+\Delta k)(x+\frac{D}{2})-(\omega+\Delta\omega)t)} \tag{2.13}$$

$$\Delta k = \frac{\Delta\omega}{c_s} \tag{2.14}$$

where D is the distance between the sources, a_c the attenuation of the medium, k the wave number, ω the vibration frequency in rad/s and $\Delta\omega$ the offset frequency between

the sources. With the superposition of both signals, the resulting envelope $|u(x,t)|^2$ of the interference pattern is:

$$|u(x,t)|^2 = 2e^{-a_c D}[\cos(2k + \Delta k)x + \Delta \omega t] \tag{2.15}$$
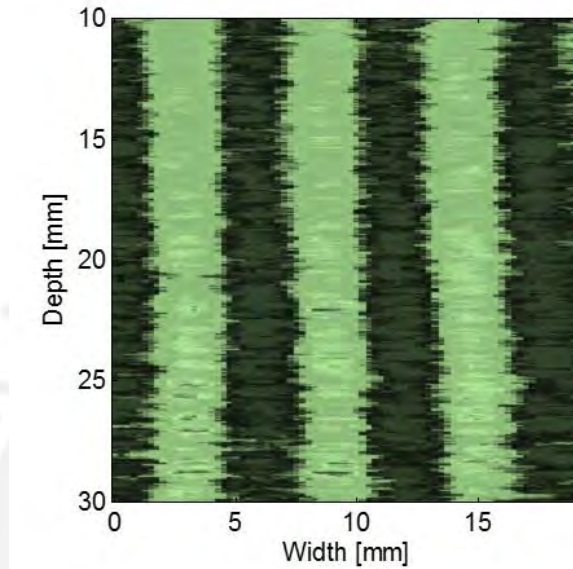

Figure 2.2: Crawling waves pattern in an medium with homogeneous stiffness

From Eqn.2.15 it can be derived that the spatial frequency of the crawling waves in homogeneous ($\Delta k = 0$) and static condition ($t = 0$) is $2k$, which represents half of the wavelength λ between peaks. Then, the shear wave velocity is calculated as:

$$c_s = \lambda f \tag{2.16}$$

Given that $\Delta \omega$ is positive and orders of magnitude lower than ω, the interference pattern (see Fig.2.2) moves towards the source with lower frequency at an apparent speed v_p proportional to the shear wave speed c_s. Furthermore, this approximation is also achievable at local regions, allowing the generation of a SWS image (proportional to the Young Modulus E) in a medium with increased stiffness.

$$v_p \approx \frac{\Delta \omega}{2\omega} c_s \qquad \omega >> \Delta \omega \tag{2.17}$$

2.3.2 Shear Wave Speed Estimators

A large variety of SWS estimators have been developed for CWS. Initially, Wu *et al.* [WTRP06] applied a local frequency estimator (LFE) based on filter banks to assess CrW spatial frequency while Zhang *et al.* [ZCW⁺07] calculated it with an implemented semi-automatic interface based on pattern recognition, where the user inputs a desired ROI and the software calculates the spatial displacement of CrW. Similarly, other estimators focus on phase derivation measurements along slow time (i.e. a certain number of acquired frames) [LMRT10] and lateral dimension [HHM⁺12] to compute 1-D velocity maps. The Phase Derivative (PD) estimator proposed by Hah *et al.* consists of assessing the wave number $k(x)$ of Equ.2.15 by recovering the phase $\theta(x)$ pixel-wise through the slow time dimension:

$$\theta(x) = 2 \int_0^x k(x)\,dx + \text{constant} \tag{2.18}$$

$$k(x) = \frac{\theta^j(x)}{2}, \quad \omega_0 = 2\pi(f + \Delta f) \tag{2.19}$$

$$c_s(x) = \frac{2\omega_0 T_x}{\theta^j(x)} = \frac{2(2\pi(f+\Delta f))\,T_x}{\theta^j(x)} \tag{2.20}$$

where T_x is the pitch or the lateral sampling of the transducer. Likewise, Hoyt *et al.* proposed a real-time 2-D and 1-D based on autocorrelation techniques [HCP08]. The 1-D estimation takes into account the converted analytic signal $\hat{u}(x)$ from the Hilbert transform $H(u(x))$ along the lateral dimension in order to acquire the local phase θ over a windows N with a lag-1 autocorrelation function:

$$\hat{u}(x) = H(u(x)) = u(x)(1 + \frac{1}{\pi x}j) \tag{2.21}$$

$$\hat{\gamma}(n^j, n) = \sum_{n=0}^{N - n^j - 1} \hat{u}(n)_* \hat{u}(n + n^j), \quad n^j = 1 \tag{2.22}$$

$$c_s(x) = |2\pi(2f + \Delta f)T_x / arctan(\frac{Im[\hat{\gamma}(1, x)]}{Re[\hat{\gamma}(1, x)]})|, \tag{2.23}$$

where $*$ denotes the complexo conjugation operator.

2.4 GPU Applications

Due to the high demand of processing performance and visualization in the video game industry, the parallel computing potential is massively increasing in current processors,

both in PC and specialized equipment of the automation [XPKB09], spatial location and medical industry [SDS14]. These new parallel processing units (i.e. GPUs) feature thread execution with thousands of cores simultaneously, since the data to be processed is distributed to a large number of processors unlike the previous scheme where a single processor performed reconstruction of the entire image.

Given that applications of new imaging modalities in ultrasound systems significantly benefit several clinical procedures and diagnosis, research on real-time elastography systems development has been widely studied and reported in the literature [ADP12][MTB+09]. Particularly, strain elastography as well as Acoustic Radiation Force Imaging (ARFI) have been successfully implemented and standardized on well-known ultrasound equipments [RBF+08][YDR11]. Similar to ARFI, algorithms of high computational complexity found in other approaches suchs as vibroelastography and CWS require fast computing architectures that can cope with the acquisition rate provided by the imaging equipment to allow the develpment of real-time applications.

In the last ten years, the medical imaging has been enhanced with new methods of parallelism using GPUs, featuring thread execution with thousands of cores simultaneously and thus, increasing the temporal resolution of the reconstructed images. For instance, multiple GPUs were programmed in the framework of Yiu *et al.* in order to beamform Plane Wave Compounding (PWC) and Synthetic Aperture Imaging (SAI) at an ultra-fast frame rate of 3000 fps [YTY11]. Likewise, they presented real-time operational feasibility of Minimum Variance (MV) beamforming with a GPU-based imaging system [YY15]. Computing enhancement was also reported in other ultrasonic techniques such as Tridimensional Ultrasonic Computed Tomography (3D USCT), where Birk *et al.* developed a heterogeneous hardware conformed of ten FPGA and six GPU to accelerate the processing time by a factor of 7 [BKF+13]. Regarding elasticity imaging modalities, Idzenga *et al.* evaluated the performance of normalized cross correlation algorithms, widely used in strain elastography, implemented on GPUs and OpenMP (multiple CPU's) and obtained an improvement factor that ranged from 132 to 376 [IGV+14]. Furthermore, 3D remote reconstruction of strain elastography was reported in Chen *et al.* [CCH16] with the aid of graphics cards. Rosenzweig *et al.* used GPU's to reduce the processing time Loupas's auto-correlator, generating ARFI in real time [RPN11]. In similar techniques, Baghani *et al.* built a vibro-elastography "free-hand" system in real-time using commercial GPUs, reporting an improvement of 32 in computational time rate [BEW+12]. Finally, in CWS, Hoyt *et al.* recently presented a new method to generate images with reduced computational time while maintaining the image quality [HPR07]. However, to date it has not been reported the

implementation of parallel processing algorithm of this last technique, which is yet to be adapted in practice.

3 Methodology

In this chapter, the complete methodology for the GUI implementation, SWS estimator and phantom generation for validation experiments is presented.

3.1 Graphical User Interface for Real-Time Quantitative Elastography

A quantitative elastography imaging system was implemented on a commercial US scanner using GPU resources in a C++ environment. The system was initially oriented to characterization of tissue elasticity in regions where normal or conventional excitation for crawling wave generation is feasible (such as breast or muscle tissue).

3.1.1 Hardware Configuration

The interface was programmed in a SonixTouch research US system (Ultrasonix[®] S.A., British Columbia, Canada), which featured the typical imaging modalities used in clinical procedures: B-mode for acoustic impedance of tissue in real-time, Power Doppler for blood flow imaging, Pulsed Wave Doppler for cardiac cycle monitoring and M-Mode for structure movement over time. Likewise, a linear array transducer (L14-5/38) was connected to the US equipment, generating focused ultrasound beams and receiving the backscatter signal of the examined tissue, which are delivered to the US system and processed in order to depict an image. Hardware specifications of the SonixTouch and transducer are presented in Table 3.1 and Table 3.2. Then, in order to enhance the system processing speed of image reconstruction, a GTX 750M (NVIDIA, Santa Clara, California, USA) was installed and replaced for the default display adapter on the CPU, enabling parallel execution of a set of instructions (see specifications on Table 3.3).

Table 3.1: Hardware features of SonixTouch

Parameter	Value	Units
Processor clock	3.10	GHz
Random Acces Memory	2.99	GB
Number of cores	4	-
Cache Memory	4	MB
Screen resolution	1280 x 1024	pixels

Table 3.2: Hardware features of transducer L14-5/38

Parameter	Value	Units
Frequency range	14 - 5	MHz
Central frequency	7	MHz
Number of elements	128	-
Pitch	0.308	mm
Geometric focus	16	mm
Elevation Aperture	4	mm
Physical Foot Print	4 x 39	mm
Steered Angle	17.5	°
Doppler Frequency	4	MHz
Focal range	2 - 9	cm

3.1.2 Software Design

Currently, the SonixTouch features WindowsXP embedded operating system (32-bits). Therefore, most of the applications for GUI design are limited and require certain downgrade due to the compatibility. In this work, the following tools were used for the GUI programming.

- Cmake 3.2.0: cross-platform, open-source build system that generates visual studio 2010 solutions.

- Visual Studio 2010 Professional: robust application development tool for C-based (CUDA) and C++ programs compilation and debugging.

- QT 4.8.6: application development tool that offers build-in libraries for graph-

Table 3.3: Hardware features of GTX 750M

Parameter	Value	Units
Processor clock	941	MHz
Random Acces Memory	2048	MB
Number of cores	384	-
Memory Clock	1250	MHz
Compute Capability	3.0	-
Memory Bandwidth	80	GB/sec

ical user interface.

- SonixRP 6.0.7: software development kit that enables communication and control of the imaging parameters, elements and buffer of the ultrasound system.

- CUDA 4.0: C programming model designed for graphical processing units.

- Matlab 8.5.0.197613 (testing and validation): technical-computing environment suitable for algorithm simulation, modeling and matrix operation.

The layout of the GUI is presented in Fig. 3.1 as a Windows application form and the generalized main flowchart is showed in Fig. 3.2. Three main buttons controlled the imaging flow (see Fig. 3.1.A). The initialization button set up the firmware and license file in order to open communications with the US system as well as initialize classes and variables of the main function. Once the initialization is complete, a set of probes currently installed will be displayed at the left side (see Fig. 3.1.B). By selecting the probe, the default preset configuration is loaded and the thread instance for US control (drived by the SDK Porta) is started. The start button initiates a loop sequence of color radio frequency (CRF) data acquisition. Then, kernel functions defined in the GPU are called in order to process each step of the crawling wave sonoelastography algorithm using the phase derivative (PD) estimator. The resulting SWS image is depicted in the center of the GUI (see Fig. 3.1.C) where the user is able to establish the ROI around the imaging zone. Since memory allocation is executed at the initalization of the GUI for efficiency purposes, modification of US parameters that might change the buffer size is allowed only when the system is not imaging or capturing data; thus, it is necessary to stop the imaging first. Additionally, the idle state offers storage options for each of the processing stages of CWS (described in the

following subsections), saving the data in binary files which can be later analyzed in the MATLAB environment.
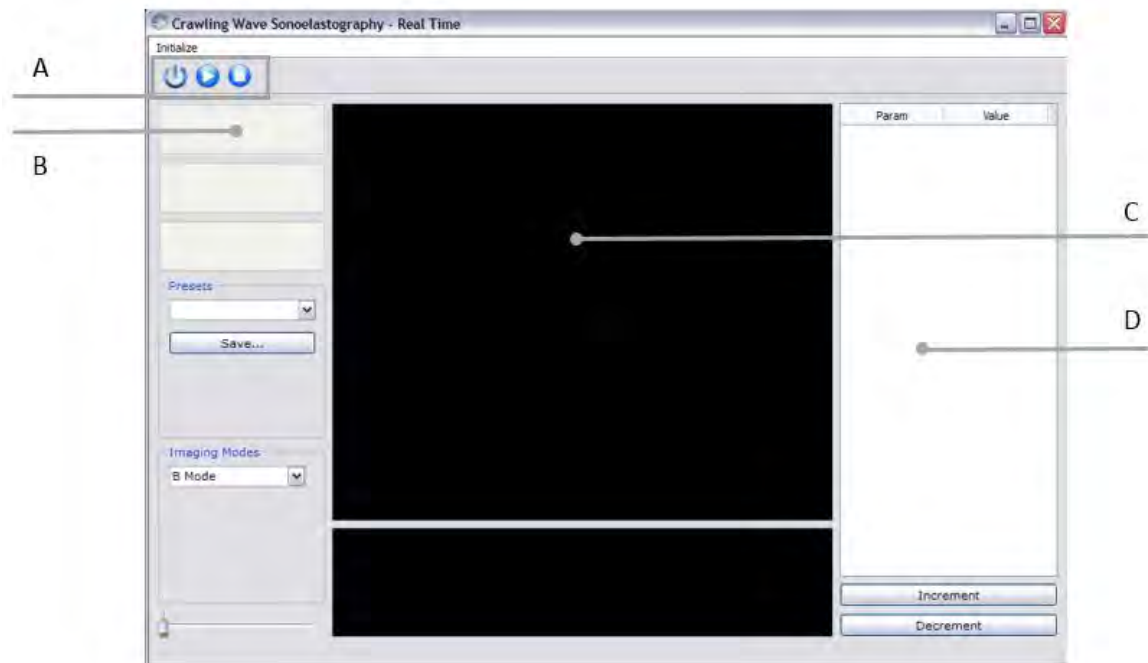

Figure 3.1: GUI for quantitative ultrasound elastography. A: Initialization, Start and Stop button. B: Probe selection and default preset configuration. C:Display of elasticity images in duplex mode with B-Mode acquisitions. D: Control parameters.
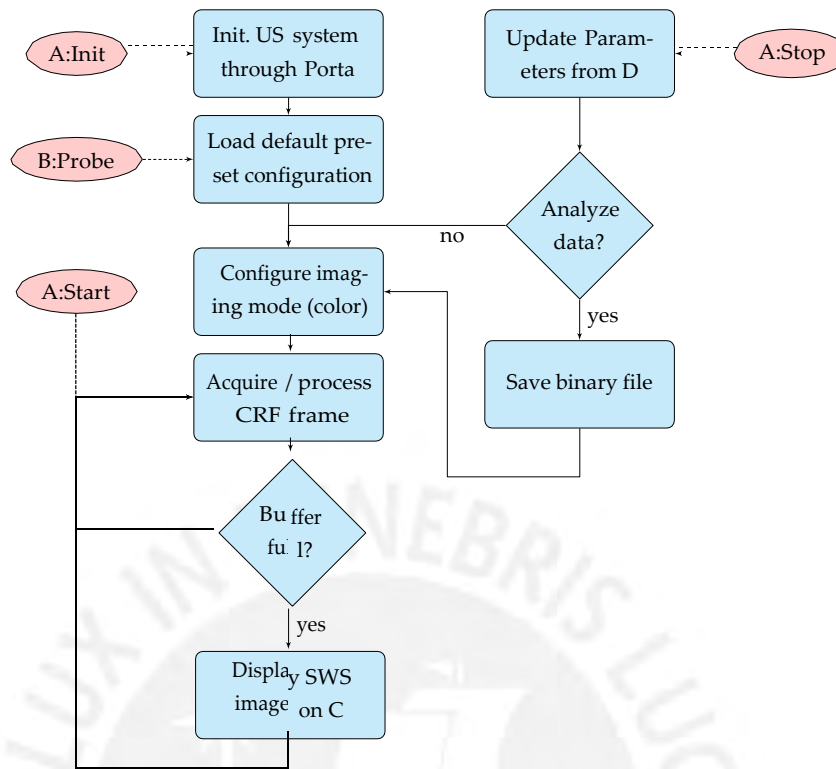
Figure 3.2: Main flowchart of the quantitative elastography GUI

3.1.3 In-phase Quadrature process

A CRF frame is conformed from a set of scan lines, each of them recorded several times in an ensemble package over a short period of time for tracking purposes. This CRF frame is acquired from the Sonixtouch and stored in a host computer buffer with a M x N format, where M represent the number of axial samples acquired and N is the number of scan lines multiplied times the ensemble package. The first stage consist on converting the radio-frequency signals to complex signals (i.e. In-phase Quadrature or IQ data) using a Hilbert transform. Due to the limitations on the maximum number of threads per blocks, the data is distributed in N Blocks of M threads each (see Fig. 3.3) for faster computation. The reason behind this is that in IQ processing, lines are independent from each other as well multiple acquisition of each (ensemble), so they can be put in separate blocks, otherwise synchronization would be more resource-consuming. Moreover, a low pass filter used at the end of the process requires synchronization between each sampling along a single line. Hence, all samples of a single line should be loaded in threads of the same block.
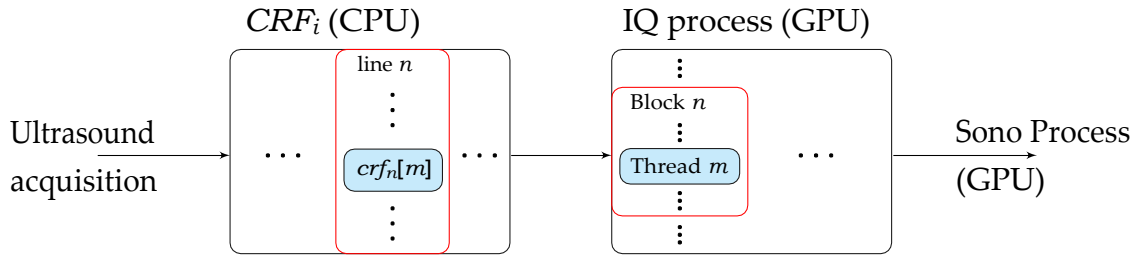
Figure 3.3: In-phase Quadrature process: GPU distribution

The IQ processing in the GPU is presented in Fig. 3.4. Inside each thread the signal is down-mixed into a complex signal, which is achieved by multiplying it with two sinusoidal signals phased 90° between each other: $-\sin(2\pi f_d t_n)$ and $\cos(2\pi f_d t_n)$, where f_{down} is the down-mixing frequency, set equally to the transmit color frequency (i.e 6.6 MHz), and t_n is the time of flight consumed by the signal to reach the scatter n, which is calculated from the distance of the scatter to the transducer ($r(n)$) and speed of sound in the medium (c = 1540 m/s): $t_n = 2r(n)/c$. These parameters are constantly being refreshed by the ultrasound system in every acquired CRF frame. Then, a low pass filter (LPF) is applied using zero-phase filtering on both direction in order to remove the negative spectrum and noise outside the bandwidth. The LPF coefficients (b_0, b_1, b_2) are obtained from the design of a 2nd order FIR filter using Hamming windows with cut-off frequency set to 60% of the signal bandwidth. However, since the LPF is applied along a single CRF line, all samples must have been already converted to complex signal. To ensure this assumption, a synchronization step is added before the LPF filter.
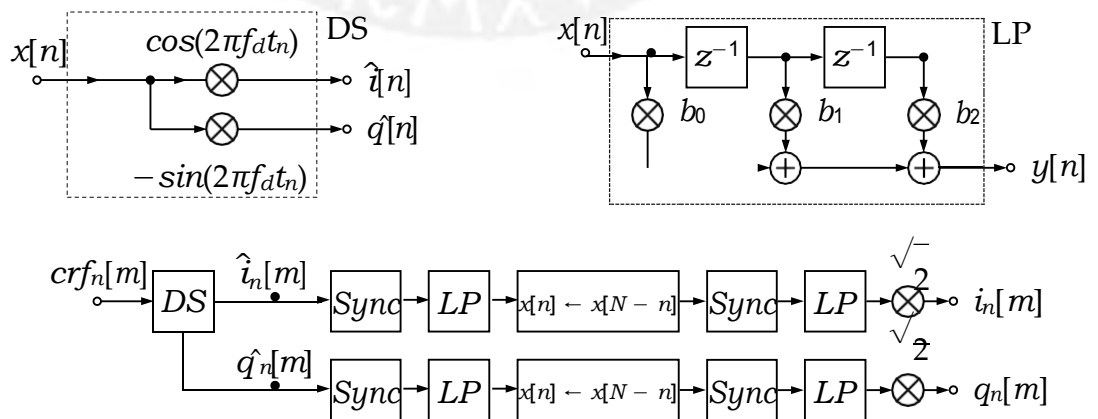

Figure 3.4: In-phase Quadrature process: Flow diagram

3.1.4 Spectral Doppler variance estimator

In order to visualize the interference patterns and generate a sono-elasticity video, the spectral variance spectrum (σ^2) in an ensemble package of size P is calculated for every pixel of each acquired frame. Since the operation is conducted inside an ensemble package and independently through pixels, each ensemble vector of a pixel s_{mn} is send to a block in the GPU architecture, running M x N blocks, where M and N are the number of CRF samples and lines (ensemble excluded), respectively.
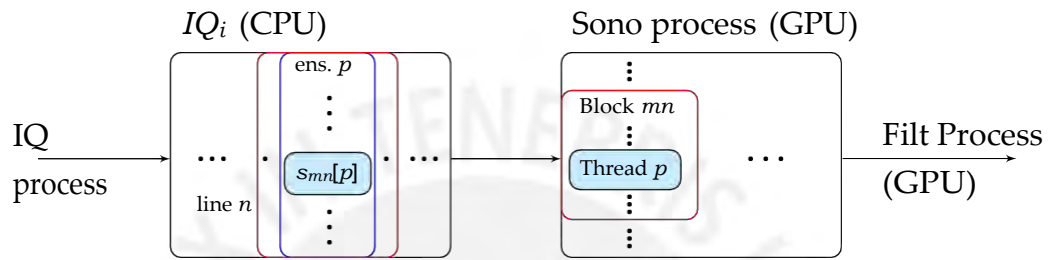
Figure 3.5: Sonoelastography process: GPU distribution

Here, the spectral moment estimator proposed by Miller *et al.* [MR72] is computed at the pulse repetition period (PRP) of the analytic IQ data, which is inputed as a complex $s(m, n)$ matrix. Prior to the calculation, a wall filter (w_f = [0.525, −0.475]) is applied to reduce the DC level. The algorithm is presented as follows:

$$u[m, n] = \sigma^2(m, n) = \frac{2}{P\,RP^2}(1 - \frac{|R_{PRP}(m, n)|}{R_0(m, n)}) \tag{3.1}$$

being R_0 and $R_{P\,RP}$ are correlation functions and at lag $t = 0$ and lag $t = P\,RP$, respectively, defined as:

$$R_{PRP}(m, n) = \frac{1}{P}\sum_{p=1}^{P-1} s_{mn}[p]s_{mn}[p+1]^* \tag{3.2}$$

$$R_0(m, n) = \frac{1}{2P}\sum_{p=1}^{P-1} [\,s_{mn}[p]^2 + s_{mn}(p + 1)\,^2] \tag{3.3}$$

$$s_{mn} = i_n[m] + j.q_n[m] \tag{3.4}$$

where P is the ensemble length once the wall filter is applied, $*$ the complex conjugation operator, and s_{mn} the complex vector at pixel in sample m and line n.

3.1.5 Sonoelastography filtering

Sonoelastograms obtained from Miller's estimator are further processed with a [3x3] median filter (see Alg.1)for noise reduction. However, extrapolation at boundary regions were not taken into consideration in order to reduce computation time in the GPU. The filtered sonoelastograms are then stored in a circular buffer, which is located in the host computer and is initialized with a fixed number of I frames (i.e. 50 frames). Once the buffer has been completely filled, a normalization stage is conducted over the complete sonoelastography video.

$$u[m, n, i] \quad \boxed{Avg_I} \quad - \quad \boxed{M} \quad u_I[m, n] \quad \boxed{Max_N} \quad \frac{1}{u_{NI}[m]} \quad \hat{u}[m, n, i]$$

$$- u[m, n]$$

Kernel 1 \qquad Kernel 2 \qquad Kernel 3
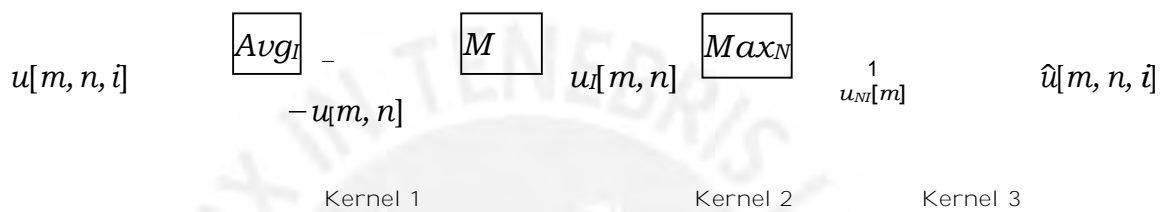
Figure 3.6: Filtering process: Flow diagram

Algorithm 1: Median filter of kernel 3 x 3 computed in each thread

Input : index: sample m, line n
Output: Median value in a 3 x 3 grid
$\qquad$ around input index
$\quad w[0...8], i \leftarrow 0$
$\quad$ for $x = m - 1$ **to** $m+1$ **step** 1
$\quad\quad$ do if $x > 1$ **and** $x < M$ then
$\quad\quad\quad$ for $y = n - 1$ **to** $n + 1$ **step** 1
$\quad\quad\quad\quad$ do if $y > 1$ **and** $y < N$ then
$\quad\quad\quad\quad\quad w[i] \leftarrow u[x, y];$
$\quad\quad\quad\quad\quad i \leftarrow i + 1;$
$\quad\quad\quad\quad$ end
$\quad\quad\quad$ end
$\quad\quad$ end
$\quad$ end

for $j = 0$ **to** 4 **step** 1 do
$\quad i \leftarrow j;$
$\quad$ for $l = j + 1$ **to** 8 **step** 1 do
$\quad\quad$ if $w[l] < w[i]$ then
$\quad\quad\quad i \leftarrow l;$
$\quad\quad$ end
$\quad$ end
$\quad t \leftarrow w[j];$
$\quad w[j] \leftarrow w[i];$
$\quad w[i] \leftarrow t;$
end
$\hat{u}[m, n] \leftarrow w[4];$

For every depth, a slice of N (lines) x I (frame) pixels is taken and processed. First, the DC component of each lateral pixel is removed by calculating the mean vector of the slice along the slow time and subtracted from it. Then, normalization is conducted over the entire slice. However, due to limitations in the number of threads per block that the current GPU provides, the total number of elements on each slice is usually

higher than the maximum block size, restricting the whole synchronization between threads. Hence, the normalization process is divided in three kernels (grids) in order to properly calculate the maximum value of each slice. Calculation of average and maximum value of a vector is achieved using a well-known parallel reduction process [RK10]. Fig. 3.7 depicts the first step of average estimation where the new result is stored in the first half of the vector. Therefore, after log_2N steps, the final result is read from the first sample. As observed in Fig. 3.7 for instance, average of a certain vector is calculated as: $Avg_N = x_1/N$.
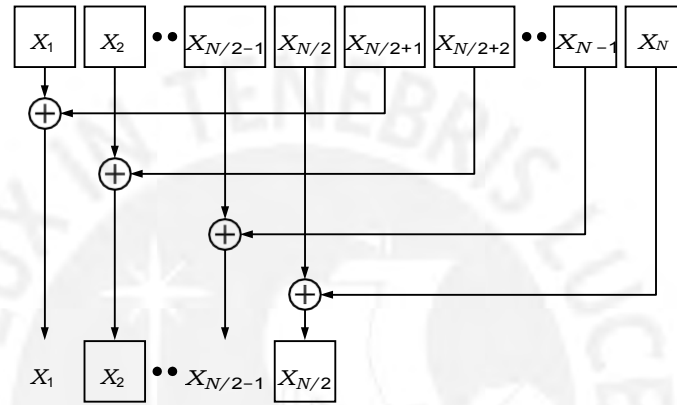
Figure 3.7: One step of summation reduction, storing each sum on elements of the same vector

3.1.6 Phase derivative estimator

In this part, the SWS values are calculated using the phase derivative estimator. First, the sonoelasticity video is reordered according to the index of the last acquired frame, which is constantly read from the system and send to the GPU kernel function. Then, the Fast Fourier Transform (FFT) Ψ_{mn} is computed over the signal ψ_{mn} in the slow time dimension (frames) employing build-in CUDA libraries for each pixel in the M x N grid. Since the whole interference patterns moves at a constant speed proportional to the offset frequency Δf, the FFT displays a peak temporal frequency where the initial angle of the current pixel can be estimated a $\theta = arctan(Img(\Psi_{mn}[f_t * I])/Re(\Psi_{mn}[f_t * I]))$. This temporal frequency f_t is defined as:

$$f_t = \Delta_f/T_n \tag{3.5}$$

where T_n is the frame rate, given by the research ultrasound system. The sonoelasticity video is therefore reduced to a $M \times N$ 2-D phase map $\theta(m, n)$, from which the SWS values are inversely proportional to the spatial derivative of the phase along the lateral direction:

$$c_s[n,m] = \frac{2(2\pi(f + \Delta f))T_x}{\theta[m,n] - \theta[m,n+1]}. \tag{3.6}$$

In order the properly compute the denominator in Eqn. 3.6, function θ needs to remain continuous along the lateral direction. Hence, an unwrap process is conducted before the SWS estimation in every depth of the 2-D phase map, removing leaps between maximum and minimum phase and generating a continuous slope function θ (see Alg. 2).

Algorithm 2: Unwrap filter computed in each thread

Input : index: sample m, line n
Output: unwraped phase $\bar{\theta}[m,n]$

$\Delta\theta \leftarrow \theta[m, n] - \theta[m, n - 1]$
$c \leftarrow 0$
if $\Delta\theta < 0$ then
   $s[m,n] \leftarrow 1;$
   $\Delta\theta \leftarrow |\Delta\theta|;$
end
else
   $s[m,n] \leftarrow -1;$
end

if $\Delta\theta >= \pi$ then
   $p[m,n] \leftarrow 1;$
end
else
   $p[m,n] \leftarrow 0;$
end
Synchronize();
for $j = 1$ **to** n **step** 1 do
   $c \leftarrow c + 2\pi s[m, j]p[m, n];$
end
$\bar{\theta}[m, n] \leftarrow \theta[m, n] + c;$

In spite of the previous filter applied to the CrW data in Section 3.1.5, θ is usually coupled with noise, requiring some degree of additional smoothing to avoid amplified errors in the lateral derivative [HHM+12]. Here, a local regression algorithm is implemented element-wise using the weighted coefficients and a 2nd order polynomial fit.

$$w_i = (1 - (\frac{|x_i - x_n|}{h})^3)^3 \tag{3.7}$$

$$\hat{\beta} = \underset{\beta_0, \beta_1, \beta_2}{\mathrm{argmin}} \sum_{i=h_1}^{h_2} w_i[\theta_i - (\beta_0 + \beta_1 x_i + 1/2\beta_2 x_i^2)]^2 \tag{3.8}$$

$$h = h_2 - h_1 \tag{3.9}$$

$$\hat{\theta}_n = \hat{\beta}_0 + \hat{\beta}_1 x_n + 1/2\hat{\beta}_2 x_n^2 \tag{3.10}$$

Taking the partial derivatives $\partial/\partial\beta_i$ from Eqn.3.10, a system of equation is generated and the optimal fitting coefficients are estimated as:

$$\hat{\beta_2} = \frac{P_1^2 P_2 P_6 - P_1 P_2^2 P_5 + P_0 P_2 P_3 P_5 - P_0 P_2^2 P_6 + P_2^3 P_7 - P_1 P_2 P_3 P_7}{P_2^2 - P_0 P_2 P_4 - 2P_0 P_2 P_3 + P_1^2 P_2 P_4 + P_0 P_2 P_3} \tag{3.11}$$

$$\hat{\beta_1} = \frac{P_1 P_7 - P_0 P_5 - 1/2(P_1 P_2 - P_0 P_3)\hat{\beta_2}}{P_1^2 - P_0 P_2} \tag{3.12}$$

$$\hat{\beta_0} = \frac{P_7 - 1/2 P_2 \hat{\beta_2} - P_1 \hat{\beta_1}}{P_0} \tag{3.13}$$

where:

$$P_0 = \sum_{i=h_1}^{h_2} w_i \quad P_1 = \sum_{i=h_1}^{h_2} w_i x_i \quad P_2 = \sum_{i=h_1}^{h_2} w_i x_i^2 \quad P_3 = \sum_{i=h_1}^{h_2} w_i x_i^3 \tag{3.14}$$

$$P_4 = \sum_{i=h_1}^{h_2} w_i x_i^4 \quad P_5 = \sum_{i=h_1}^{h_2} w_i x_i y_i \quad P_6 = \sum_{i=h_1}^{h_2} w_i x_i^2 y_i \quad P_7 = \sum_{i=h_1}^{h_2} w_i y_i \tag{3.15}$$

3.1.7 Color pixel mapping

Once the elasticity map is constructed, shear wave speed values are normalized over a user-defined dynamic range delimited by a maximum (e_h) and a minimum (e_l) SWS value (i.e. e_l = 2 m/s, e_h = 6 m/s) and indexed to the hot-to-cold color map based on the RGB color space [Bou95], as showed in Fig. 3.8. Then, the SWS map is scaled in order to fit the screen resolution using nearest neighborhood interpolation. Finally, a post-processing median filter of kernel [3 x 3] is applied to the reconstructed image, reducing the artifacts produced by crawling waves of low SNR.
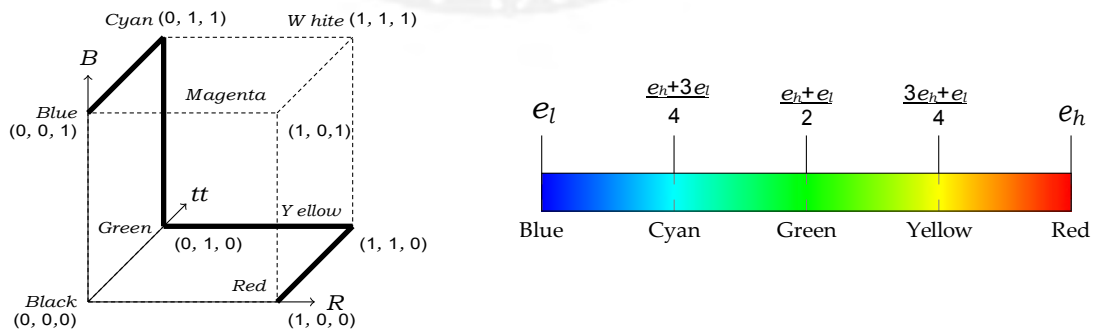
Figure 3.8: Hot and cold colormap based in the RGB colorspace

3.2 Regularized Wavelength Average Velocity Estimator

The proposed and developed SWS estimator, namely Regularized Wavelength Average Velocity Estimator (R-WAVE), is based on the conventional CWS setup and process the CrW video generated from the Spectral Doppler variance estimation (described in Chapter 2). The proposed estimator provides a resulting lateral vector of local SWS values by analyzing the displacement of the interference pattern in a lateral profile. Therefore, R-WAVE is computed over each slice across the lateral and temporal dimension in order to generate a complete SWS image.

Two of the most used shear wave speed estimators, the Phase Derivative (PD) and 1-D Hoyt (1DH), calculate the spatial frequency phase θ through autocorrelation windows in a single CrW frame and FFT in the slow time dimension, respectively. However, both presents limitations in their SWS estimation. On one hand, PD is sensitive to small errors in θ since it computes instantaneous change of θ along the lateral dimension. On the other hand, while 1DH estimate a more robust θ, it likewise reduce the effective size of the output SWS image due to the use of autocorrelation windows. Instead, R-WAVE measures the interference pattern wavelength directly through peak detections algorithm, reducing estimation variance of the final c_s map.

3.2.1 Moving Filter

As a pre-processing stage, a moving filter is implemented on each slide of depth (see Fig. 3.9) for signal-to-noise ratio (SNR) enhancement and suppression of reflection artifacts, following the framework of Castaneda *et al.* [CAW⁺09]. The filter is designed as a 2D bandpass centered at the normalized temporal frequency f_t and a selected spatial frequency range f_k. The first frequency depends on the offset frequency Δf and frame rate T_n, while the second is set according to the desired elasticity limits e_l and e_h as well as the lateral resolution T_x (pitch) and vibration frequency f. Additionally, it is worth highlighting the fact that f_k is actually the wavenumber of interference pattern, $\lambda/2$, as explained in section 2.3.1, thus the factor of 2 in Eqn. 3.17.

$$f_t = \frac{\Delta f}{T_n} \tag{3.16}$$

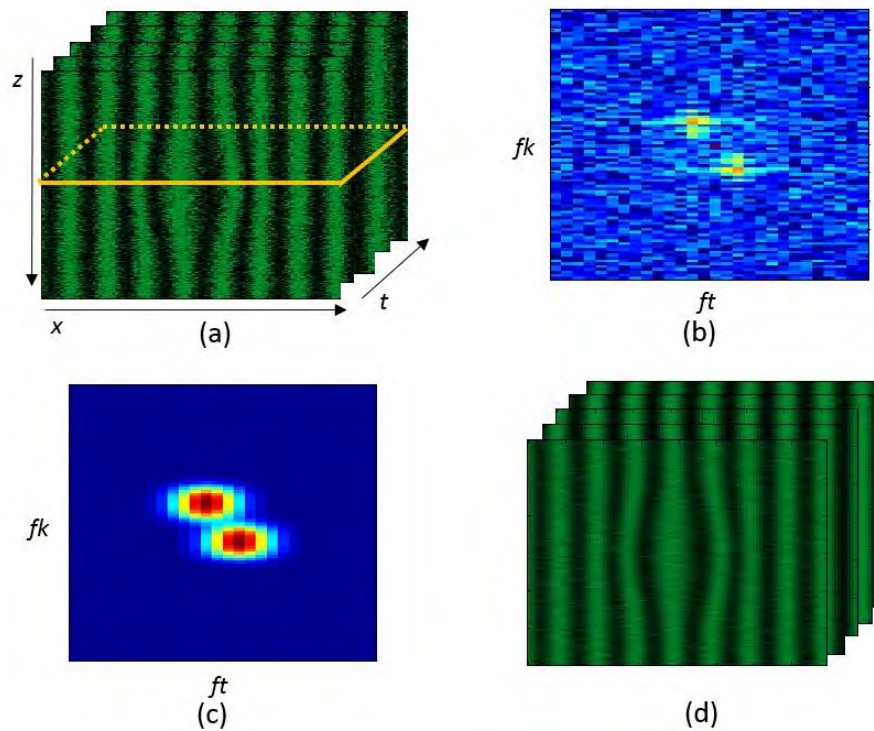$$f_k = [\, T_x \frac{2f}{e_h} \quad T_x \frac{2f}{e_l} \,] \tag{3.17}$$

Figure 3.9: Moving Filtering. (a) Simulated sonoelasticity movie showing the interference pattern with a 40% added noise. (b) 2D FFT of a slice selected in (a). (c) Motion filter with the desired special and temporal frequency. (d) Filtered sonoelasticity movie with reduced noise.

3.2.2 Linear Problem

The final step consist of finding the local $c_s(i, j)$ along the ROI for each i and j of the lateral and axial axis, respectively. From Eqn. 2.16, shear wave speed c_s can also be described as: $c_s = \lambda f$, where f is the vibration frequency induced into the tissue and λ is two times the lateral distance between peaks of the interference pattern which is assumed to be parallel to the axial axis. First, let x_j be an array of unknown c_s values at a certain depth j in the sonoelasticity movie along the lateral dimension. Then, analyzing the signal amplitude and inflection points, peaks are detected and indexed, thus the wavelength $\lambda/2$ is measured. In this process, the motion filter applied previously greatly benefits the accuracy of peak recognition and wavelength measurement. Through the analysis of Eqn.2.15 in a two-phase medium, the estimated shear wave speeds obtained from the measured wavelength $\lambda/2$ can be approximated to a linear fit as a weighted sum of the SWS elements contained in-between (see Appendix 1 for the detailed demonstration), as shown in Fig.3.10.

For every average c_s an equation is generated containing the involved elements x.
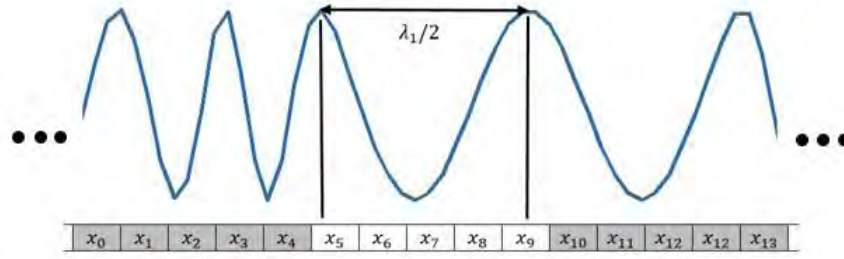
$$a_5x_5 + a_6x_6 + a_7x_7 + a_8x_8 + a_9x_9 = \frac{1}{2}\lambda_1 f = S_{av_1}$$

$$a_5 + a_6 + a_7 + a_8 + a_9 = 1$$

Figure 3.10: Interference pattern along the lateral dimension at a selected depth and frame. The distance between peaks is equal to half the wavelength of the weighted average shear wave speed

Boundary regions with no detected peaks in-between are filled with extrapolated c_s of the lateral profile. Repeating the same process over time acquisitions, the equation system is reduced to the form:

$$Ax_j = S_{av}, \quad A \in \mathsf{R}^{MxN}, x_j \in \mathsf{R}^{1xN}, S_{av} \in \mathsf{R}^{Mx1} \tag{3.18}$$

where A is the weighted coefficient matrix map, S_{av} the weighted average speeds and x_j the unknown shear wave speeds at depth j. For simplification purposes, let A be an equally distributed weighted coefficient matrix along the lateral dimension or rows (i.e. from Fig. 3.10: $a_5 = a_6 = a_7 = a_8 = a_9$, the real weighted values are calculated and explained later in section 3.2.4). Usually, the number of color frames acquired contains more than one cycle of the crawling pattern over the ROI. Therefore more equations than variables are found and an overdetermined system is generated.

3.2.3 Quadratic Programing and regularization

A useful approach to solve this problem is the quadratic programming (QP), which minimize an objective function from least square optimization (LSO) method:

$$QP_{x_j}(Ax_j = S_{av}) : min_{x_j} ||Ax_j - S_{av}||^2 = x_j^T A^T A x_j - 2Ax_j S_{av} + S^2_{av} \tag{3.19}$$

$$min_{x_j} ||Ax_j - S_{av}||_2 = \frac{1}{2}[x_j^T(A^T A)x_j] - [(S_{av}A)^T]^T x_j \tag{3.20}$$

$$min_{x_j} ||Ax_j - S_{av}||_2 = \frac{1}{2}x_j^T H x_j - f x_j \tag{3.21}$$

where $||.||$ is the euclidian norm, and H and f are know as the Hessian operator and linear term, respectively, which are constructed by the sum of the partial H and f from each row of A matrix and S_{av} :

$$H = \sum_{m=0}^{M-1} [a_{m1} a_{m(N-1)}]^T [a_{m1} a_{m(N-1)}] \tag{3.22}$$

$$f = \sum_{m=0}^{M-1} S_{avm}[a_{m1} a_{m(N 1)}] \tag{3.23}$$

For each depth j of the sonoelastography video, the QP approach will look for the solution x_j subject to equations/inequations restrictions (if any) under a determined number of iterations or if a tolerance condition is reached. The only restriction available for the present linear problem are the upper and lower bound of x, since the data has already been filtered by the desired SWS examination range in the pre-processing stage:

$$x_j \leq T_x \frac{2f}{e} \tag{3.24}$$

$$x_j \geq T_x \frac{2f}{e} \tag{3.25}$$

However, performance of QP in a quick simulation (see Table 3.4) of a homogeneous and inhomogeneous media using Eqn. 2.15 shows that the linear system is ill-conditioned and presents amplified noise in the solution (see Fig. 3.11). This is understandable since the exact position of each peak is rounded to the nearest index in the lateral vector, whose resolution is linked to the transducer pitch. The inaccurate peak location adds noise to the system and increase the conditional number of matrix A. Therefore, a regularization approach is required for stabilizing the solution.

One of the commonly used methods for regularization is the Tikhonov approach,

Table 3.4: Simulation Setup

Parameter	Symbol	Value	Units
Vibration frequency	f	200	Hz
Vibration offset frequency	Δf	0.4	Hz
Pitch	T_x	4.08	mm
Frame rate	T_n	8	Hz
Frames acquired	N	50	-
Elements / lateral samples	X	128	-
Axis samples	Z	1	-
Tissues shear wave velocity	SWS_l, SWS_h	[1;5], [3;3]	m/s
Distance between sources	D	50	mm
Attenuation coefficient	a_c	0.1	dB/MHz/cm
Cut-off SWS in motion filter	e_l, e_h	[0.5; 6]	m/s
SNR of added white noise	v	25	dB
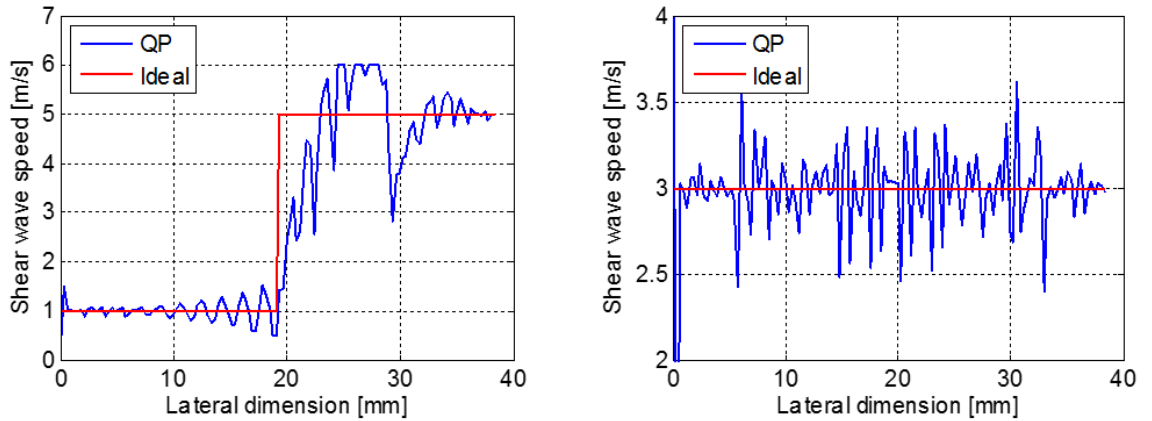
Figure 3.11: QP solution from simulated inhomogeneous (left) and homogeneous media (right) generated from Table 3.4 using Eqn. 2.15

which adds a penalty constrain in the minimization of the squared residuals of a linear system. Including this regularization term in the QP setting results:

$$min_{x_j} [||Ax_j - S_{av}||^2 + ||\Gamma x_j||^2] = x_j^T A^T A x_j - 2Ax_j S_{av} + S_{av}^2 + x_j^T \Gamma^T \Gamma x_j \quad (3.26)$$

$$min_{x_j} [||Ax_j - S_{av}||_2 + ||\Gamma x||] = \frac{1}{2}[x_j (A_T A + \Gamma_T \Gamma)x_j] - [(S_{av} A)^T]^T x_j \quad (3.27)$$

Similar to Eqn. 3.19, the constant S_{av}^2 is removed since it does not influence the

minimization process. Here, the new Hessian operator is $A^TA + \Gamma^T\Gamma$, where Γ is known as the Tikhonov matrix. Usually, the Tikhonov matrix is defined as a scaled identity matrix aI, adjusting the penalty with the regularization parameter a. However, since the elasticity of a certain tissue within a ROI remains uniform, a scaled high-pass operator (i.e. gradient operator ∇) is more suitable for the current ill-posed problem. Hence:

$$H = A^TA + a^2\nabla^T\nabla \tag{3.28}$$

Repeating the previous simulation, the QP solution is improved by selecting $a = 1$. Still, the algorithm fails to properly optimize the solution for a sonoelastography simulation produced by a step function (i.e. inhomogeneous media). The main cause is the inadequate selection of weighted coefficient matrix A, which affects the average SWS between peaks of different tissue elasticity in-between; otherwise it is indifferent, as observed in the homogeneous medium.
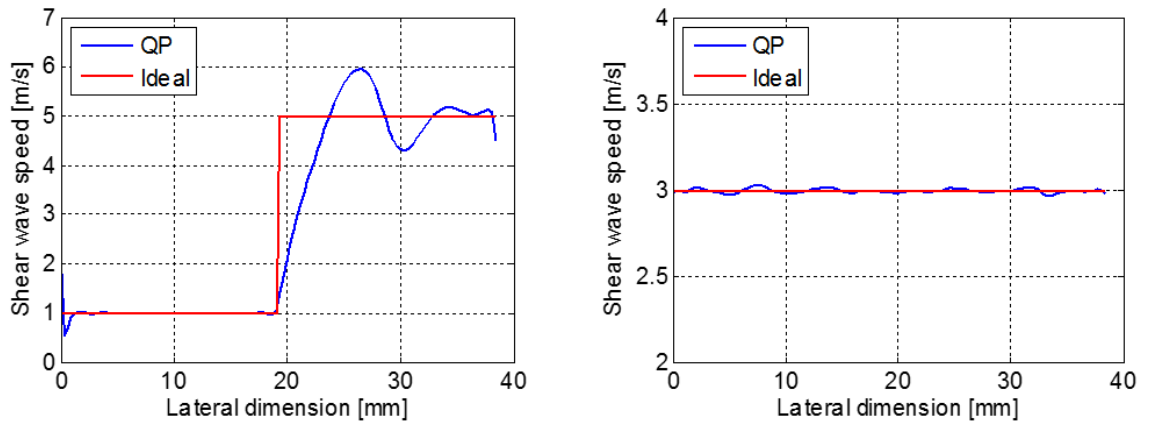
Figure 3.12: Regularized QP solution from simulated inhomogeneous (left) and homo-geneous media (right) generated from Table 3.4 using Equ. 2.15

3.2.4 Estimation of weighted coefficients

Initially, a theoretical estimation of the weighted coefficients was conducted for a two-phase medium (see Appendix 1). However, the simulations showed an underdamped response in the step function of elasticity, requiring a more accurate fitting. In order to solve A, several CrW simulations are conducted, each of them using a fixed x matrix and a measured S_{av} vector. The full procedure is described below:

1. A set of two-tissue medium vectors x, composed by regions A and B, is generated at random c_A and c_B SWS values.

2. Each medium is excited with a random frequency f_e to generate a CrW using Eqn.2.15, where a single equation is acquired from the peaks surrounding both tissue regions.

3. In order to construct a system of equations that features the same number of variables a, only those equations that meet a N number of variables are kept.

4. In a CrW segment that surrounds two different elasticity regions, let θ be the phase that delimits the boundary between these two regions. A high spatial frequency (low elasticity region) would contribute less than a low spatial frequency (high elasticity region) in the total width of the average wavelength and vice versa. This property affects the value of the a coefficients found in equations at different θ. However since the medium is already know, θ can be estimated for each equation and select only those that meet the condition $\theta = \theta_b$, where θ_b is a fixed given value.

5. To avoid the extensive computational time that takes to satisfy $\theta = \theta_b$, a range of tolerance is established as well: $\theta_b - \delta \leq \theta \leq \theta_b + \delta$.

6. Finally, after M equations are collected, the QP is used to solve A:
$$QP_A(xA = S_{av}) : min_A ||xA - S_{av}||^2 = \tfrac{1}{2} A^T H A - fA$$

Constrains

The difference between coefficients in the same elasticity region is smaller than the allowed difference between coefficient in different elasticity regions. Therefore an inequality restriction using a gradient operator is added to the QP optimizer.

$$|a_n - a_{n-1}| \leq \begin{cases} \dfrac{1}{N(N-1)} & \text{if } a_n, a_{n-1} \in \text{medium A or B} \\ \dfrac{(N-1)^2-1}{N(N-1)}, & \text{otherwise} \end{cases} \tag{3.29}$$

An equation restriction is also added due to the property of weighted sum:

$$\sum_{n=0}^{N-1} a_n = 1 \tag{3.30}$$

Since the coefficients are related to the elasticity values, they must be positive and different than 0:

$$a_n > 0 \tag{3.31}$$

Varying θ_b

A first set of simulations was conducted while varying θ_b from $0.15(2\pi)$ to $0.85(2\pi)$ in $0.01(2\pi)$ steps. Each simulation computed $M = 100$ equations of $N = 36$ variables each, with $\delta = 0.02(2\pi)$ and the same number of variables for each region ($N_A = 18$, $N_B = 18$). Results from a single simulation (i.e $\theta_b = 0.7(2\pi)$) are presented in Fig.3.13. Then, a linear fit was computed for the mean value of the weighted coefficients of each region A and B (separately) versus the vector θ as showed in Fig.3.14.
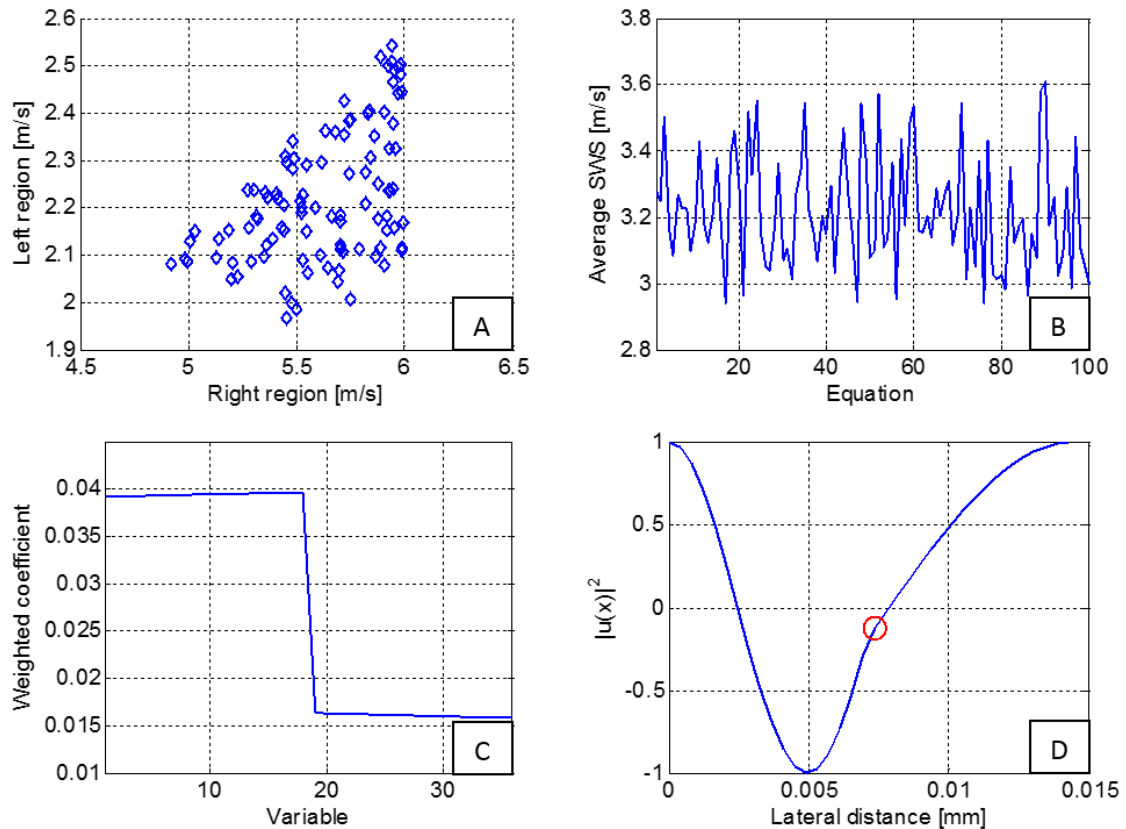
Figure 3.13: QP simulation for determine the weighted coefficients in an inhomogeneous medium.(A) Set of pair elasticity values for each equation.(B) Average SWS for each equation.(C) Calculated weighted coefficient.(D) Simulated Sonoelasticity signal where one equation was generated, showing the boundary phase $\theta = 0.7(2\pi)$ between medium.

From Fig.3.14, the linear fits showed that the average weighted coefficient is directly proportional to $\theta/2\pi$ and $1 - \theta/2\pi$ in region A and B, respectively. Both of those fits showed a proportional coefficient of $a = 0.055845$, approximately, which is very similar to the inverse of the number of elements for each region ($N_A = N_B = 18$). Since the simulations results suggested that average weighted coefficient was inversely
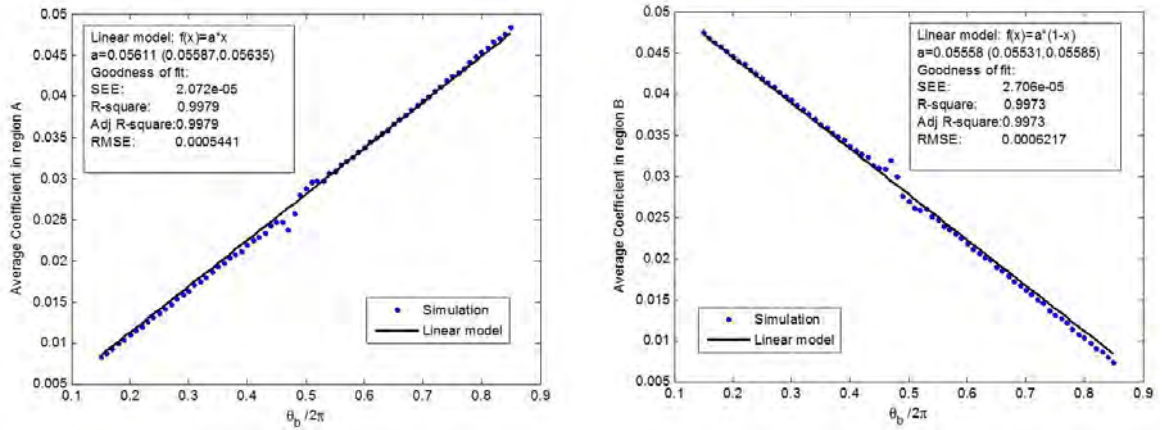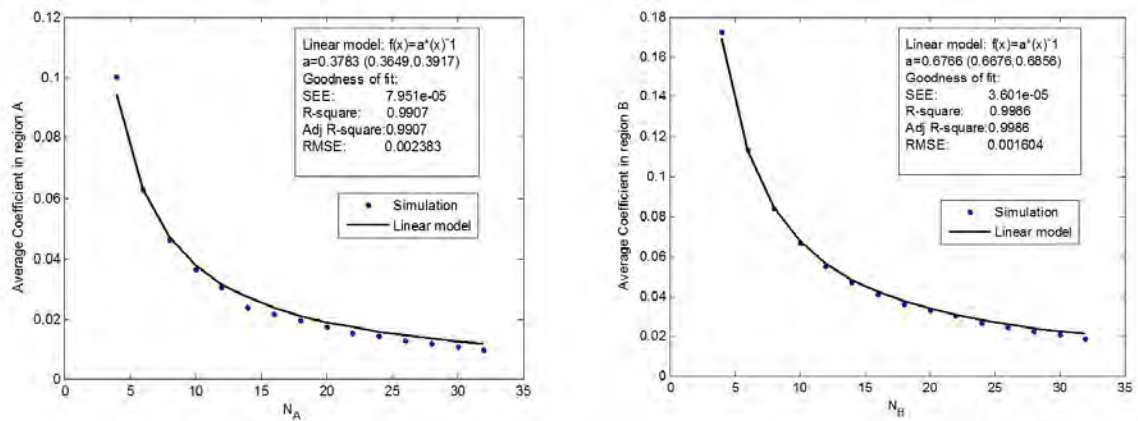
Figure 3.14: Linear fit for the mean solution of the a coefficients in region A (left) and region B (right) while varying θ

proportional to the number of elements of each region, an additional set of simulations was conducted for validation.

Varying N_A and N_B

A second set of simulations was conducted while varying the number of elements of each region in a fixed number of variables $N = 36$. This was accomplished by initializing the elasticity medium with a shifted boundary between region A and B, and then iterating new mediums with a shift vector. Each simulation computed $M = 100$ equation with $\theta_b = 0.35(2\pi)$ and $\delta = 0.02(2\pi)$. The results are presented in Fig.3.15. Here, the linear model of $f(x) = a(x)^-1$ closely follows the average coefficient with by a factor of $a = 0.3783$ and $a = 0.6766$ in region A and B, which is also similar to $\theta_b/(2\pi) = 0.35$ and $(1 - \theta_b/(2\pi)) = 0.65$, respectively.

From the analysis of the two set of simulations, the weighted coefficient can be estimated with the following empirical fit:

$$a = [a_0, ..., a_b, a_{b+1}, ..., a_{N-1}] \qquad a_i = \begin{cases} \dfrac{\theta_{\pi b}}{2}, & \text{if } i \le b \\ \dfrac{2\pi - \theta}{2\pi(N - b)}, & \text{otherwise} \end{cases} \tag{3.32}$$

where b is the boundary index that divide the regions. It is deduced that this algorithm takes an additional assumption since the interference pattern can contain no more than two different elasticity regions between its peaks. In order to achieve this condition, a higher vibration frequency may be needed to shorten the CrW's wavelength. For the estimation of θ, the Hilbert transform is performed in each of the wavelength segments

Figure 3.15: Linear fit for the mean solution of the a coefficients in region A (left) and region B (right) while varying N_A and N_B

(see Fig. 3.13.D). Then, the inflection point of the phase function is detected, a peak detector finds the highest value of the second derivate from the calculated phase vector, obtaining the boundary phase θ and the index b.
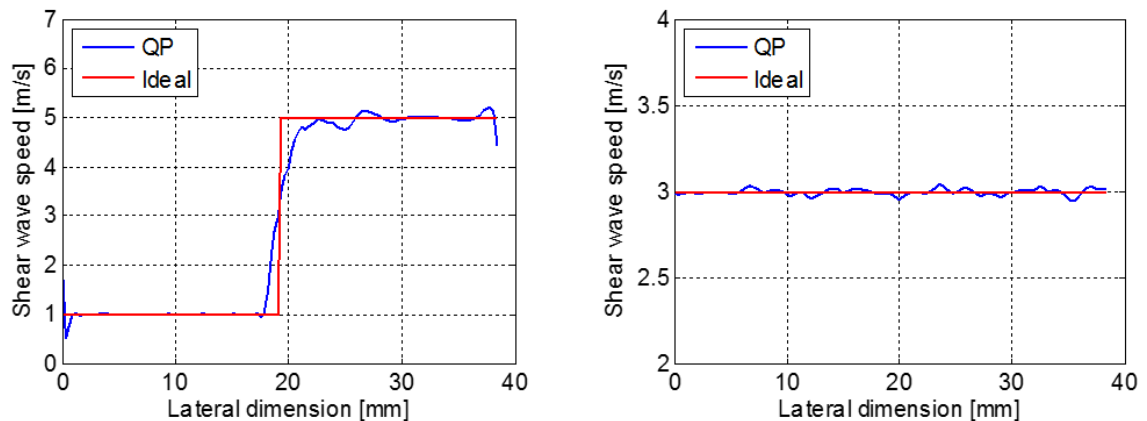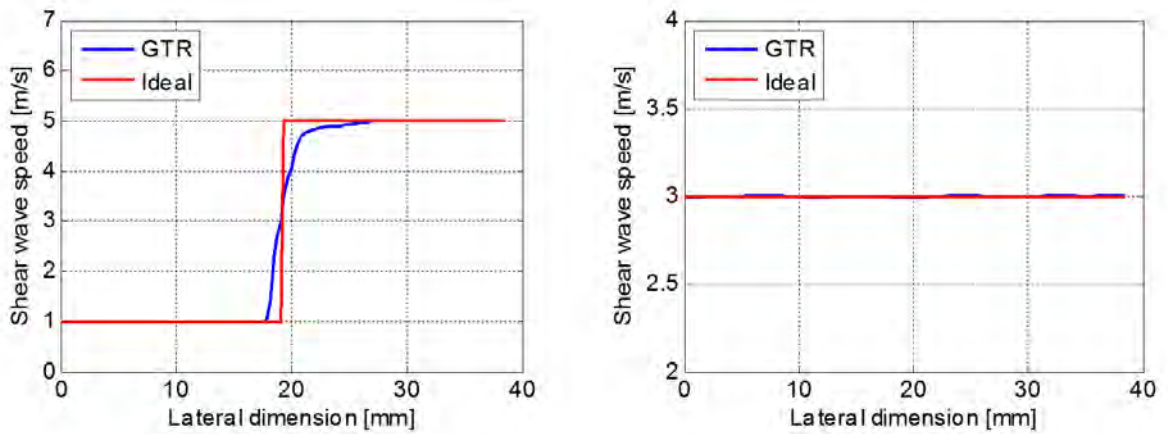

Figure 3.16: Regularized QP solution with modified coefficient matrix A from simulated inhomogeneous (left) and homogeneous media (right) generated from Table 3.4 using Equ. 2.15

The experiment showed in Fig. 3.6 is repeated one more time with the addition of weighted coefficient estimation process. As expected, the final results (see Fig. 3.16) depicted an improvement on the step function (inhomogeneous media) with a regularization parameter $a = 1$ while maintaining the performance in the constant function (homogeneous). Therefore, the regularized QP method is a viable option for solving $Ax_j = S_{av}$, where the weighted coefficient map A is estimated with the boundary phase

and index between different tissues.

3.2.5 Generalized Iterative Tikhonov Regularization

This method uses an expanded regularization term in the norm-2 least square minimization. The function to minimize is defined as:

$$\hat{x}_j = argmin[||Ax_j - S_{av}||^2 + a^2 \sum_{i=1}^{N} (|(\Gamma x_j)_i|^2 + \beta)^{\frac{k}{2}}] \tag{3.33}$$

Based on Lavarello *et al.* framework [LKO06], a generalized form of the Tikhonov regularization method presents an explicit solution of x_j:

$$x_j^{(n+1)} = [(A^T A + a^2 \Gamma^T W(x_j^{(n)})\Gamma)^{-1} A^T] S_{av} \tag{3.34}$$

Likewise, Γ is defined as the Tikhonov matrix equals to a gradient operator (∇), a is known as the regularization parameter and:

$$W(x_j^{(n)}) = \frac{k}{2} diag[(|\Gamma x^{(n)}|^2 + \beta)^{1-k/2}]_i. \tag{3.35}$$

While increasing a enhance robustness of A by reducing its condition number, it negative influence the spatial resolution. The stopping criteria of the iterative solution is defined by. The stopping criteria of the iterative solution is defined by:

$$\delta > \frac{||x_j^{(n+1)} - x_j^{(n)}||^2_2}{||x_j^{(n+1)}||^2_2}, \tag{3.36}$$

where δ is the regularization tolerance. Although repeating the simulation with GTR at $a = 1$ improved estimation results (see Fig.3.17), sensibility of the regularization coefficient in GTR is higher than the previous approach (i.e. for $a = 4$, comparable results were found using the regularized QP). However, GTR was chosen as the optimizer for the solution of x due to the continuity of each x_j along the lateral dimension without additional constrains and to the full control of the implemented algorithm (QP was used as a build-in Matlab function). Finally, the solution procedure for x_j is repeated for every depth j until the full shear wave speed image is reconstructed.

Figure 3.17: Generalized Tikhonov Regularization solution with modified coefficient matrix *A* from simulated inhomogeneous (left) and homogeneous media (right) generated from Table 3.4 using Equ. 2.15

3.3 Simulation and validation setup

In order to assess the performance of the proposed SWS estimator, crawling wave simulation on elasticity tissue as well as experiments on tissue mimicking phantoms were conducted with two SWS estimators found in the literature: the Phase Derivative (PD) estimator and the one-directional Hoyt estimator (1DH).

As described in chapter 2, the PD estimates the local spatial frequency k along each lateral profile of the crawling wave video. For each pixel, the phase of the interference patter is calculated by analyzing the peak frequency of the DFT along the slow time domain (i.e. $\Delta f / T_n$). Then, after unwrapping the signal along the lateral dimension, the lag-1 derivative of the phase is computed in order to obtain the spatial frequency k. Since k is inversely proportional to the final shear wave speed c_s, a small disturbance in continuity of the slope function would result in an amplified error in the reconstructed image, increasing the estimation variance. Therefore, a non-parametric regression (LOESS) process is often implemented before differentiating the phase function, smoothing the signal. The LOESS method takes as input parameter the size of the kernel w_l (i.e. 40% from the total number of samples of the input signal) that computes the regression for a single value along the phase function. While increasing the kernel size could benefit the reduction of the estimation variance, it compromise the lateral resolution as well as increase the presence of artifacts at boundary regions.

Likewise, the 1DH computes k directly by converting the lateral profile to an analytic signal (Hilbert transform) for later process it with a lag-1 autocorrelation function.

Similar to PD, 1DH controls the estimation accuracy of k by the size of the kernel (w_a) for autocorrelation. However, increasing this parameter reduce the width of the reconstructed image while increasing bias on the estimation.

3.3.1 Simulation setup

Simulations of heterogeneous and homogeneous media were performed for each of the proposed methods with the parameters described on Table.3.4, following the framework of Hoyt *et. al.* [HCP08]. Since all estimators compute the SWS along each lateral profile independently, only a single vector of elasticity value is required for the simulation. Additionally, the evaluation was repeated for several vibration frequencies, starting at 120 Hz to 500 Hz in 20 Hz step, as well as varying the smoothing parameter of each estimator at several set of two-phase mediums (see Table 3.5).

Table 3.5: Simulation Setup for performance evaluation

Parameter	Lower limit	Upper limit	Step	Units
Vibration frequency	120	500	20	Hz
Regularization coefficient (a)	0.3	1.6	20	-
LOESS kernel size (w_l)	5	70	1	% of total samples
Autocorrelation kernel size (w_a)	8	46	2	samples
Two-phase medium 1	1	5	-	m/s
Two-phase medium 2	2	4	-	m/s
Two-phase medium 3	1.5	1.5	-	m/s
Two-phase medium 4	3	3	-	m/s
Two-phase medium 5	4.5	4.5	-	m/s

3.3.2 Tissue Mimicking Phantom generation

Evaluation of both contributions (GPU implementation and SWS estimator) was conducted on tissue mimicking phantoms. The elaboration procedure follows the recipe

of Hah. *et. al* [HHM⁺12], specifying the inputs quantity as:

$$G[g] = \frac{x}{1-x} H[ml] \tag{3.37}$$

$$NaCl[g] = 0.009 H[ml] \tag{3.38}$$

$$A[g] = 0.0015 H[ml] \tag{3.39}$$

$$C[g] = 0.02 H[ml] \tag{3.40}$$

where H is deionized water, G dry gelatin (300 Bloom Pork Gelatin, Gelatin Innovations. Inc), $N\,aCl$ salt, A agar (Difco^{TM} Agar Technical, Becton, Dickinson and Company, Sparks, MD, USA) and C cornstarch. The dry gelatin and agar concentration controls the Young modulus of the tissue, while the salt and cornstarch controls the sound of speed and scatter concentration, respectively. The mixture was heated to 90 °C at 1200 RPM using a Robax§ M6 (Schott, Mainz, Germany) on a beaker. Then, after cooling it to 30 °C for approximately 10 min, the mixture was poured in a cubic container and allowed to rest at 4 °C overnight. For homogeneous medium, three phantoms of 12% (P1), 10% (P2) and 8% (P3) gelatin concentration were elaborated. Likewise, three heterogeneous phantom with a cylindrical inclusion were fabricated. A phantom with an inclusion of 7 mm diameter (P4) and 12% gelatin concentration simulated a small lesion in a background of 10% gelatin. Another phantom (P5) with the same concentration rates was generated but with a inclusion diameter of 12 mm. Finally, a 12 mm inclusion phantom (P6) was elaborated with 10% and 8% gelatin concentration for inclusion and background regions, respectively. Assessment of the true SWS vales was performed by several Time of Flight (ToF) acquisition. This procedure consisted of placing the mini-shakers at opposites sites of the phantom and generate an impulse signal from one of the mini-shaker that pass through the material and is received on the other one. Registered signals are then correlated in order to measure the delay shift between them (ToF), where the shear wave speed can be estimated by dividing the traveled distance and ToF. Several ToF experiments were conducted through all lateral sides of the phantom in order to avoid outliers measurements. In this study, the true SWS of the 12%, 10% and 8% concentration homogeneous phantoms were 4.95 ± 0.31 m/s, 4.08 ± 0.34 m/s and 3.43 ± 0.28 m/s, respectively. Table 3.6 summarizes the specifications of each elaborated phantom.

Table 3.6: Specifications of elaborated gelatin based phantoms

Index	Type	Inc. d (mm)	B.Conc (%)	I.Conc (%)	True SWS (m/s)
P1	Homogeneous	-	12	-	4.95 ± 0.31
P2	Homogeneous	-	10	-	4.08 ± 0.34
P3	Homogeneous	-	8	-	3.43 ± 0.28
P4	Heterogeneous	7	10	12	-
P5	Heterogeneous	12	10	12	-
P6	Heterogeneous	12	8	10	-

3.3.3 Acquisition setup

The conventional crawling wave setup was implemented on all gelatin phantoms, as described in section 2.3.1. Two mechanical mini-shakers (4810 Brüel & Kjaer, Naerum, Denmark) were placed at opposite lateral sides of the material (see Fig. 3.18). The excitation signals, with sinusoidal form and differentiated by 0.4 Hz, were generated with a dual channel function generator (AFG3022B, Tektronix, Beaverton, OR, USA) and an amplifier (5530, AE Techron, Elkhart, IN, USA). For acquisition, color radio frequency (CRF) data was acquired using two ultrasound systems: a linear transducer M12L (GE Healthcare, Wauwatosa, WI, USA) connected to a GE LOGIQ 9 (GE Healthcare, Wauwatosa, WI, USA), and a linear transducer L14-5/38 (Ultrasonix, British Columbia, Canada) connected to a SonixTouch (Ultrasonix, British Columbia, Canada). The last one was used for testing the GUI of the PD estimator, implemented with GPU acceleration. The pitch of the M12L and L14-5/38 were 4.08 mm and 3.08 mm, respectively.

3.3.4 Quantitative measurements

The quality of the reconstructed SWS images was compared using conventional metrics found in the literature.

Signal-to-noise ratio

The Signal-to-noise ratio (SNR) of a specific evaluation region was used to assess the homogeneity of the SWS estimates and was defined as [LBHY04]:

$$\text{SNR} = 20 \log_{10}(\mu_R / \sigma_R) \tag{3.41}$$
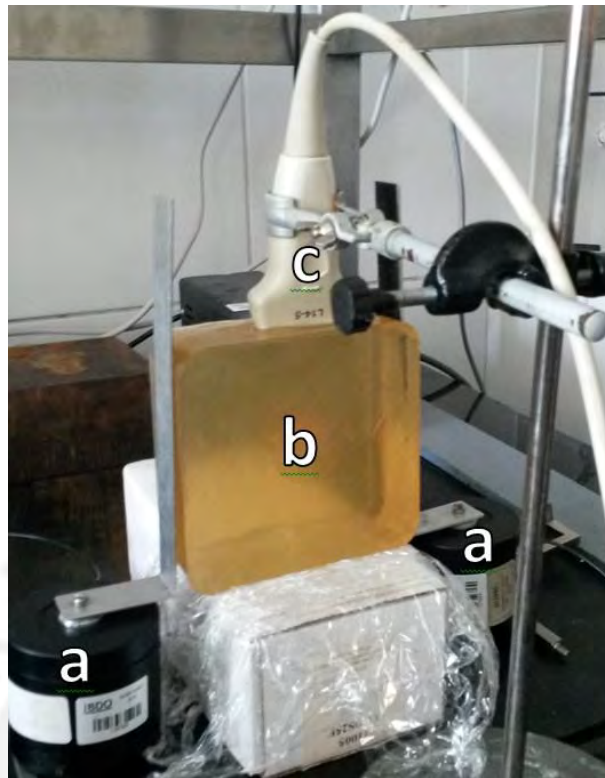
Figure 3.18: CWS using parallel excitation setup. (a) Mini-shakers. (b) Homogeneous gelatin-based phantom. (c) Ultrasound Transducer L14-5/38

where μ_R and σ_R were the mean and standard deviation of the calculated SWS of the region, respectively.

Contrast

Likewise, for heterogeneous media, Contrast (CR) was used and presented as:

$$CR = 20 log_{10}(\mu_I / \mu_B) \tag{3.42}$$

where μ_I and μ_B were the mean SWS values of the inclusion and the background, respectively.

Contrast-to-noise ratio

Additionally, the Contrast-to-noise ratio (CNR) assess the mean difference in two examined regions and the relationship towards their combined noise, which is expressed

by the following formula [LBHY04]:

$$\text{CNR} = 20\,log_{10}\frac{2(\mu_h - \mu_l)^2}{\sigma_h^2 + \sigma_l^2} \tag{3.43}$$

Spatial resolution

Spatial resolution (SR) of SWS images for heterogeneous phantom was calculated by fitting the lateral profile across the inclusion with a double sigmoid function [RWPN12], given by:

$$c(x) = (c_h - c_l)\left(\frac{1}{1 + e^{\frac{x_1-x}{\lambda_1}}}\right)\left(\frac{1}{1 + e^{\frac{x-x_2}{\lambda_2}}}\right) + c_l \tag{3.44}$$

where c_h and c_l are the SWS of inclusion and background, x_1 and x_2 are the edge location indexes, and λ_1 and λ_2 represents the transition width at the lateral sides of the inclusion, respectively. Then, the spatial resolution SR_{2080} (simplified as SR), is defined as the average of the λ distances for a 20% to 80% transition of the SWS, therefore [RWPN12]:

$$\text{SR} = ln(4)(\lambda_1 + \lambda_2). \tag{3.45}$$

This fitting process was repeated for 20 lateral profiles across a user-defined region of evaluation, where the final SR was obtained from the median value of the SR vector.

Bias and Coefficient of variation

Estimation accuracy can also be defined relative to the true value of the SWS estimates. The bias of an estimations indicates how far the calculated mean differs from the true mean value, expressed as:

$$\text{Bias} = 100(|(\mu_c - \mu_i)|/\mu_i). \tag{3.46}$$

where μ_c and μ_i are the calculated mean and ideal mean of the estimates, respectively. Similarly, the coefficient of variation (CV) takes into consideration the standard deviation relative to the true mean value and is defined as:

$$\text{CV} = 100(\sigma/\mu_i). \tag{3.47}$$

4 Experiments and Results

4.1 GUI: Evaluation of Crawling Wave Quality vs IQ filter order

Typically, after the low pass filter in the IQ process is performed, analytic data is decimated by a factor proportional to the ratio between the signal bandwidth and sample frequency, both being constant parameters in the present study. For instance, in the Matlab environment decimation is computed with an 8th order Chebyshev IIR filter enhancing stop-band response and noise suppression. With only a 2nd order FIR filter, sonoelastography images generated with the Miller's algorithm present poorly defined interference patterns (CNR: -44dB), which translates into increased phase error and high SWS standard deviation (0.76 m/s). Therefore, acquired CRF data from an homogeneous phantom (P2) was processed with several FIR filters to determine the optimal filter order that balance CNR, SWS STD and excecution time. Fig. 4.1 depicts interference patterns at different FIR filter order, specifying regions for CNR assessment. Measured CNR as well as standard deviation of SWS, using the PD estimator, are presented in Fig. 4.2. From this results, a filter order of 6 was chosen since higher order filters didn't significantly improved neither the CNR (less than 0.5dB) nor further reduced the STD of the reconstructed SWS images.
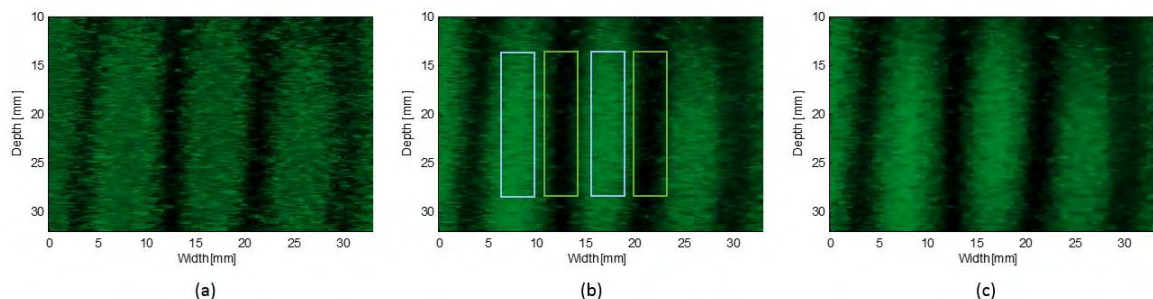
Figure 4.1: Interference pattern of homogeneous media (P1) using (a) 2nd order, (b) 3rd order and (c) 6th order low pass FIR filter in the IQ process.
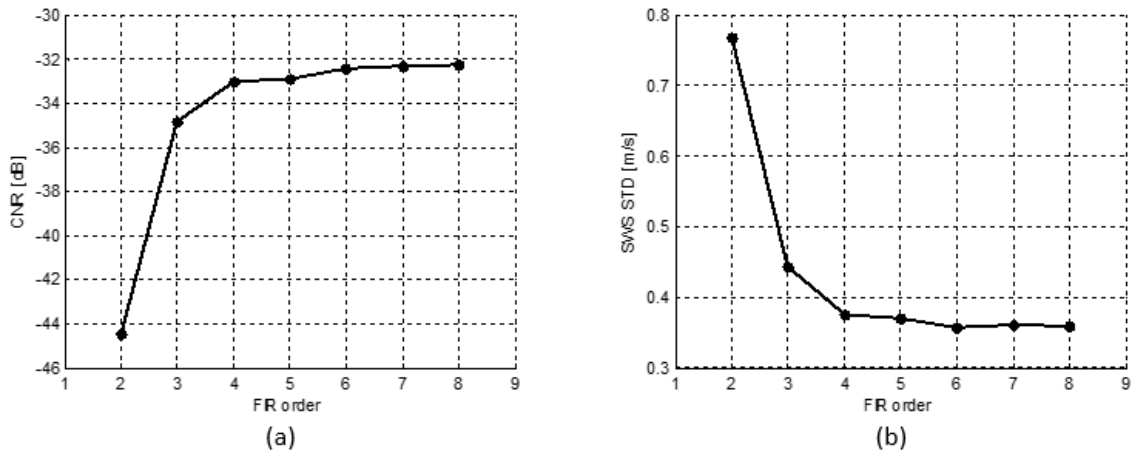
Figure 4.2: Low pass FIR filter performance in the IQ process while increasing the filter order. (a) Crawling Wave CNR from regions specified in Fig. 4.1. (b) STD of the reconstructed homogeneous SWS images.

4.2 GUI: SWS estimation on gelatin-based phantoms

Fig.4.3 shows the SWS images of an homogeneous phantom (P3) with 8% gelatin concentration (3.43 ± 0.28 m/s) with the mini-shakers operating at 200 Hz (200 Hz and 200.4 Hz) and 300 Hz (300 Hz and 300.4 Hz). It can be appreciated that both SWS images generated with the PD estimator exhibit lateral artifacts, as reported in the literature. However, accuracy of the algorithm is validated since the average SWS estimation at low (3.68 ± 0.17 m/s, SNR: 26.61 dB at 200 Hz) and high frequencies (3.78 ± 0.13 m/s, SNR: 29.19 dB at 300 Hz) are within 7% of the ground truth values obtained from mechanical measurements.

Similarly, Fig.4.4 shows the SWS images of an inclusion phantom (P5) with 10% gelatin concentration in background (4.08 ± 0.32 m/s) and 12% in the inclusion region (4.95 ± 0.31 m/s), excited with the same pair of vibration frequencies. Then, quantitative measures were calculated form evaluations regions of the background and inclusion (labeled in Fig.4.4) and are presented in Table 4.1. At 200 Hz, background and inclusion estimates were in good relation to the SWS ground truth values (B: 3.96 m/s and I: 5.18 m/s). Additionally, while increasing the vibration frequency slightly enhanced the CNR, CR and SNR, a trade off was observed due to the SR degradation as wells as overestimation of both inclusion and background regions. Still, the GUI implementation successfully differentiated heterogeneous media with low estimation variance on the SWS values (STD <0.28 m/s).
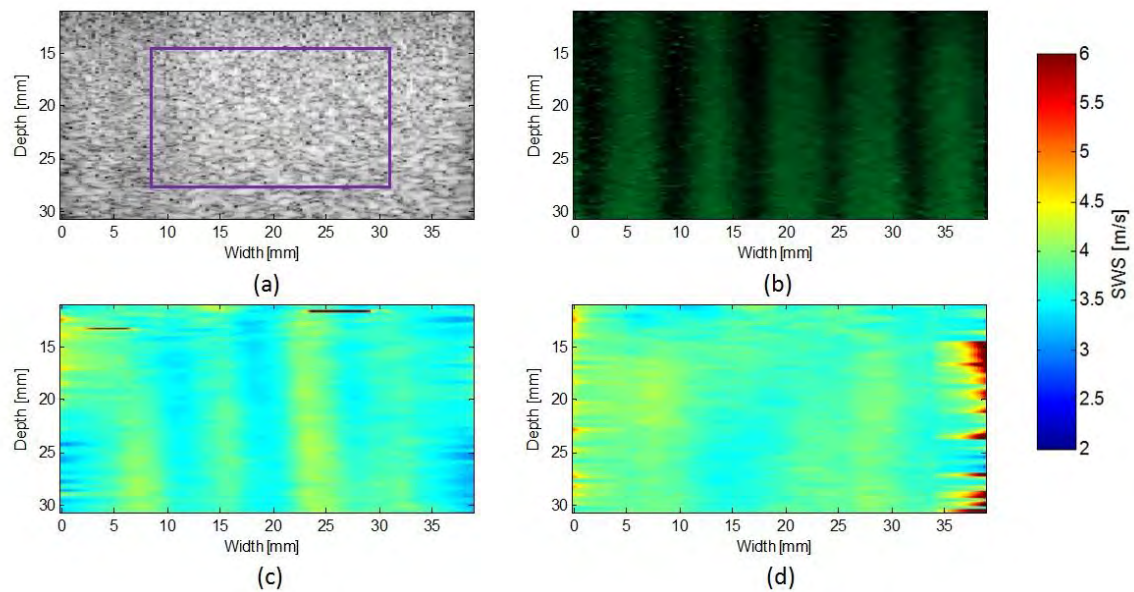
Figure 4.3: SWS results of an homogeneous phantom (P3). (a) B-mode image. (b) Crawling waves at 200 Hz. (c) SWS images at 200 Hz and (d) 300 Hz. Evaluation box is labeled in (a) and $w_l = 33$ was used for both cases.
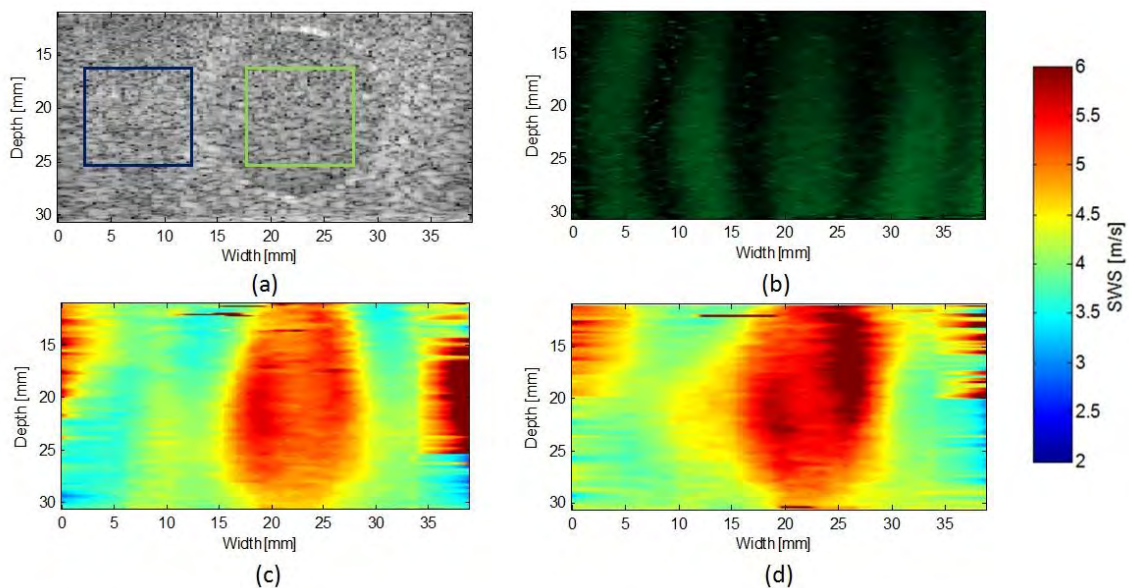
Figure 4.4: SWS results of an heterogeneous phantom (P5). (a) B-mode image. (b) Crawling waves at 200 Hz. (c) SWS images at 200 Hz and (d) 300 Hz. Evaluation boxes are labeled in (a) and $w_l = 33$ was used for both cases.

Table 4.1: Quantitative measurements of a 10 mm diameter inclusion phantom (P5)

Parameter	f = 300 Hz		f = 200 Hz		Unit
Mean	B: 4.213	I: 5.646	B: 3.958	I: 5.183	m/s
STD	B: 0.187	I: 0.275	B: 0.183	I: 0.145	m/s
SNR	B: 26.240	I: 31.386	B: 31.067	I: 34.828	dB
CNR	27.048		26.707		dB
CR	2.544		2.342		dB
SR	4.822		1.802		mm

4.2.1 Adjusting the LOESS kernel size

Estimation of SWS in the small-lesion phantom (P4) was conducted while varying the LOESS kernel size (w_l) and results are presented in Fig. 4.5. As mentioned in Chapter 2, increasing w_l benefits the smoothing of the phase function θ and thus, increase the signal rejection from the noise in the SWS image, which is appreciated as enhanced CNR and SNR following a linear progression in Fig.4.6. However, increasing this parameter also compromises spatial resolution (see Fig.4.6.e) as well as generates artifacts at the boundaries of the SWS images. Furthermore, the processing time consumed in the PD estimator stage was also increased (see Fig.4.7.), which compromises the feasibility of CWS in real-time. While a delay of 123.50 $\pm$ 1.46 ms was reached at w_l = 33 with the maximum examination window size, real-time imaging was still accomplished below this threshold at 2 Frames Per Second (FPS). Here, evaluation regions were previously filtered by keeping the 95 percentile of the SWS values in the evaluation region, avoiding outliers of several order of magnitudes (i.e 1.3E5 m/s) that might severely affect mean and STD estimations.
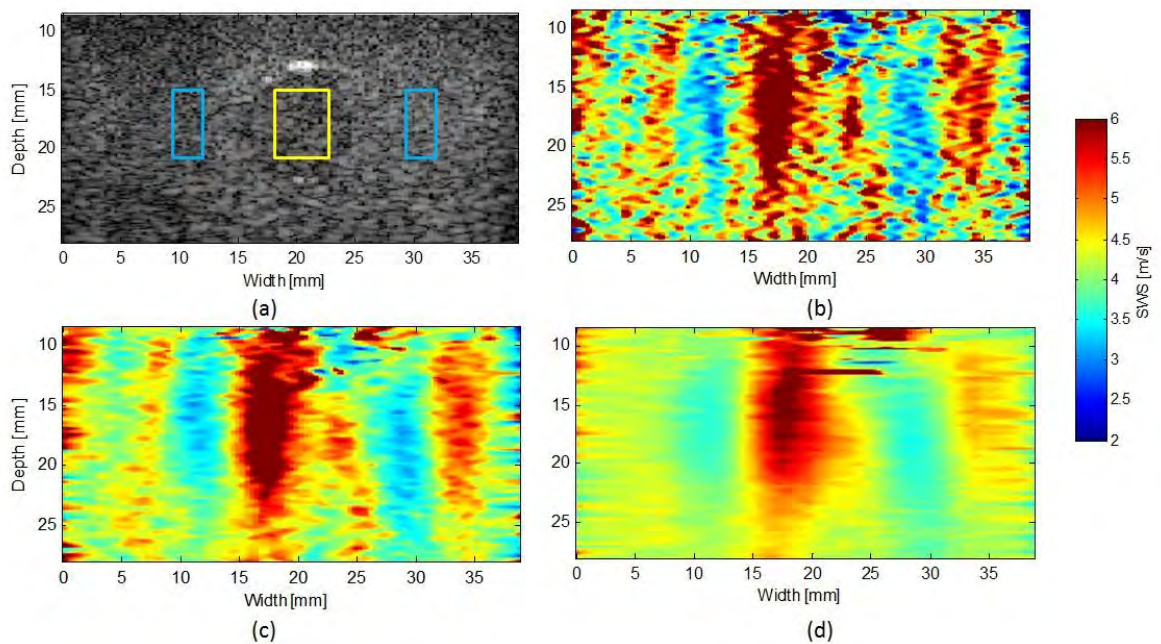
Figure 4.5: SWS images of a 7 mm diameter inclusion phantom (P4) varying w_l. (a) B-mode image at 50 dB dynamic range. SWS images are displayed with (b) 7, (c) 15 and (d) 33 samples of w_l. Blue and yellow labeled regions were set for quantitative measurements of inclusion and background, respectively
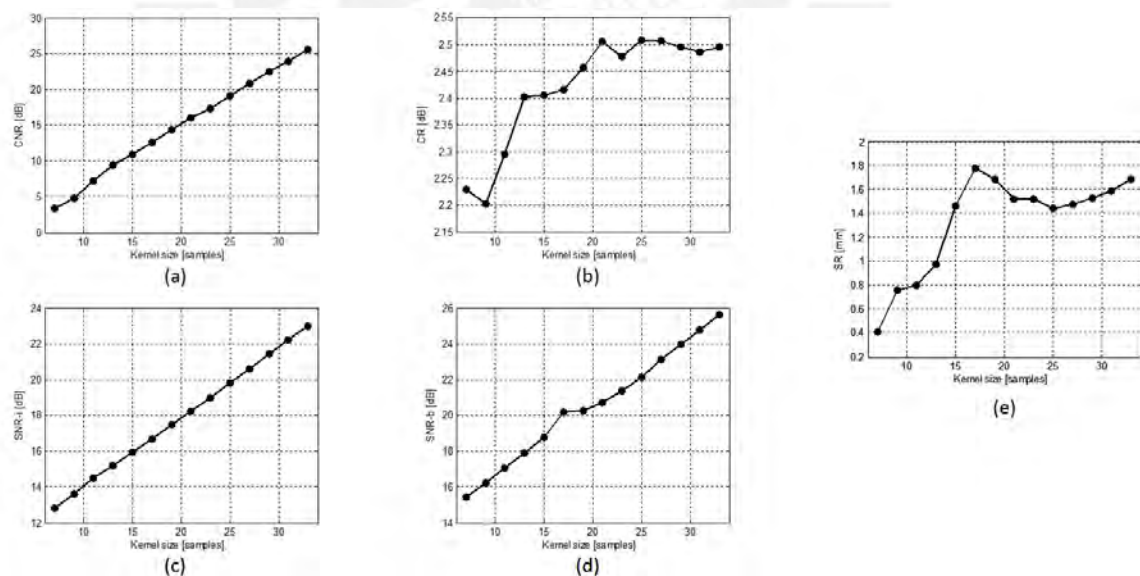
Figure 4.6: Quantitative measures vs LOESS kernel size w_l
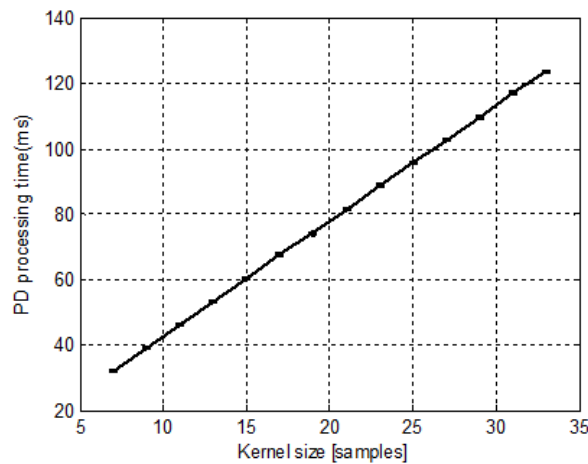
Figure 4.7: Processing time consumed on the PD estimator stage with different w_l
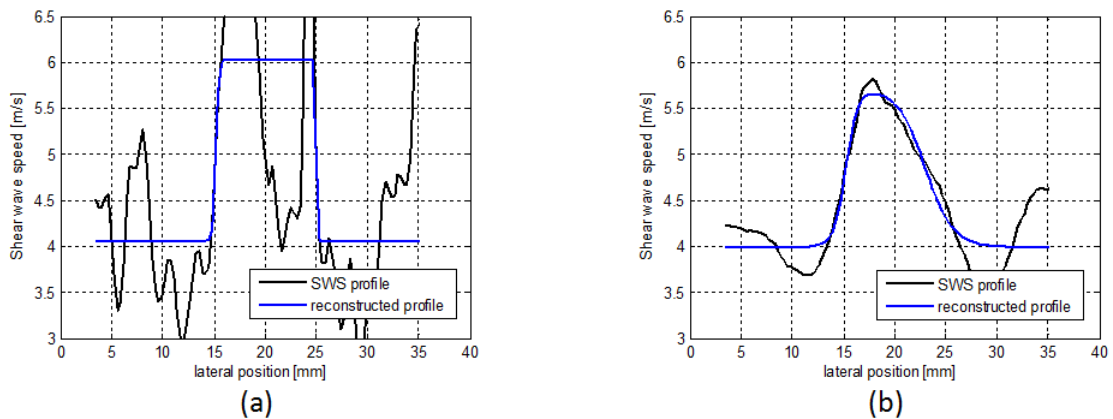
Figure 4.8: Curve fitting for estimation of lateral resolution using (a) $w_l = 7$ and (b) $w_l = 33$ samples in a small lesion phantom (P4)

4.2.2 Comparison with MATLAB implementation

In order to achieve a frame rate suitable for real-time imaging, the CWS algorithm was adapted for parallel computing while optimizing the transfer memory between the host and the device (GPU). This last feature was accomplished by processing each stage of the algorithm with simplified variable types, such as int-16, float and short, consuming less memory. Since subsequent truncations of processed data often lead to inaccurate results, SWS estimates obtained from the GUI were compared with the ones obtained from a MATLAB implementation (offline mode), considering as input data for the latter the CRF signals acquired from the GUI. Fig.4.9 shows the SWS estimation of an heterogeneous phantom (P5) calculated from each implementation. Initially, by

setting the same LOESS kernel (i.e. $w_l = 33$ samples), image quality of the MATLAB environment appeared as inferior in comparison with the GUI image. For instance, subtracting one SWS image from the other and removing the 5 and 95 percentile of the difference resulted in 0.4632 ± 0.1938 m/s. However, when w_l was increased in the MATLAB algorithm (i.e. $w_l = 51$), SWS values were found to be quite similar (0.0888 $\pm$ 0.0724 m/s). This results could suggest that the order of the programmed local regression filter was higher than the in-build *smooth* function used in the MATLAB environment. Nevertheless, as observed in Fig.4.9, both of them successfully detects the inclusion with well-defined edges.
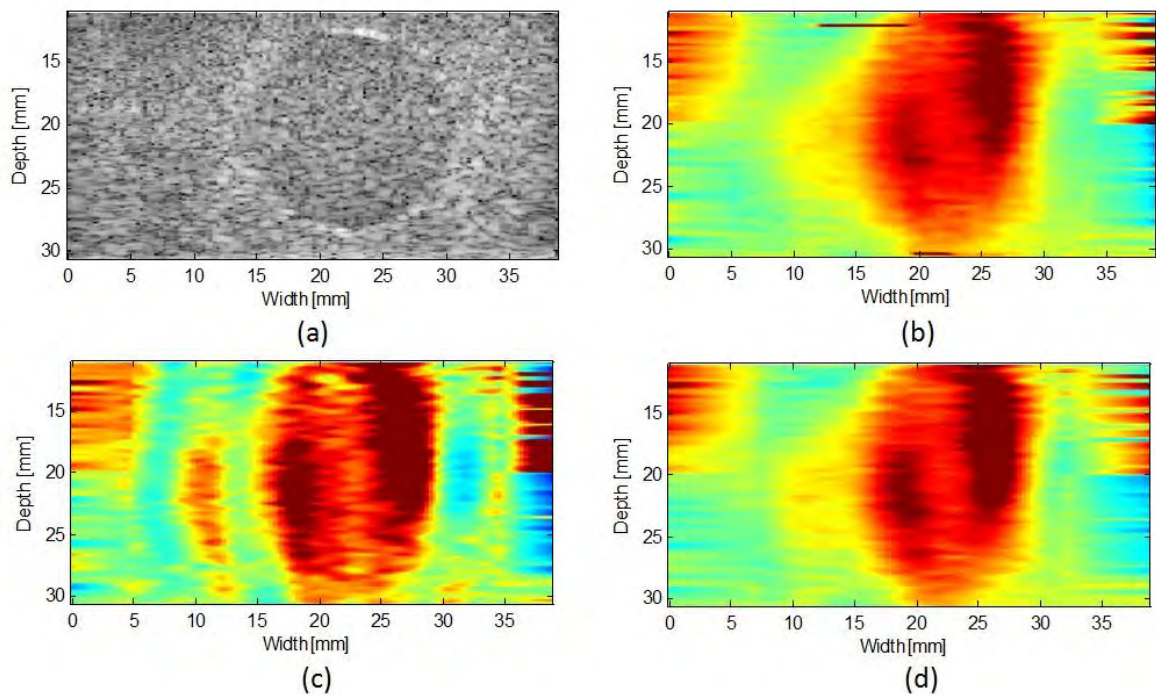
Figure 4.9: Comparison of CWS implementation in the GUI and MATLAB enviroment. (a) B-mode image. (b) SWS image from GUI at $w_l = 33$. (c) SWS image from MATLAB at $w_l = 33$ and (d) $w_l = 51$

4.3 GUI: Processing time performance

Synchronization of data acquisition and computing time for real-time feasibility highly depended on the color box size (ROI) and the raw data frame rate. The first parameter affected the total amount of data to process in the GPU while the other one was controlled by the ensemble package, Pulse Repetition Frequency (PRF) and imaging

depth of the ROI. In the architecture of parallel computing, if the number of samples in a vector is higher than the number of threads found in the device, kernel are executed piece-wise and multiple times, significantly lowering the processing frame rate. Therefore, a maximum ROI of 19.64 x 38.7 mm was set in order to avoid this condition. Likewise, the CRF frame rate provided by the SonixTouch automatically varied when imaging at different depths, changing the ensemble package and/or PRF. For instance, synchronization was not achieved with the current ROI in depths near the phantom surface (i.e. <5mm), ensemble package smaller than 10 or PRF higher than 1.3 KHz. Hence, a fixed frame rate of 2 Hz was established for CRF data acquisition, lowering the transfer speed of the host to the GPU and thus, allowing the processing frame rate to match with the raw data frame rate. The execution time of each process of the quantitative sonoelastography algorithm implemented in the GPU was measured with the CUDAEventRecord function, located in the CUDA runtime library. In order to compare the performance with a typical computer implementation, each function was serialized and programmed in the host computer as well, measuring the execution time using the time.h library. Then, the speedup of an algorithm is presented as the ratio of execution times in the GPU and CPU:

$$\text{Speedup}(f) = \frac{T_{CPU}(f)}{T_{ttPU}(f)} \tag{4.1}$$

Specifications of the acquired data for performance evaluation is described in Table 4.2. The complete method was divided in 8 processes: Radio frequency signals to in-phase quadrature data (IQ, <short>), analytic data to spectral frequency variation data (Sono,<int16>), processing the sonoelastography data with a [3x3] median filter (Sono-M <int16>), normalization and DC filtering of the sonoelastography data (Sono-F <float>), reordering the sonoelastography video according to the last acquired frame index (Reorder, <float>), computing the Fast Fourier Transform along the temporal dimension (FFT, <float>), phase derivative estimator and color indexing (PD, <float>) and post-processing the reconstructed image with a [3x3] median filter (SWS-M, <unsigned char>). Then, Fig. 4.10 shows the comparison of execution time for GPU and CPU, while Table 4.3 presents the detailed evaluation results for each algorithm. Measurements of execution time for both GPU and CPU processes were repeated for 10 set of data, enhancing precision and reducing outliers generated from cache memory access. For the FFT function, evaluation was conducted using well-know libraries for GPU (cuFFT) and CPU (FFTW).

Table 4.2: Parameters of the acquired data for performance evaluation

Parameter	Symbol	Value	Unit
Scan lines	x	128	samples
Ensemble package	e	14	samples
Axial samples	z	1020	samples
Acquired frames	p	50	-
Local regression kernel	k_l	9	samples
Depth offset	Z_0	11	mm
Lateral pixels	w	230	pixels
Axial pixels	h	169	pixels
Pulse Repetition Frequency	PRF	600	Hz
Frame rate	FR	2	Hz
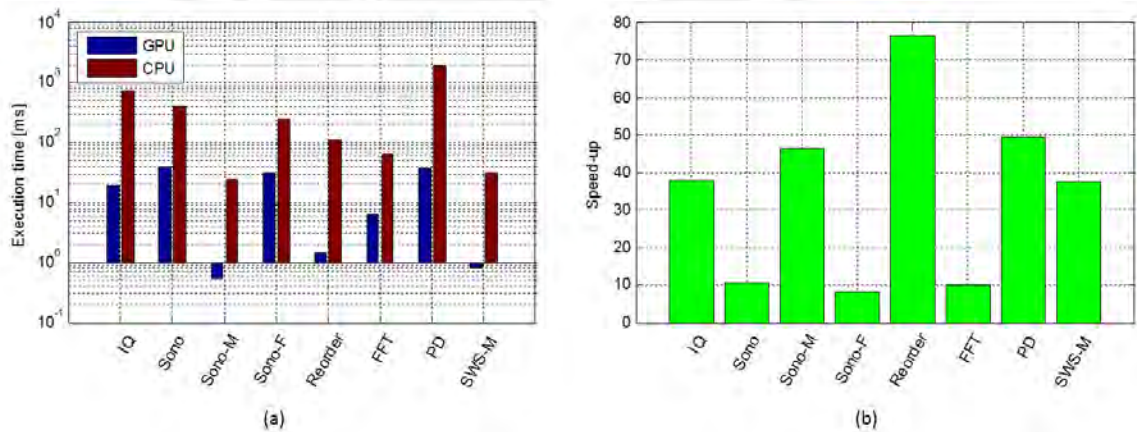
Figure 4.10: Performance of each process of the quantitative sonoelastography algorithm. (a) Execution time on GPU and CPU, (b) Speedup.

Table 4.3: Execution time of the quantitative sonoelastography processes

Process	$T_{ttPU}(ms)$			$T_{CPU}(ms)$			Speed-up		
IQ	19.47	$\pm$	0.07	738.62	$\pm$	0.80	37.93	$\pm$	0.13
Sono	39.47	$\pm$	0.14	421.05	$\pm$	1.91	10.67	$\pm$	0.04
Sono-M	0.52	$\pm$	0.01	24.33	$\pm$	0.35	46.52	$\pm$	0.65
Sono-F	30.93	$\pm$	0.15	249.99	$\pm$	0.42	8.08	$\pm$	0.04
Reorder	1.42	$\pm$	0.01	109.29	$\pm$	0.49	76.71	$\pm$	0.74
FFT	6.30	$\pm$	0.01	62.55	$\pm$	0.59	9.92	$\pm$	0.09
PD	38.11	$\pm$	0.25	1874.86	$\pm$	1.53	49.21	$\pm$	0.33
SWS-M	0.82	$\pm$	0.01	30.96	$\pm$	0.33	37.59	$\pm$	0.35

4.4 R-WAVE: Crawling wave simulation

Estimation results of homogeneous and heterogeneous medium are presented in Fig.4.12, 4.13, 4.14 for all vibration frequencies. Spatial resolution on two-phase medium was calculated as the rising time of a fitted step response using an in-build MATLAB estimator. Regarding the estimation accuracy, the resulting SWS signal was splitted in two at the center value of the lateral vector, where the ideal boundary was located.
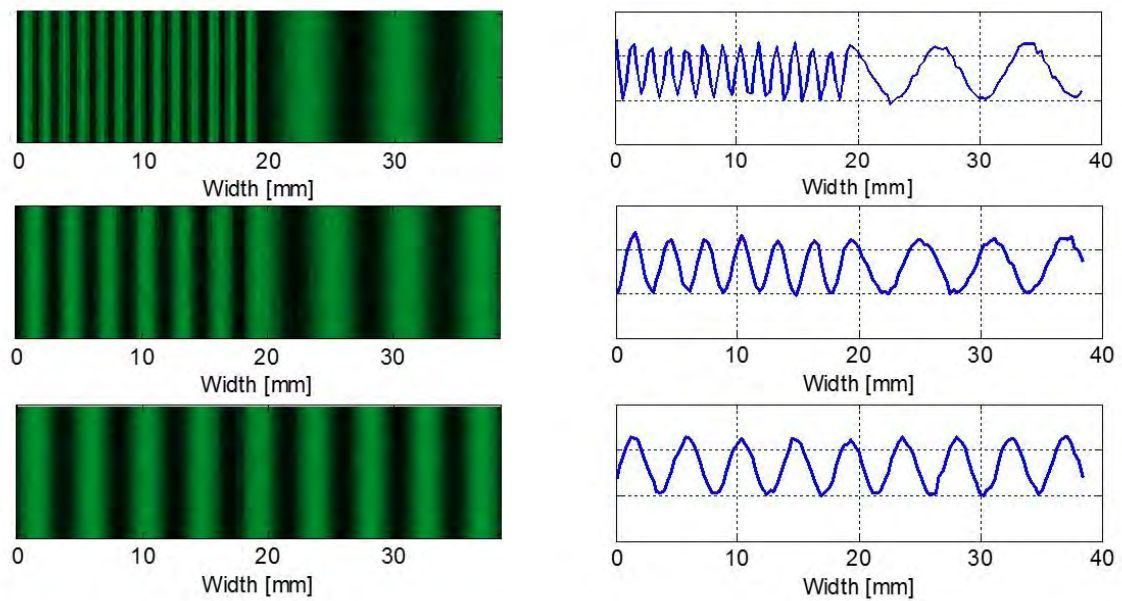
Figure 4.11: Crawling wave simulation in different media at 260 Hz vibration frequency. Left: Simulated sonoelasticity image. Right: Lateral profile for SWS estimation. Top: [1 5] m/s SWS media. Center: [2 4] m/s SWS media. Bottom: [3 3] m/s SWS media (homogeneous).

where h and t subindex stand for high and low SWS regions, respectively.

As observed in Fig. 4.12, R-WAVE outperformed the others estimators in homogeneous media at all frequencies, presenting the lowest bias (PD: 0.32%, 1DH: 2.12%, R-WAVE: 0.009%) and CV (PD: 2.10%, 1DH: 0.83%, R-WAVE: 0.19%). While PD showed comparable performance at 360 Hz or higher (4.503 $\pm$ 0.024 m/s), overestimation and increase of estimate variance was present at lower frequencies. Likewise, 1DH underestimated the homogeneous SWS at frequencies below 250 Hz (4.295 $\pm$ 0.072 m/s), improving it principally by increasing the autocorrelation kernel, since no significant change was appreciated at higher frequencies. In the first two-phase media (see Fig. 4.13), R-WAVE present enhanced CNR at frequencies higher than 250 Hz (PD: 36.95 dB, 1DH: 30.75 dB,R-WAVE: 41.68 dB) while keeping the lowest SR (PD:
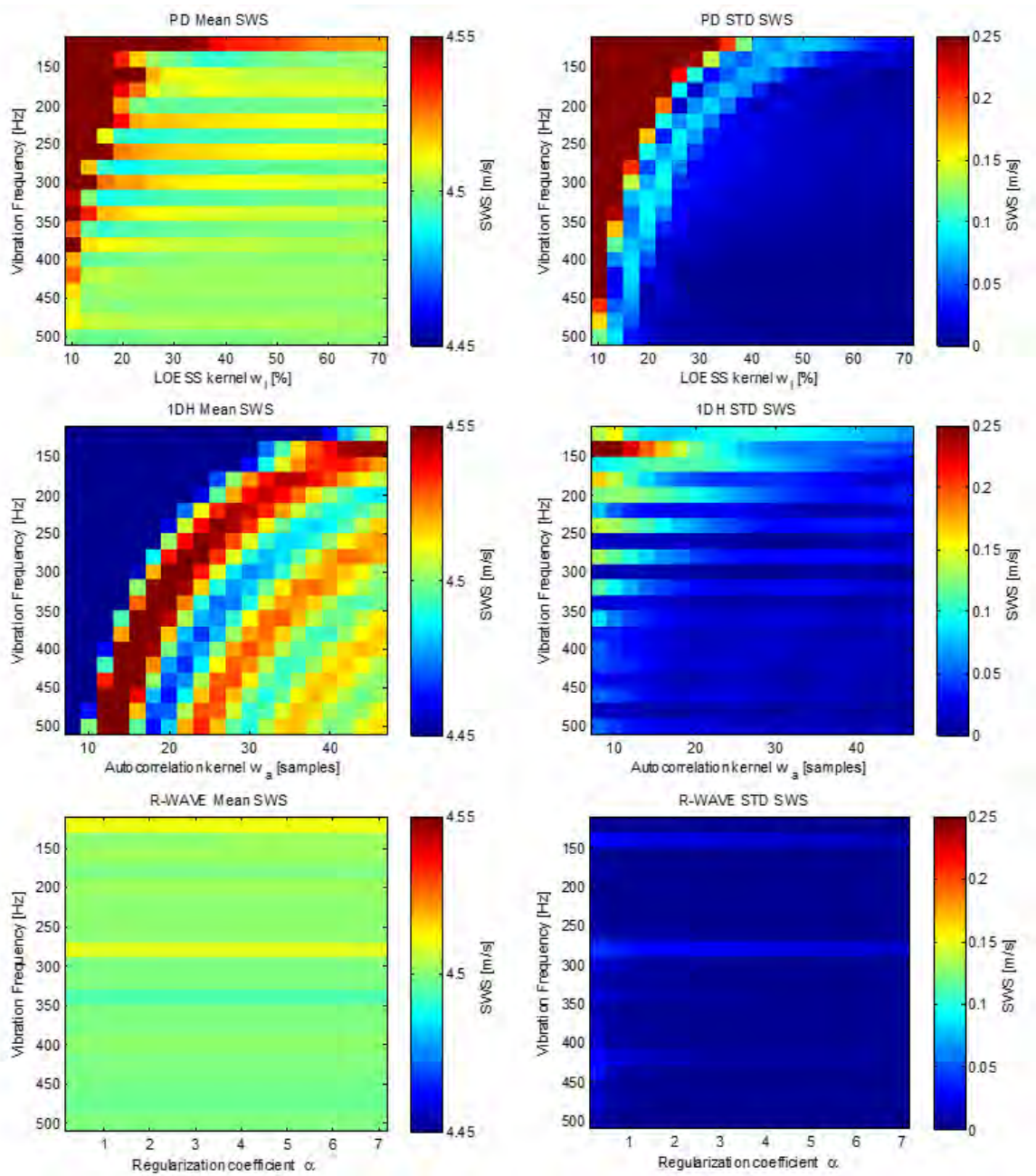
Figure 4.12: Mean and STD values of SWS estimation in homogeneous media of 4.5 m/s SWS. Top: PD. Center: 1DH. Bottom: R-WAVE

4.24 mm, 1DH: 6.32 mm, R-WAVE: 3.07 mm). Although increasing the smoothing parameters degraded CNR and SR on all estimators, R-WAVE was the least affected among the three. For instance, at 300 Hz, difference of CNR and SR using the lowest and highest smoothing parameter for each estimator was [7.08 mm; 11.12 dB], [7.11 mm; 16.17 dB] and [3.29 mm; 3.13 dB] for PD, 1DH and R-WAVE, respectively. In
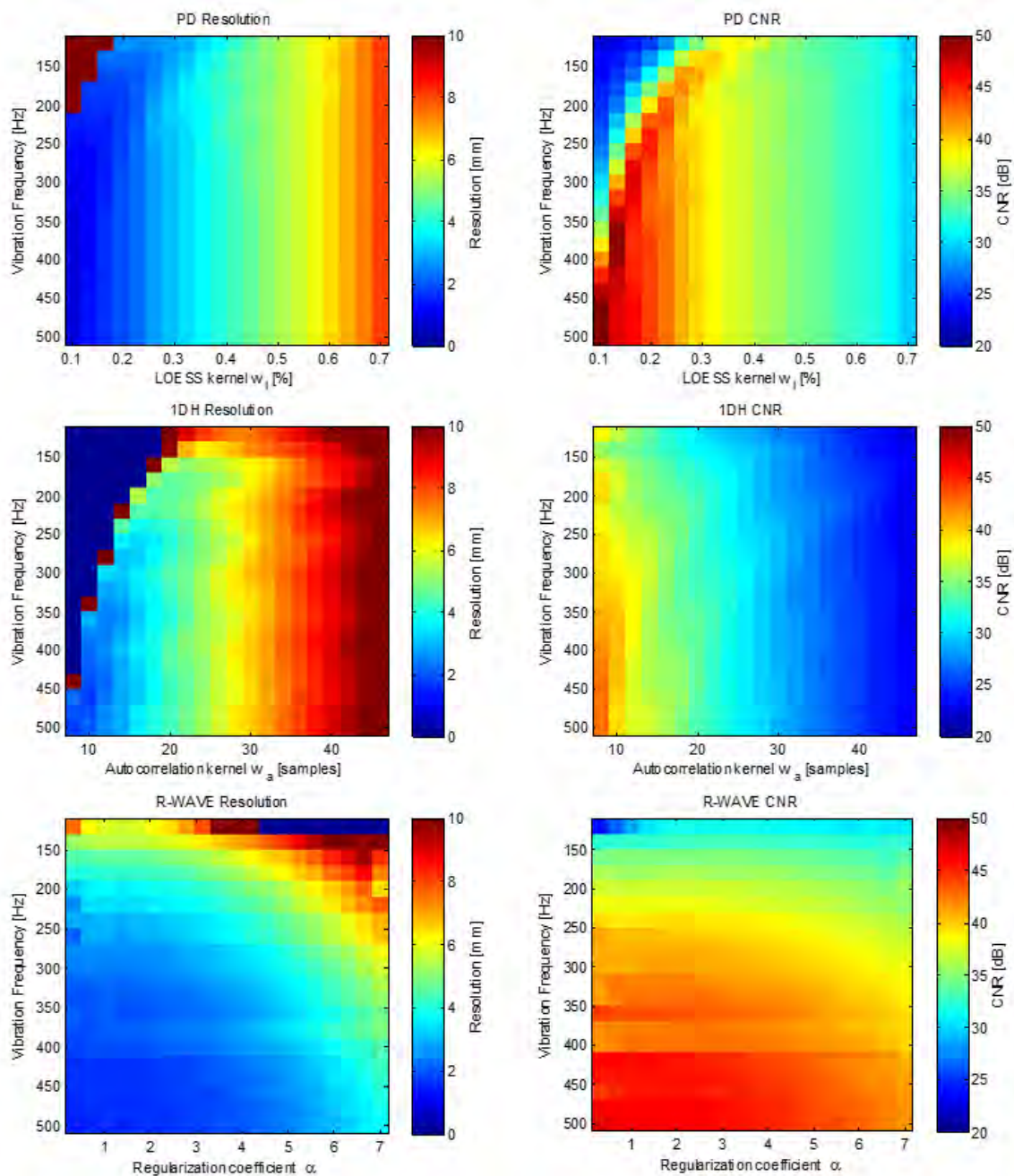
Figure 4.13: Spatial resolution and CNR of two-phase media with 2 m/s and 4 m/s SWS. Top: PD. Center: 1DH. Bottom: R-WAVE

comparison with PD and 1DH smoothing parameter's range, however, it is worth mentioning that the typical a used in experimental data range from 0.5 to 3. Hence, a regularization coefficient of 7 is unlikely to be used in practice. Similarly, comparison of estimation results in the second two-phase media (see Fig.4.14) benefit R-WAVE at frequencies higher than 180 Hz in CNR (PD: 30.19 dB, 1DH: 25.77 dB, R-WAVE:
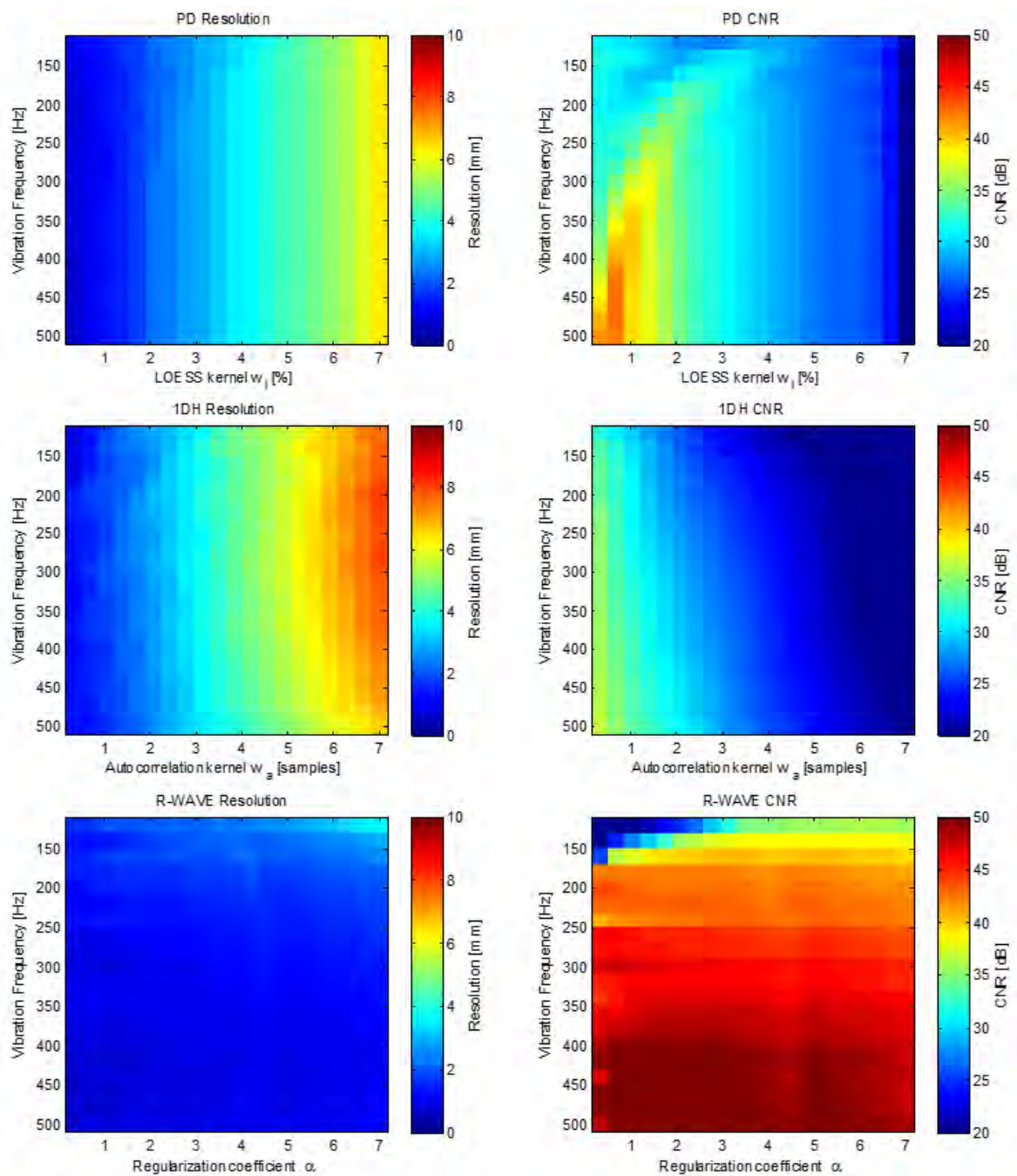
Figure 4.14: Spatial resolution and CNR of two-phase media with 1 m/s and 5 m/s SWS. Top: PD. Center: 1DH. Bottom: R-WAVE

46.53 dB) and SR (PD: 3.36 mm, 1DH: 4.33 mm, R-WAVE: 1.16 mm). For instance, at 300 Hz, variation of CNR and SR was [5.48 mm; 11.82 dB], [6.61 mm; 17.27 dB] and [0.44 mm; 1.92 dB] for PD, 1DH and R-WAVE, respectively.
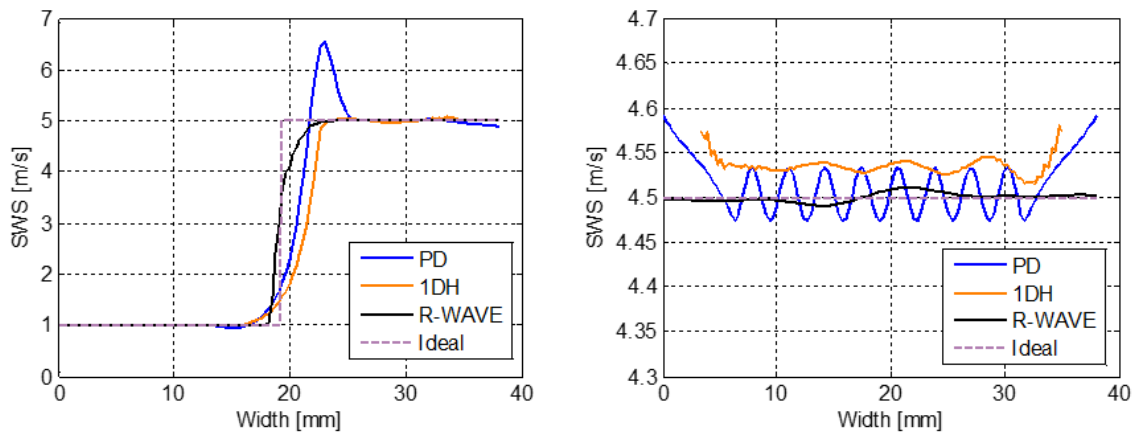
Figure 4.15: Estimated SWS profile of a heterogeneous (left) medium of [1 5] m/s SWS and homogeneous (right) medium of 4.5 m/s SWS. Results computed with f @ 260 Hz, PD @ 35.3% w_l, 1DH @ 22 w_a and R-WAVE @ 1.36 a.
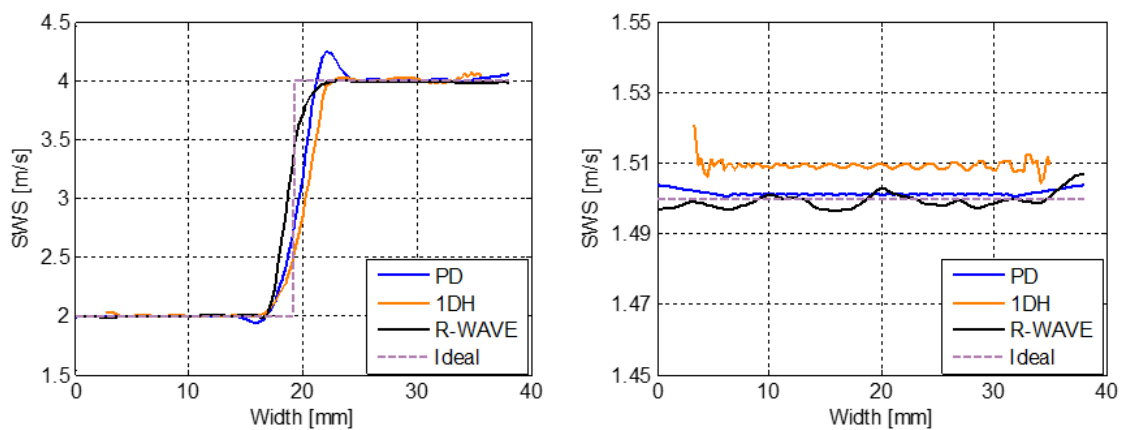
Figure 4.16: Estimated SWS profile of a heterogeneous (left) medium of [2 4] m/s SWS and homogeneous (right) medium of 1.5 m/s SWS. Results computed with f @ 260 Hz, PD @ 35.3% w_l, 1DH @ 22 w_a and R-WAVE @ 1.36 a.

4.5 R-WAVE: Experiments on elasticity phantoms

In this section, results on elaborated elasticity phantoms as well as calibrated tissue mimicking phantom are presented. For all experiments, CrW were processed with a fixed moving filter of [2 6] m/s elasticity range. Furthermore, each estimator computed the SWS images with a corresponding fixed smoothing parameter, which was calibrated from CrW data provided by the University of Rochester, USA. In an heterogeneous phantom of 3 m/s background and 5 m/s inclusion of 12 mm (P7), selection of the optimal parameter was conducted by minimizing the bias function of the mean SWS

from the inclusion region at 360 Hz vibration frequency. The calculated smoothing parameter were: $a = 1.2$, $w_l = 30\%$ of the total lateral samples and w_a lateral samples for R-WAVE (GTR), PD and 1DH, respectively.

4.5.1 Gelatin-based phantoms

Homogeneous phantoms

Fig.4.17 presents the estimation result for the 10% concentration homogeneous phantom (P2) with a vibration frequency of 250 Hz. While all estimators successfully asses the SWS true value (4.08 ± 0.34 m/s), estimation results of R-WAVE showed better performance due to its slightly reduced STD (PD: 4.02 ± 0.19 m/s, 1DH: 3.76 ± 0.12 m/s, R-WAVE: 3.91 ± 0.09 m/s). Likewise, the same experiment was conducted on the stiffest tissue elasticity phantom (P1: 4.95 ± 0.31 m/s), where results (see Fig.4.18) followed the same trend (PD: 5.17 ± 0.12 m/s, 1DH: 5.00 ± 0.08 m/s, R-WAVE: 5.16 ± 0.06 m/s). However, SWS underestimation is observed on all estimators at the top corners of the reconstructed images (4.4 ± 0.29 m/s). The main cause is the low CNR of the CrW due to reflection at the phantom borders and/or weak coupling. Since this artifacts are related to the CrW quality and not to the performance of the estimators, they were not included in the evaluation region.

Heterogeneous phantoms

SWS plots for the heterogeneous phantom of 8% (3.43 ± 0.28) and 10% (4.08 ± 0.34) gelatin concentration (P6) are shown in Fig.4.19. Similar to experiments of inclusion phantom using the GUI (see Fig.4.4), two square windows of 10 mm (see Fig.4.19.a) were used to quantify mean SWS, STD and quantitative measures of background and inclusion regions, which are displayed in Table 4.4. Again, despite the accurate estimation of both background and inclusion regions of the three estimators, R-WAVE presented higher CNR in comparison with the other ones. Likewise, underestimation is visualized in all cases due to reduced quality of the CrW.

In order to evaluate the influence of the vibration frequency on R-WAVE performance in comparison with the other estimators, data from CWS experiments on a heterogeneous phantom (P7) was processed. A cylindrical lesion of 10 mm diameter was placed at 25 mm depth and multiple acquisitions were conducted at several vibration frequencies, ranging from 140 Hz to 360 Hz in 20 Hz step with a Δf of 0.4 Hz. Additionally, ground truth values were estimated with mechanical measurements
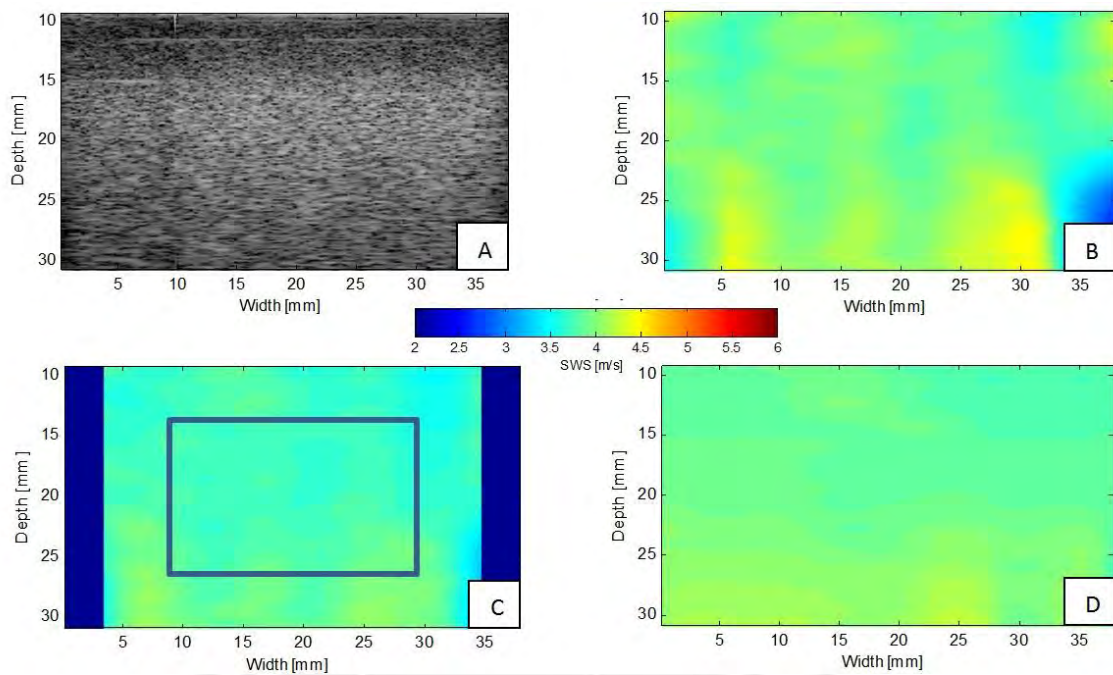
Figure 4.17: Estimated SWS profile of an homogeneous phantom (P2). (a) B-mode image. SWS images using (b) PD, (c) 1DH and (d) R-WAVE.
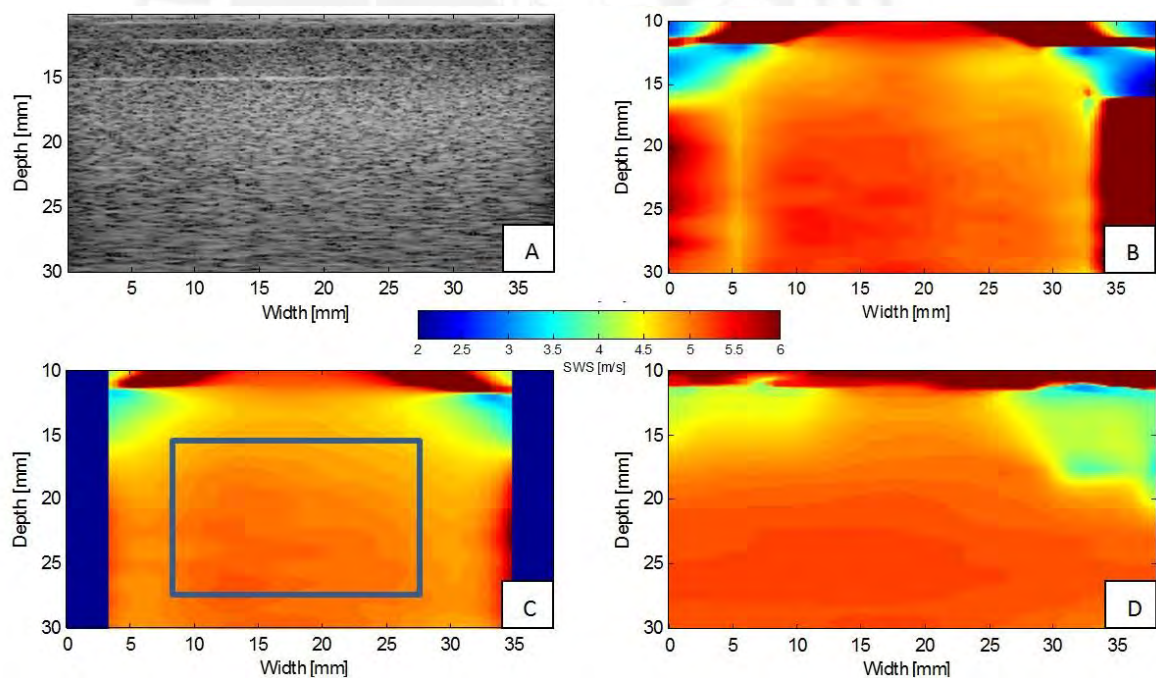
Figure 4.18: Estimated SWS profile of an homogeneous phantom (P1). (a) B-mode image. SWS images using (b) PD, (c) 1DH and (d) R-WAVE
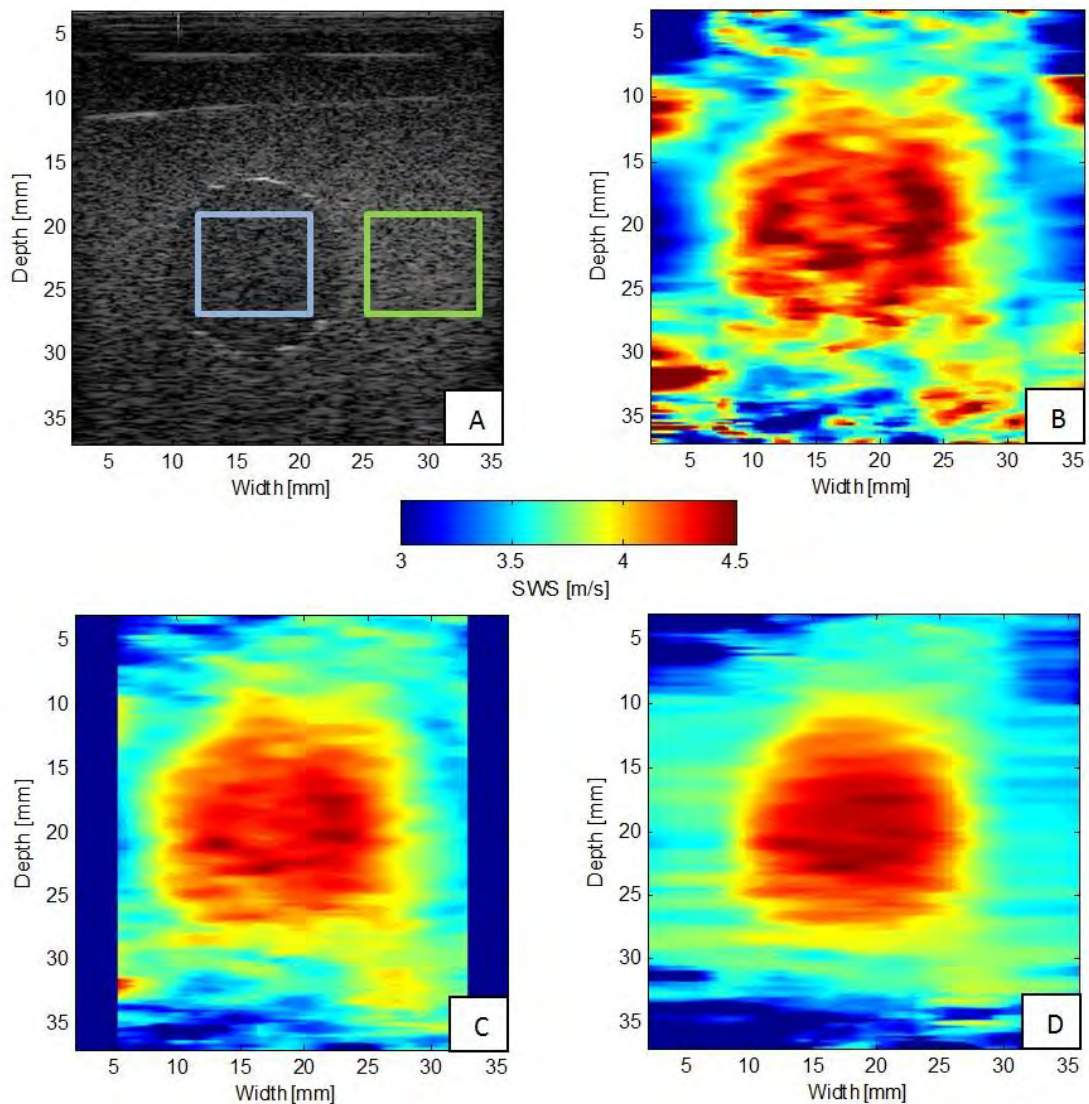
Figure 4.19: Estimated SWS profile of an heterogeneous phantom (P6). (a) B-mode image. SWS images using (b) PD, (c) 1DH and (d) R-WAVE

Table 4.4: Quantitative measurements of the P6 phantom

Est.	SWSi [m/s]	SWSb [m/s]	CNR [dB]	CR [dB]	SR [mm]
PD	4.25 ± 0.19	3.51 ± 0.15	25.02	1.66	1.91
1DH	4.24 ± 0.12	3.63 ± 0.12	28.91	1.36	2.664
R-WAVE	4.31 ± 0.11	3.59 ± 0.09	34.90	1.58	2.83

(MM) applied in homogeneous phantom from each region (Background: 8%, Inclusion: 13%), following the framework of Rojas *et al.* [ROS+13]. A QT/5 mechanical

device (MTS Systems Co., Eden Prairie, MN, USA) with a 5 N load cell was used to test the cylindrical samples of each concentration phantom. Then, the Kelvin Voigt Fractional Derivative (KVFD) model was implemented for fitting each of the acquired stress-relaxation curves. Then measured SWS of the 8%, 13% gelatin phantoms were approximately 3.5 m/s and 5 m/s, respectively. Fig.4.20 shows the quantitative measures from the generated SWS images along the frequency range while Fig.4.21 depicts the comparison of the SWS images between each estimator at a specific frequency. The results closely followed the trend deduced in simulations, since R-WAVE showed the lowest bias of the inclusion SWS at frequencies higher than 200 Hz (PD: 3.34%, 1HD: 5.64%, R-WAVE: 1.48%), which is reflected on CNR, . Furthermore, SR of R-WAVE slightly changed while increasing the vibration frequency (3.54 ± 1.59 mm), which was not the case for PD (8.86 ± 4.89 mm) nor 1DH (6.80 ± 3.14 mm). On the other hand, crawling waves with vibration frequencies below 200 Hz adversely affected accuracy of all estimators for both inclusion (PD: 12.62%, 1HD: 15.38%, R-WAVE: 10.04%) and background regions (PD: 9.78%, 1HD: 8.27%, R-WAVE: 8.10%).
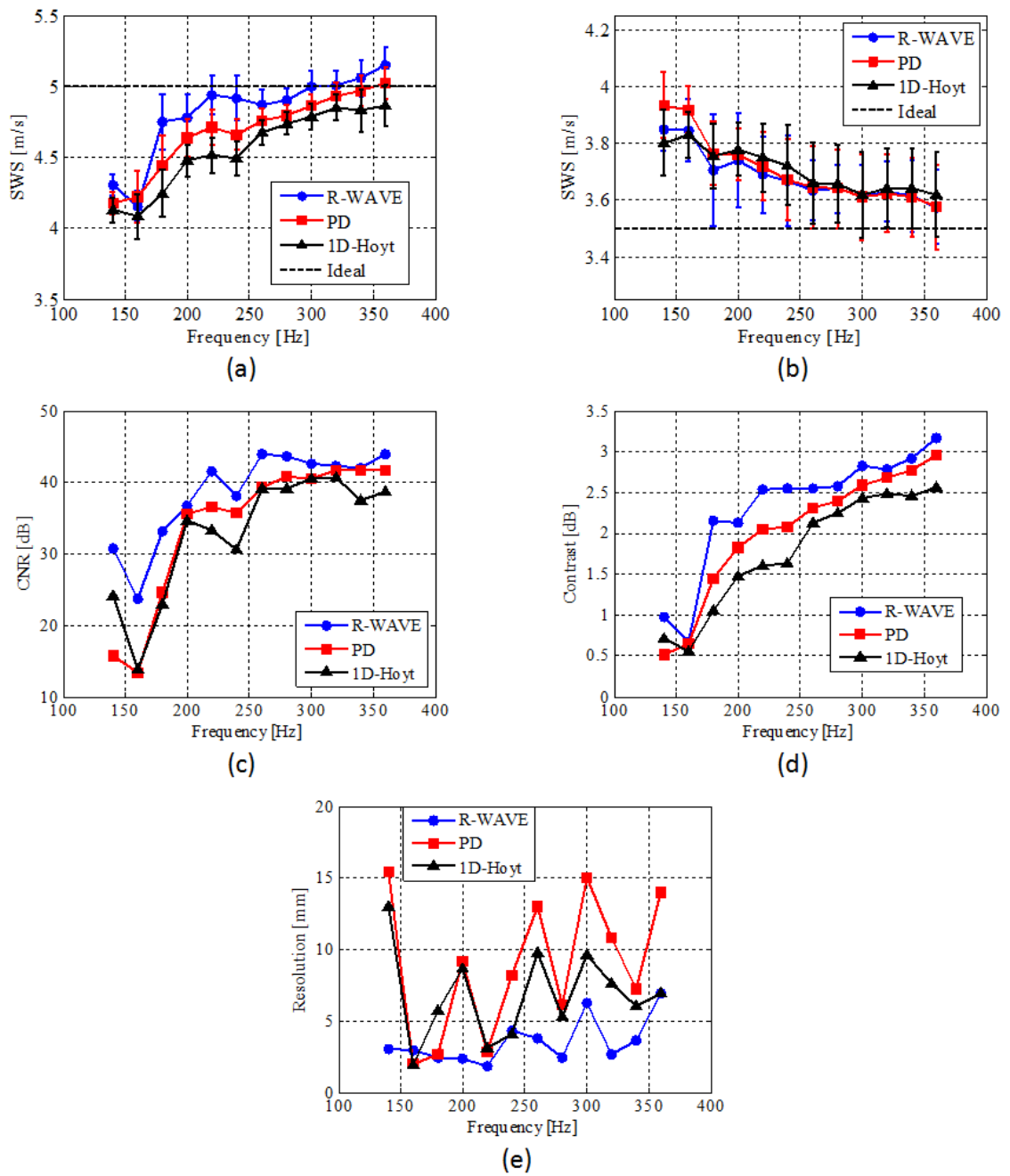
Figure 4.20: Quantitative measurements of each estimator in a heterogeneous phantom (P7). (a) Inclusion SWS, (b) Background SWS, (c) CNR, (d) CR, (e) SR.
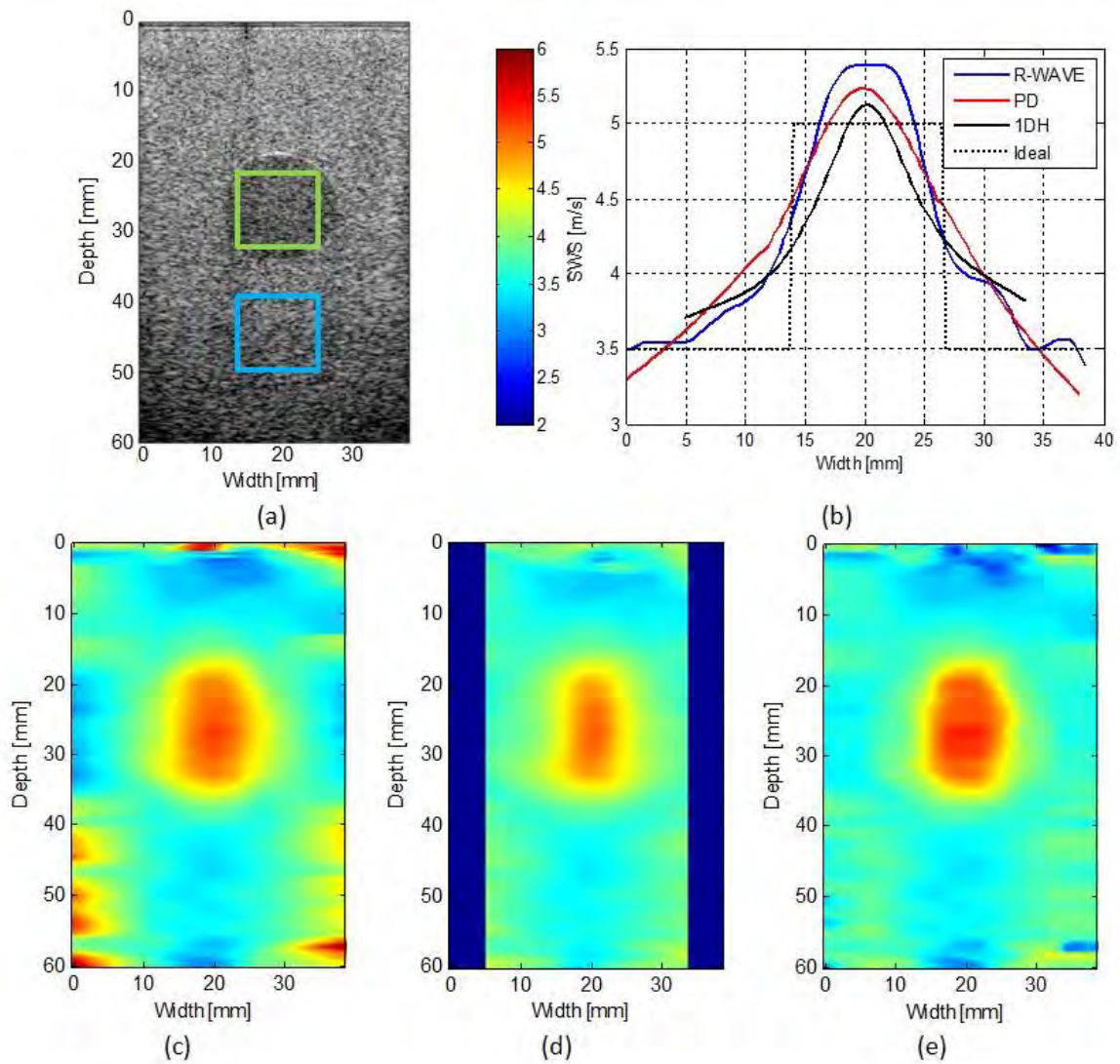
Figure 4.21: SWS images of an inclusion phantom (P7) of 5m/s and 3.5 m/s background SWS. (a) B-mode image. (b) Lateral profile of reconstructed SWS images at 25 mm depth. SWS images using (c) PD, 1DH (d) and (e) R-WAVE

4.5.2 Breast elasticity phantom

Performance of the R-WAVE in comparison with the other estimators was conducted on a calibrated breast elasticity phantom QA 059 (CIRS§, Virginia, USA), which simulated the biomechanical properties of a human breast. The phantom featured spherical lesions of different diameter size (3 mm - 10 mm) and which were randomly distributed in an homogeneous media of 20 ± 5 KPa (2.582 ± 0.346 m/s). According to the technical specifications, inclusion elasticities were guarantied to be higher than

twice the elasticity of the background (i.e. 4.08 m/s). For this CWS experiment, the normal excitation setup was used instead of the parallel setup due the coupling limitations that the latter provides. A vibration module for a vibroelastography system was configured for CWS excitation and attached to the ultrasound transducer (see Fig.4.22). Here, the generated interference pattern is not presented as vertical lines but curved. Therefore, compensation on reconstructed SWS images of all estimators is required, which was computed using Partin *et al.* framework [PHB+13].
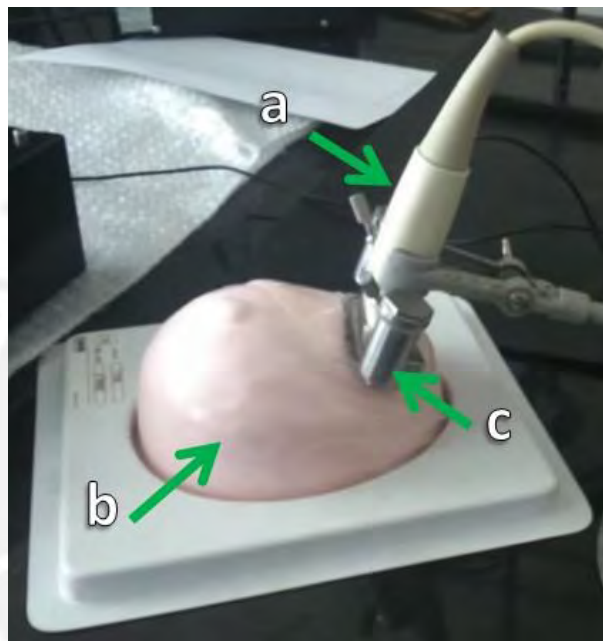
Figure 4.22: Normal excitation setup for CWS experiments on a breast phantom. (a) L14-5/38 transducer. (b) QA 059 breast phantom. (c) Vibration module from a vibroelastography system

Fig.4.23 and Fig.4.24 presents estimation results from two homogeneous regions acquired at 185 Hz and 333 Hz of vibration frequency, respectively. In both cases, all estimators successfully assess the elasticity in the background region since SWS values located between the tolerance of the background regions (PD: 2.30 m/s, 1DH 2.31 m/s, R-WAVE: 2.30 m/s). Still R-WAVE presented lower standard deviation from the estimates (PD: 0.103 m/s, 1DH 0.065 m/s, R-WAVE: 0.039 m/s). In all images, artifacts located at lower and upper boundaries are related to the low CNR of the CrW (see Fig.4.23.b), which are produced due to penetration limitations of the normal excitation as well as inaccurate coupling.

Similarly, Fig.4.25 and Fig.4.26 present estimation results from two lesions acquired at 185 Hz and 260 Hz of vibration frequency, respectively. Here, an underestimation
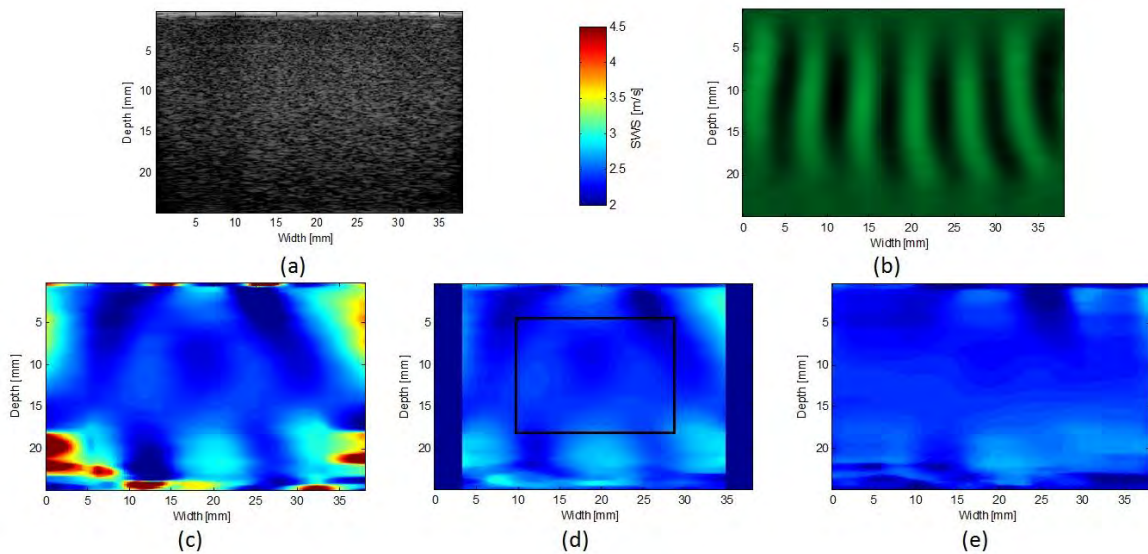
Figure 4.23: SWS images of the first homogeneous region in the breast phantom. (a) B-mode image. (b) CrW image. SWS images using (c) PD, (d) 1DH and (e) R-WAVE
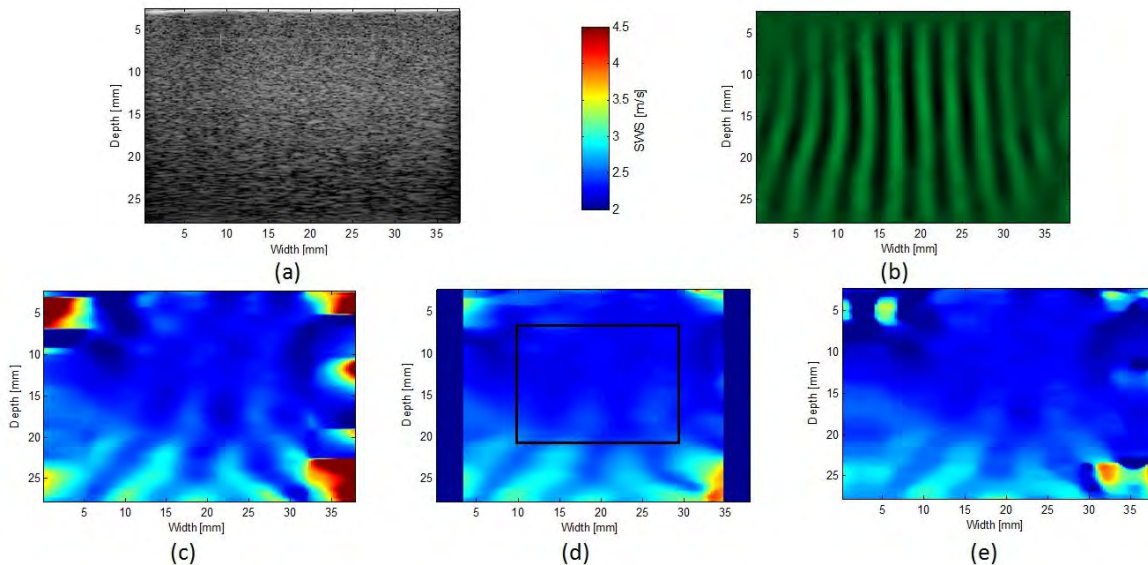
Figure 4.24: SWS images of the second homogeneous region in the breast phantom. (a) B-mode image. (b) CrW image. SWS images using (c) PD, (d) 1DH and (e) R-WAVE

of the lesion for all estimators is evident at 185 Hz (see Table 4.5), which is slightly corrected at higher frequencies (see Table 4.6). While the PD yields the lowest inclusion bias among the three, presence of high estimation artifacts in the lateral sides contributes to added noise in the evaluation region, severely affecting the CNR. Results

on the calibrated phantoms suggest that R-WAVE outperforms PD as well as 1DH in CNR and CR, while no definitive conclusion can be stated regarding the SR.
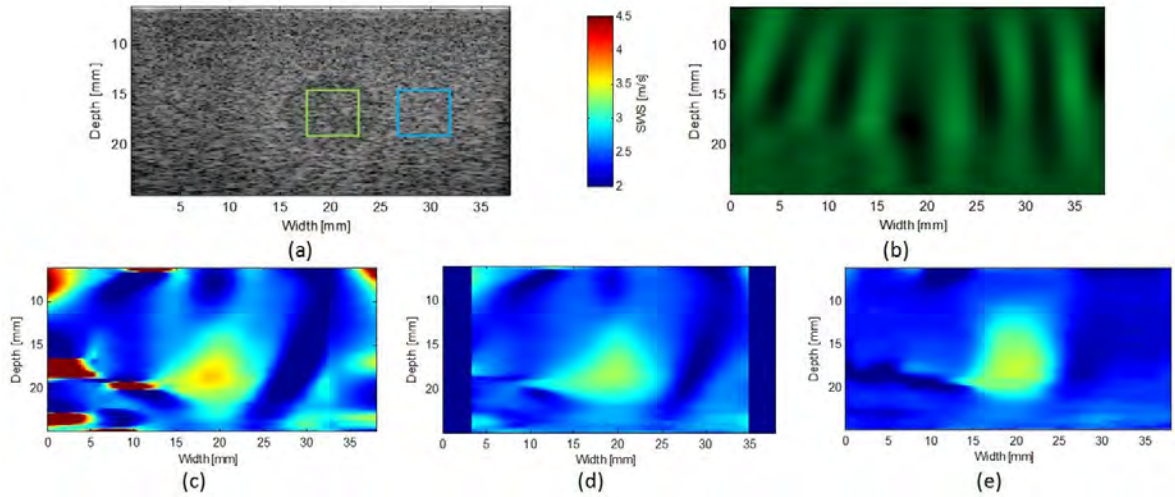
Figure 4.25: SWS images of the first lesion in the breast phantom. (a) B-mode image. (b) CrW image. SWS images using (c) PD, (d) 1DH and (e) R-WAVE

Table 4.5: Quantitative measurements of the first lesions in the breast phantom

Est.	SWSi [m/s]	SWSb [m/s]	CNR [dB]	CR [dB]	SR [mm]
PD	3.39 ± 0.13	2.18 ± 0.44	22.68	3.85	2.04
1DH	3.16 ± 0.07	2.28 ± 0.23	28.68	2.87	4.82
R-WAVE	3.23 ± 0.04	2.22 ± 0.08	47.31	3.26	3.94
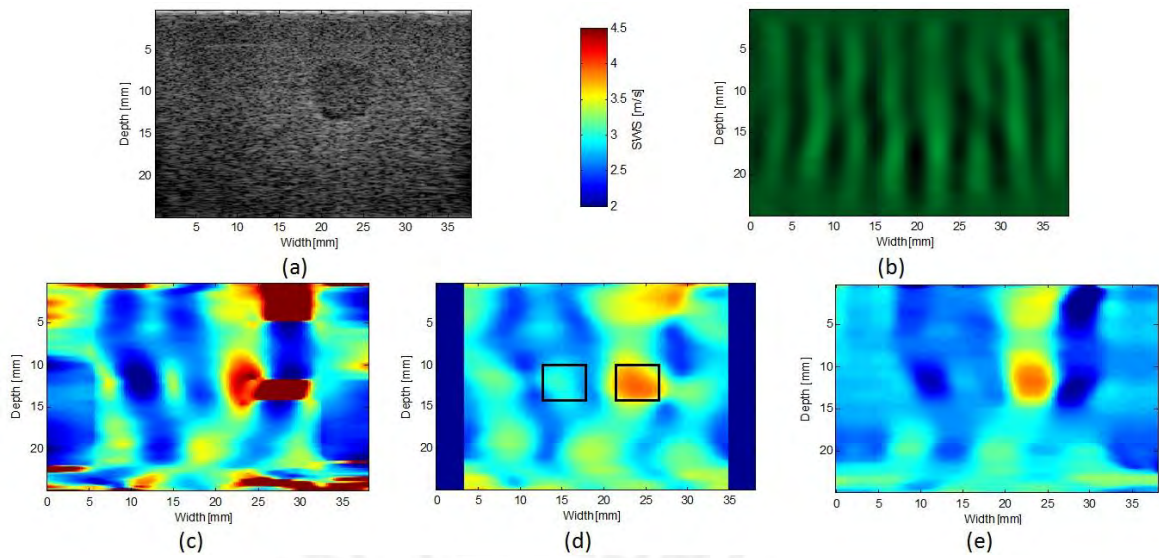
Figure 4.26: SWS images of the second lesion in the breast phantom. (a) B-mode image. (b) CrW image. SWS images using (c) PD, (d) 1DH and (e) R-WAVE

Table 4.6: Quantitative measurements of the second lesions in the breast phantom

Est.	SWSi [m/s]	SWSb [m/s]	CNR [dB]	CR [dB]	SR [mm]
PD	3.92 ± 0.41	2.84 ± 2.02	-5.56	2.74	1.80
1DH	3.61 ± 0.23	2.73 ± 0.17	24.96	2.41	1.94
R-WAVE	3.64 ± 0.18	2.46 ± 0.18	32.37	3.41	1.49

5 Discussion

5.1 GUI for real-time CWS

Despite modifying the IQ filter order from 2 to 6 in the GUI implementation, speckle noise was still found in the reconstructed interference pattern. Although this artifacts could negatively influence the CrW's normalization and DC filtering, most of them are removed with the [3x3] median filter. Hence, estimation errors are not perceived when comparing the final SWS images with the ones obtained from MATLAB implementations. Likewise, increasing the vertical size of this median filter could further enhance CNR of CrW. However, depending on the CWS excitation setup (normal or parallel) and the distance between the sources (*D*), size limitations must be adjusted since CrW might not present the parallel behavior.

Due to the temperature conditions in the experimental environment, data acquisition from gelatin-based phantoms for ground truth values and GUI estimations were conducted at different days. The main reason was the low lifetime of the material, requiring constantly storage and freezing in order to cope with the high temperature and humidity. Therefore, given the cumulative water and increased stiffness from day to day, the mimicking tissue varied its local SWS through the experiment, resulting in SWS estimation errors. This was also the case for R-WAVE experiments on gelatin-based phantoms.

Accuracy estimation on homogeneous as well as heterogeneous phantoms was negatively affected when operating at a higher excitation vibration frequency. For instance, bias in the P3 phantoms increased from 7.29% to 10.20% at 200 Hz and 300 Hz, respectively. Likewise, bias of the inclusion region in the P5 phantom increased from 4.71% to 14.06% operating at the same frequencies. This is understandable since imaging tissues using high excitation frequencies develop into shorter interference patterns, where differentiation of the phase function is more sensitive due to the low resolution of the crawling waves. Hence, a single phase step along the lateral dimension could be rounded up (or rounded down) resulting in biased SWS estimation accuracy, which is verified by the given estimation results. Likewise, lateral artifacts reported in the

literature of PD estimator were as well visualized in the reconstructed SWS images. However, they did not significantly affected differentiation of the examined inclusion from the background region nor the computation of the quantitative measurements. Instead, artifacts of high estimation variance were found through the entire image due to bad coupling of the mini-shakers that were later corrected by increasing the excitation amplitude, improving the SNR of the CrW.

A fixed ROI of was established for the feasibility of CWS in real-time. With the current imaging area, a lesion width a maximum diameter d of 19.64 mm could be detected. Since CWS as well as most elastography techniques are aimed to early detection of tumors, this is not a limitation. For instance, breast cancer lesion of size smaller than 20 mm are commonly classified in the T1 stage group, where most of the elastography-aided diagnosis cases usually fall. However, further classification into T1a ($d < 1$ mm), T1b (1 mm $< d <$ 5 mm), T1c (5 mm $< d <$ 10 mm) and T1d (10 mm $< d <$ 20 mm) subclasses is still not possible given the estimation results on elasticity phantoms. Although the lateral resolution reported (2.19 ± 0.63 mm) was comparable with the performance of CWS in previous studies (2.38 ± 0.51 mm), overestimation is appreciated near boundary regions of the inclusion in SWS images of small diameter (see Fig. 4.5), where the maximum diameter found was 4.8 mm larger (11.8 mm) than the true diameter of the lesion (7 mm).

Several real-time systems of quantitative elastography techniques has been reported in the literature. However in most of these studies, feasibility of such imaging systems is demonstrated by analyzing the acquisition and processing rate in offline mode implementations. Then, if the processing rate outperforms the raw data acquisition rate, real-time imaging is assumed as achieved. In contrast, this study evaluates the physical implementation of the CrW algorithm in a real ultrasound scanner, where the technical characteristic of the processor, memory bandwidth as well as delay generated by running multiple applications in the operating system are also considered. It is worth mentioning that in the present thesis, the concept of real-time imaging is referred to the possibility of depicting a series of images during a standard examination procedure, allowing the technician to correct and acquire new images if complications are encountered.

While a frame rate of 2 Hz allowed real-time visualization of elasticity estimates, several sonoelastography images are required in order to depict a single SWS frame. Therefore, the frame rate reported did not represent the update of the SWS images when moving to a different region of the tissue, changing the vibration frequency or turning on/off the exciters. In the FFT, at $\Delta f = 0.4$ Hz, quality of the θ function

estimation and thus, detection of the inclusion was appreciated after approximately 17 new acquired frames of filtered CrW. Therefore, the true update rate when changing imaging regions was around 8.5 s. This is still comparable with other real-time implementations such as the case of vibroelastography [BEW⁺12], where a delay of approximately 5 to 7 seconds is to be expected before displaying an image in order to stabilize the autocorrelation function used for speckle tracking. Moreover, enhancement of the final image is achieved by averaging previously processed SWS values, lowering the frame rate as well.

The reported speedup (26.16 ± 0.22) is comparable with the framework of Baghani *et al.*, where an average speedup of 32 was achieved for an implementation of freehand vibroelastography system [BEW⁺12] using a CUDA supporting graphics card (GTX 580 NVIDIA). Regarding the computing architecture, it is worth mentioning that the current work was conducted on a single GPU of relatively standard computing features (GTX 750 NVIDIA). Hence, increasing the number of GPU as well as enabling multi-thread processing in the host computer could significantly improve the speed up, which develops into higher frame rates of displayed SWS images, as reported in previous contributions [YTY11].

5.2 R-WAVE performance

Simulation results at lower frequencies severely degraded the performance of the three estimators. In the case of R-WAVE, imaging tissues with low excitation frequencies produces fewer interference patterns in a single frame, detecting one or two pairs of peaks at most. Therefore, the overdetermined system of equations initially assumed is not necessary achieved due to missing local SWS values, which worsen the ill-posed problem and generates high estimation errors in the solution of the x vector. On the other hand, in comparison with the other estimators that are more sensible to estimation errors at higher frequencies, wavelength of the CrWs are shortened and more interference patterns are visualized. Thus, more equations can be processed in a single frame, reducing the condition number of total matrix A and improving the CNR (+4.3 dB from 200 Hz to 450 Hz at a =1) as well as spatial resolution (-3.8 mm from 200 Hz to 450 Hz at a =1).

Although variation of the smoothing parameters was not evaluated in tissue mimicking phantoms, simulation results showed that increasing this parameter for PD and 1DH compromised the CNR as well as the lateral resolution, while R-WAVE performance was slightly affected even when considering a values far superior than the ones

usually selected for SWS estimation. The degradation of CNR in PD is related to the increase of lateral artefacts that are produced at higher LOESS kernel size, which affects the STD of both high and low elasticity regions. Likewise, while 1DH present SNR enhancement by increasing the autocorrelation kernel size, SWS underestimation of region is also observed, severly affecting the CNR.

Results from homogeneous phantoms indicates that R-WAVE provide robust assessment of homogeneous medium due to it CV in soft (PD: 4.7%, 1DH: 2.9%, R-WAVE: 2.2%) and stiffer (PD: 2.4%, 1DH: 1.6%, R-WAVE: 1.2%) tissues. Likewise R-WAVE performance on the P7 heterogeneous phantom while varying the vibration frequency indicates a favorable accuracy for both inclusion and background regions except for frequencies below 200 Hz due to the low quantity of peaks along the lateral profile, as noted in the previous discussion. In practice, limitations of R-WAVE applications may be found on stiffer lesions or regions where typical excitation frequency is set under 200 Hz, such as prostate cancer or ablation liver for ex-vivo experiments.

One of the advantages of the R-WAVE method in comparison with PD method is the reduction of artifacts in the boundaries of the ROI. While artifacts in the lateral sides were severely diminished mostly as a result of the wavelength extrapolation, artifacts at top and bottom regions were also reduced. In practice, these artifacts with high values of shear wave speed might mislead the technician into the presence of stiffer masses. Thus, the accuracy of diagnosis is undermined due to false-positive lesions, which are suppressed by the R-WAVE method. Similar to this artifacts, reduction of the image width is produced due to the increment the smoothing parameter w_a of the 1DH estimator. In contrast, R-WAVE maintains the effective ROI for SWS reconstruction when operating at a high regularization coefficient a.

Finally, experiments conducted on homogeneous regions from the calibrated breast phantom showed favorable results for all estimators in successfully assessing the true SWS values. However, despite the boundary artifacts in all images due to the CrW low SNR, R-WAVE provided more robust elastograms which are related to a lower CV (PD: 4.5%, 1DH: 2.8%, R-WAVE: 1.7%). For lesion experiments, PD presented the smallest bias in the SWS estimates compared to the true value stated by the provider (PD: 3.92%, 1DH: 11.52%, R-WAVE: 10.78%). Still, images generated from R-WAVE depicted reduced artifacts and well-defined homogeneous regions, surpassing the other ones in locating the lesion . One possible cause of the underestimation in inclusion regions is the distortion of the crawling waves due to multiples reflections produced by near lesions in a confined space. For instance, when displaying a B-mode image where no apparent lesion is observed, crawling waves of certain circular curvature could still

be visualized, which are further processed and converted in a lesion. Similarly, crawling wave acquisition from the current inclusion experiments might be affected by reflection of other lesion located along the azimuthal direction of the transducer, stretching or compressing the wavelength the projected crawling waves in the ROI and thus, adding bias to the results. However, validation of this hypothesis is yet to be tested and will be conducted in future works.

From all the experiments conducted it can be concluded that the regularized method outperforms the other estimators in CNR and estimation accuracy. Although an improved lateral resolution was achieved in R-WAVE simulations, experiments on tissue mimicking phantoms did not completely reflected this trend. Hence, no definitive conclusion can be stated regarding this last metric.
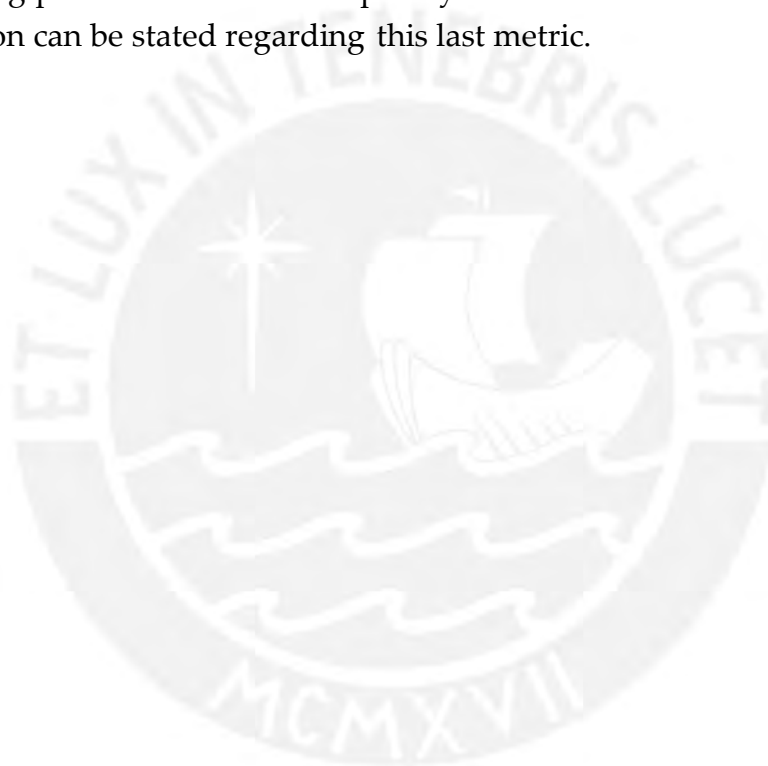
6 Conclusion

In this study, a real-time graphical user interface for quantitative elastography based on GPU parallel processing was successfully implemented on a research ultrasound system. Experiments on tissue mimicking phantoms have demonstrated good performance on the accuracy of the shear wave speed estimates while also allowing the user to adjust, in real-time, display parameters that could improve the quality of the reconstructed elasticity images. On the other hand, a novel shear wave speed estimator has been proposed and tested on simulation, gelatin-based phantoms and calibrated tissue mimicking phantoms. The performance comparison with other estimators found in the literature suggest that the new estimator demonstrates significant artifact reduction, CNR enhancement and improved estimation accuracy of SWS images while maintaining the effective ROIs. This two contribution benefits the implementation and development of further elastography techniques that could provide enhanced quality of elasticity images and thus, improved accuracy of diagnosis.

Appendix

A R-WAVE: Weighted coefficient estimation analysis

A.1 Wavenumber model

Let A and B be regions of different elasticity located in a CrW segment (between two peaks) generated by a frequency f and $f + \Delta f$, as presented in Fig. A.1. The sinus segments for each region are obtained using Eqn. 2.15 and wavenumber K_A and K_B, with no attenuation ($a_c = 0$) and no movement ($t = 0$). For simplification purposes, both regions are composed of one element each, an equivalent region Eq is estimated by measuring the distance between peaks.
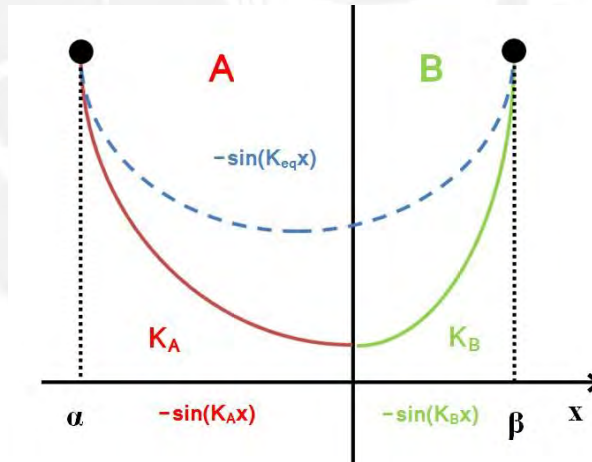
Figure A.1: Theoretical setup for two regions located in a CrW segment

At the beginning and end of each peak, both curves $-\sin(K_A x)$ and $-\sin(K_B x)$ converge with $-\sin(K_{eq})$, therefore:

$$x = a: \quad -\sin(K_A a) = -\sin(K_{eq} a), \quad \Rightarrow \quad K_A a - K_{eq} a = 2\pi n \tag{A.1}$$

$$x = \beta: \quad -\sin(K_B \beta) = -\sin(K_{eq} \beta), \quad \Rightarrow \quad K_B \beta - K_{eq} \beta = 2\pi m \tag{A.2}$$

Summing Eq.A.1 and Eq.A.2:

$$K_A a + K_B \beta - K_{eq}(a + \beta) = 2\pi l, \quad l = n + m \tag{A.3}$$

$$\frac{a}{a + \beta} K_A + \frac{\beta}{a + \beta} K_B = K_{eq} + \frac{2\pi l}{a + \beta} \tag{A.4}$$

Since the number of cycles in the equivalent medium is not greater than 1, $l = 0$. The relationship obtained in Eqn. A.4 can be used in the regularized method (i.e. GTR) as $Ax_j = K_{av}$, where K_{av} is the average wavenumber measured between peaks. The resulting SWS values can be later obtained by computing $c = 2\pi f / k$. However, a quick simulation (see Fig. A.2) shows that the Wavenumber Model (WM) presents an under-damped response in a step function of elasticity compared with the Empirical Model (EM) described in section 3.2.4. Since the optimization variable of the the EM (c) differs from the WM (k), a different regularization coefficient is used for the latter. The simulation setup is detailed in Table 3.4.
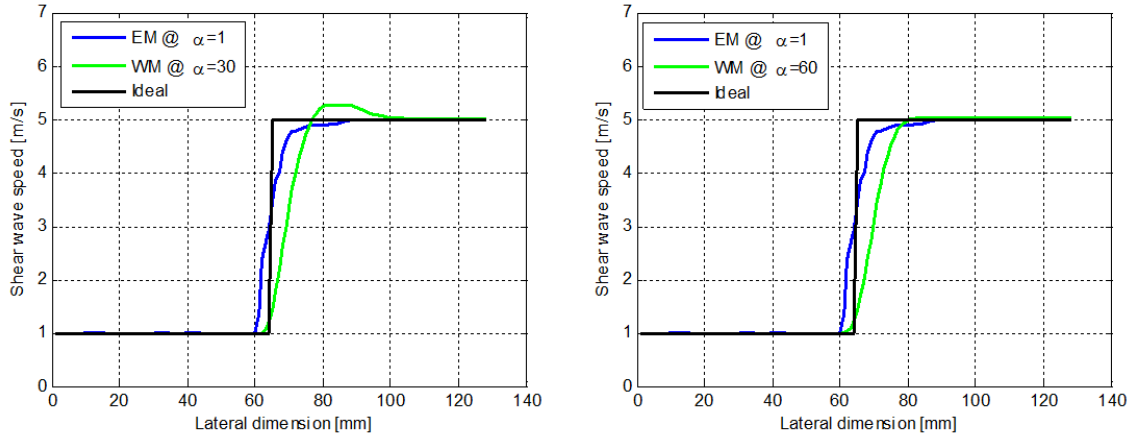
Figure A.2: Solutions from a simulated inhomogeneous media using the Wavenumber Model and the Empirical Model with different a

A.2 Shear wave speed model

Another solution is recasting the optimization problem in terms of the variable c to further reduce the error amplification in $c = 2\pi f / k$, as stated in the last approach. Using $k = 2\pi f / c$ in Eqn. A.4 results:

$$\frac{a}{a + \beta} \frac{2\pi f}{C_A} + \frac{\beta}{a + \beta} \frac{2\pi f}{C_B} = \frac{2\pi f}{C_{eq}} \tag{A.5}$$

$$(a+\beta)\frac{C_A C_B}{aC_B+\beta C_A}=C_{eq} \tag{A.6}$$

Since this is a non-linear problem, the Taylor series is used to approximate it to a 1st order linear equation around a fixed SWS value C_0 for both C_A and C_B:

$$f(C_A,C_B)\vert_{C_1,C_2}\approx f(C_1,C_2)+\frac{\partial f(C_1,C_2)}{\partial C_A}(C_A-C_1)+\frac{\partial f(C_1,C_2)}{\partial C_A}(C_B-C_2) \tag{A.7}$$

Estimating each term in Eqn. A.6

$$f(C_A,C_B)=(a+\beta)\frac{C_A C_B}{aC_B+\beta C_A} \tag{A.8}$$

$$f(C_1,C_2)=(a+\beta)\frac{C_0^2}{C_0(a+\beta)}=C_2 \tag{A.9}$$

$$\frac{\partial f(C_1,C_2)}{\partial C_A}(C_A-C_1)=\frac{C_0(aC_0+\beta C_0)-\beta C_0^2}{(a+\beta)C_0^2}(C_A-C_0)=\frac{a}{a+\beta}(C_A-C_0) \tag{A.10}$$

$$\frac{\partial f(C_1,C_2)}{\partial C_B}(C_B-C_2)=\frac{C_0(\beta C_0+aC_0)-aC_0^2}{(a+\beta)C_0^2}(C_B-C_0)=\frac{\beta}{a+\beta}(C_B-C_0) \tag{A.11}$$

Then, replacing each term in Eqn. A.7

$$f(C_A,C_B)\vert_{C_1,C_2}\approx\frac{a}{a+\beta}C_A+\frac{\beta}{a+\beta}C_B \tag{A.12}$$

From Eqn. A.12 it can be observed that the Taylor approximation is very similar to the WM. However, since the Shear Wave Speed Model (SWSM) is expressed in terms of the shear wave speed *c*, no additional inversion steps are required to find *c*, avoiding computation errors. Similar to the previous model, simulations were conducted for both SWSM and EM in inhomogeneous media (see Fig. A.3). Although both models presented similar responses at the same regularization coefficient, the EM exceed the SWSM in lateral resolution and estimation accuracy, even when increasing a in the SWSM. Hence, EM is selected for the estimation of the weighted coefficients in the R-WAVE algorithm of the current thesis work.
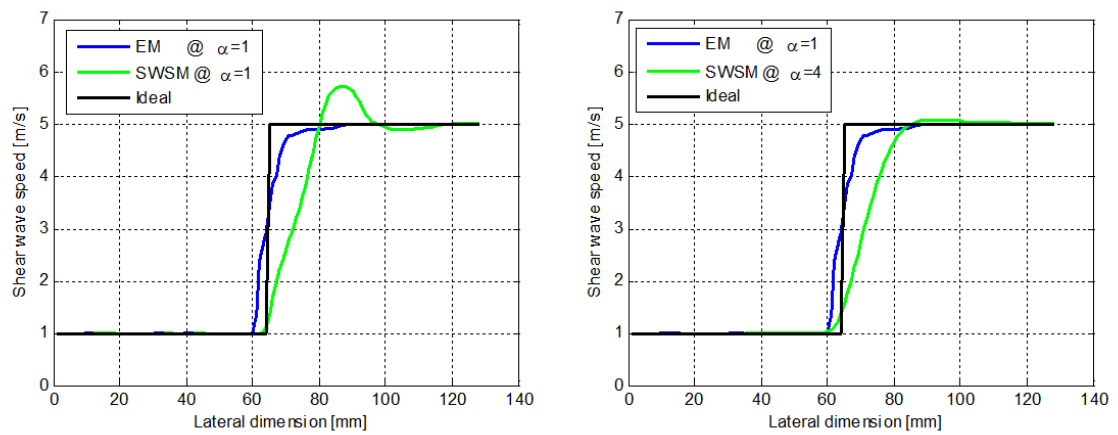
Figure A.3: Solutions from a simulated inhomogeneous media using the Shear Wave Speed Model and the Empirical Model with different a

Bibliography

[ADP12] Reza Zahiri Azar, Kris Dickie, and Laurent Pelisser. Real-time 1-d/2-d transient elastography on a standard ultrasound scanner using mechannically induced vibration. *IEEE Transactions on Ultrasonics, Ferroelectrics and Frequency Control*, 59(10):2167–2177, 2012.

[BEW+12] A. Baghani, H. Eskandari, W. Wang, D. Da Costa, N. Lathiff, R. Sahebjavaber, S. Salcudean, and R. Rohling. Real time quantitative elasticity imaging of deep tissue using free-hand conventional ultrasound. *MICCAI*, 7511:617–624, 2012.

[BKF+13] M. Birk, E. Kretzek, P. Figuli, M. Weber, J. Beckeer, and N. Ruiter. High speed medical imagin in 3d ultrasound computer tomography. *IEEE Transactions on Parallel and Distributed Systems*, PP(99), 2013.

[Bou95] P. Bourke. *RGB colour space*. paulbourke.net/texturecolour/colourspace/, 1995.

[BTF04] J. Bercoff, M. Tanter, and M. Fink. Supersonic shear imaging: a new technique for soft tissue elasticity mapping. *IEEE Trans Ultrason Ferroelectr Freq Control*, 51(4):396–409, 2004.

[CAW+09] B. Castañeda, L. An, S. Wu, J. Baxter, J. Yao, J. Joseph, K. Hoyt, J. Strang, D. Rubens, and K. Parker. Prostate cancer detection using crawling wave sonoelastography. *Proc. SPIE, Medical Imaging: Ultrasonic Imaging and Signal Processing*, 7265(13), 2009.

[CCH16] Zhaohong Chen, Yongdong Chen, and Qinghua Huang. Development of a wireless and near real-time 3d ultrasound strain imaging system. *IEEE Transactions on Biomedical Circuits and Systems*, 10(2):394–403, 2016.

[CORP13] B. Castañeda, J. Ormachea, P. Rodríguez, and K. J. Parker. Applications of numerical methods to elasticity imaging. *Mol Cell Biomech*, 10(1):43–65, 2013.

[CWF99] S. Catheline, F. Wu, and M. Fink. A solution to diffraction biases in sonoe-
lasticity: the acoustic impulse technique. *J. Acoust. Soc. Am*, 105(5):2941–
2950, 1999.

[dEN14] Instituto Nacional de Enfermedades Neoplásicas. *Registro de Cáncer de
Lima Metropolitana. Volumen IV Estudio de incidencia y mortalidad 2004-
2005*. Ministerio de Salud, 2014.

[Duc90] F. Duck. *Physical Properties of Tissue-A Comprehensive Reference Book*.
Academic Press, 6 edition, 1990.

[EM13] E. Elegbe and S. McAleavey. Single tracking location methods sup-
press speckle noise in shear wave velocity estimation. *Ultrasonic imaging*,
35(2):109–125, 2013.

[FG99] M. Fatemi and J. Greenleaf. Vibro-acoustography: An imaging modal-
ity based on ultrasound-stimulated acoustic emission. *Proceedings of the
National Academy of Sciences*, 96(12):6603–6608, 1999.

[FSB+08] J. Ferlay, H.R. Shin, F. Bray, D. Forman, C. Mathers, and D.M. Parkin.
Cancer Incidence and Mortality Worldwide: IARC CancerBase No. 10.
GLOBOCAN, 2008.

[GFI03] J. F. Greeleaf, M. Fatemi, and M. Insana. Selected methods for imag-
ing elastic properties of biological tissues. *Annual Review of Biomedical
Engineering*, 5:57–58, 2003.

[GH12] M. Gomez and J. Huayanay. Mamografia y ecografia en la evaluación de
las lesiones no palpables de la mama y su correlación anatomo-patológica.
Revista Médica Herediana, 13(2), 2012.

[GPAL95] L. Gao, K.J. Parker, S. K. Alam, and R.M. Lerner. Sonoelasticity imag-
ing: Theory and experimental verification. *Jour. Acoust. Soc. of Am.*,
97(6):3875–3886, 1995.

[GSB11] I. Gheonea, Z. Stoica, and S. Bondari. Differential diagnosis of breast
lesions using ultrasound elastography. *Indian Journal of Radiology and
Imaging*, 21(4):301–305, 2011.

[GSD+04] M. Goethem, K. Schelfout, L. Dickmans, J. Van Der Auwera, J. Weyler,
J. Verslegers, I. Biltjes, and A. De Schepper. Mr mammography in the

pre-operative staging of breast cancer in patients with dense breast tissue: comparision with mammography and utlrasound. *European Radiology*, 14(5):809–816, 2004.

[Gue11] J. Guerrero. El rol de la mamografia en el diagnóstico del cáncer de mama. *Carcinos*, 1(2), 2011.

[HCP07] K. Hoyt, B. Castaneda, and K. J. Parker. Muscle tissue characterization using quantitative sonoelastography: Preliminary results. *IEEE Ultrasonic Symposium*, pages 365–368, 2007.

[HCP08] K. Hoyt, B. Castaneda, and K. J. Parker. Two-dimensional sonoelastographic shear velocity imaging. *Ultrasound Med. and Biol.*, 34(2):276–288, 2008.

[HHM⁺12] Z. Hah, C. Hazard, B. Mills, C. Barry, D. Rubens, and K. J. Parker. Integration of crawling waves in an ultrasound imaging system: Part 2. signal processing and applications. *Ultrasound Med Biol.*, 38:312–323, 2012.

[HPR07] K. Hoyt, K. Parker, and D. Rubens. Real time shear velocity imaging using sonoelastographic techinques. *Ultrasound in Medicine and Biology*, 33(7):1086–1097, 2007.

[IGV⁺14] T. Itzenga, E. Gaburov, W. Vermin, J. Menseen, and C. Korte. Fast 2-d ultrasound strain imaging: The benefits of using a gpu. *IEEE Transactions on Ultrasonics, Ferroelectrics and Frequency Control*, 61(1):207–213, 2014.

[LBHY04] J. Luo, J. Bai, P. He, and K. Ying. Axial strain calculation using a low-pass digital differentiator in ultrasound elastography. *IEEE Transactions on Ultrasonics, Ferroelectrics and Frequency Control*, 51(9):1119–1127, 2004.

[LKO06] R. Lavarello, F. Kamalabadi, and W. O'Brien. A regularized inverse approach to ultrasonic pulse-echo imaging. *IEEE Transactions on Medical Imaging*, 25(6):712–722, 2006.

[LMRT10] K. Lin, J. McLaughlin, D. Renzi, and A. Thomas. Shear wave speed recovery in sonoelastography using crawling wave data. *Acoust. Soc. Am.*, 128(1):88–97, 2010.

[MR72] K. Miller and M. Rochwarger. A covariance approach to spectral moment estimation. *IEEE Transactions on Information Theory*, 18(5), 1972.

[MTB+09] Gabriel Montaldo, Michael Tanter, Jeremy Bercoff, Nicolas Benech, and Matias Fink. Coherent plan-wave compounding for very high frame rata ultrasonography and transient elastography. *IEEE Transactions on Ultrasonics, Ferroelectrics and Frequency Control*, 56(3):489–506, 2009.

[OAG+99] J. Ophir, S. K. Alam, B. Garra, F. Kallel, and E. Konofagou. Elastography: ultrasonic estimation and imaging of the leastic properties of tissues. *Proc. Instn. Mech. Engrs.*, 213(1):203–233, 1999.

[PHB+13] A. Partin, Z. Hah, C. Barry, D. Rubens, and K. Parker. Elasticity estimates from images of crawling wave generated by miniature surface sources. *Ultrasound Med Biol.*, 40(4):1–10, 2013.

[Pro98] R. Prochazka. *Sobrevida y Recurrencias en Cáncer de Mama segun el Estadío Clínico y el Compromiso Auxilar*. Universidad Peruana Cayetano Heredia, 1998.

[PTG05] K. J. Parker, L. S. Taylor, and S. Gracewski. A unified view of imaging the elastic properties of tissue. *Jour. Acoust. Soc. of Am.*, 117(1):2705–2712, 2005.

[RBF+08] Hassan Rivaz, Emad Boctor, Pezhman Foroughi, Richard Zellars, Gabor Fichtinger, and Gregory Haeger. Ultrasound elastography: A dynamic programming approach. *IEEE Transactions on Medical Imaging*, 27(10):1373–1377, 2008.

[RK10] J. Randers and E. Kandrot. *CUDA by Example: An Introduction to General-Purpose GPU Programming*. Addison-Wesley, 2010.

[ROS+13] R. Rojas, J. Ormachea, A. Salo, P. Rodriguez, A. Lerner, and B. Castaneda. Crawling waves speed estimation based on dominant component analysis am-fm demodulation. *International Tissue Elasticity Conference (ITEC)*, page 100, 2013.

[RPN11] S. Rosenzweig, M. Palmeri, and K. Nightingale. Gpu-based real-time small displacement estimation with ultrasound. *IEEE Transactions on Ultrasonics, Ferroelectrics and Frequency Control*, 58(2):399–405, 2011.

[RPR+12] S. Rosenzweig, M. Palmeri, N. Rouze, S. Lipman, E. Kulbacki, J. Madden J, T. Polascik, and K. Nightingale. Comparison of concurrently acquired in

vivo 3d arfi and swei images of the prostate. *IEEE International Ultrasonic Symposium*, pages 97–100, 2012.

[RWPN12] N. Rouze, M. Wang, M. Palmeri, and K. Nightingale. Parameters affecting the resolution and accuracy of 2-d quantitative shear wave images. *IEEE Transactions on Ultrasonics, Ferroelectrics and Frequency Control*, 59(8):1729–1740, 2012.

[SDS14] G. Stoica, R. Dogaru, and E. Stoica. Speeding-up image processing in reaction-diffusion cellular neural networks using cuda-enable gpu platforms. *ECAI International Conference*, pages 39–42, 2014.

[TF14] M. Tanter and M. Fink. Ultrafast imaging in biomedical ultrasound. *IEEE Transactions on Ultrasonics, Ferroelectrics, and Frequency Control*, 61(1):102–119, 2014.

[TSR06] E. Turgay, S. Salcudean, and R. Rohling. Identifying the mechanical properties of tissue by ultrasound strain imaging. *Ultrasound in medicine and biology*, 32(2):221–235, 2006.

[WTRP04] Z. Wu, L. Taylor, D. Rubens, and K. Parker. Sonoelastographic imaging of interference patterns for estimation of the shear velocity of homogeneous biomaterials. *Physics in medicine and biology*, 49(6):911–922, 2004.

[WTRP06] Z. Wu, L. S. Taylor, D. J. Rubens, and K. J. Parker. Sonoelastographic imaging of interference patterns for estimation of the shear velocity distribution in biomaterials. *J. Acoust. Soc.*, 120(1):535–545, 2006.

[XPKB09] T. XU, T. Pototschnig, K. Kühnlenz, and M. Buss. A high speed multi gpu implementation of bottom up attention using cuda. *IEEE International Conference on Robotics and Automation*, pages 41–47, 2009.

[YDR11] Xu Yang, Sthiti Deka, and Raffaella Righetti. A hybrid cpu-gpgpu approach for real-time elastography. *IEEE Transactions on Ultrasonics, Ferroelectrics and Frequency Control*, 58(12):2631–2645, 2011.

[YM12] M. Yaffe and J. Mainprize. Risk of radiation-induced breast cancer from mammographic screening. *Radiology*, 264(1):203–233, 2012.

[YTY11] Billy Yiu, Ivan Tsang, and Alfred Yu. Gpu-based beamformer: Fast realization of plane wave compounding and synthetic aperture imaging.

IEEE Transactions on Ultrasonics, Ferroelectrics, and Frequency Control, 58(8):1698–1705, 2011.

[YY15] Billy Yiu and Alfred Yu. Gpu-based minimum variance beamformer for synthetic aperture imaging of the eye. *Ultrasound in Med. and Biol.*, 41(3):871–883, 2015.

[ZCW⁺07] M. Zhang, B. Castaneda, Z. Wu, P. Nigwekar, J. V. Joseph, D. J. Rubens, and K. J. Parker. Congruence of imaging estimators and mechanical measurements of viscoelastic properties of soft tissues. *Ultrasound in Medicine and Biology*, 33(10):1617–1631, 2007.

List of Figures

List of Tables

List of Abbreviation and Symbols

1DH . . . . 1-Dimensional Hoyt
ARFI . . . . Acoustic Radiation Force Imaging
CNR . . . . Contrast-to-Noise Ratio
CR . . . . ContRtast
CrW . . . . Crawling Wave
CT . . . . Computarized Tomography
CV . . . . Coefficient of Variation
CWS . . . . Crawling Wave Sonoelastography
FIR . . . . Finite Impulse Response
FPGA . . . . Field Programmable Gate Array
FPS . . . . Frames Per Second
FR . . . . Frame Rate
GPU . . . . Graphical Processor Unit
GUI . . . . Graphical User Interface
IIR . . . . Infinite Impulse Response
LFE . . . . Local Frequency Estimator
LPF . . . . Low Pass Filter
LSO . . . . Linear Square Optimization
MM . . . . Mechanical Measurements
MRI . . . . Magnetic Resonance Imaging
PD . . . . Phase Derivative
PRF . . . . Pulse Repetition Frequency
PRP . . . . Pulse Repetition Period
QEA . . . . Quasi-Eigenfunction Approximation
QP . . . . Quadratic Programming
R-WAVE . . . . Regularized Wavelength Average Velocity Estimator
SNR . . . . Signal to Noise Ratio
SR . . . . Spatial Resolution
SSI . . . . Supersonic Shear Imaging

STD . . . . STandard Deviation
STL . . . . Single Tracking Location
SWEI . . . . Shear Wave Elastography Imaging
SWS . . . . Shear Wave Speed
TE . . . . Transient Elastography
US . . . . UltraSound Imaging

Declaration

I hereby declare that I have independently worked in the present study without using other sources than the indicated above. Likewise, all reports that were literally taken or adapted from published sources are indicated. As a result of this investigation, two proceeding articles have already been accepted and two journal articles are currently being written.

Lima, 24. 07. 2017   Eduardo González